Activity Report
of
Synchrotron Radiation Laboratory
2009

Synchrotron Radiation Laboratory
Institute for Solid State Physics
The University of Tokyo
5-1-5 Kashiwanoha, Kashiwa, Chiba 277-8581
Japan

TABLE OF CONTENTS

6) Spin and Angle-resolved Photoelectron Spectroscopy on Si(557)-Au surface
T. Okuda, K. Miyamoto, Y. Takeichi, H. Miyahara, M. Ogawa, A. Kimura, A. Harasawa, A. Kakizaki, T. Shishidou, and T. Oguchi

7) Spin-resolved photoemission study on Dirac-like surface states of ultrathin Bi_2Se_3 films
Y. Sakamoto, T. Hirahara, Y. Takeichi, I. Matsuda, A. Kakizaki, and S. Hasegewa

8) Electronic structure of $BaPrO_3$-based oxides studied with soft X-ray absorption and emission spectroscopy
S. Yamaguchi, T. Higuchi, Y. Oyama, S. Miyoshi, S. Mimuro, and T. Kikuchi

9) Characterizations of Core Level Electronic Structure and Interaction of Ln-M Cyano DMF Complex by Soft-X-ray Spectroscopy (in 2009)
T. Akitsu

10) A Study on the Electronic Structure of Proton Conducting $A^{III}B^{III}O_3$ Single Crystal
H. Yugami, Y. Nagao, J. Liu, T. Higuchi, F. Iguchi, and N. Sata

11) Resonant Soft-X-ray Emission Study of $La_{0.6}Sr_{0.4}FeO_3$ Thin Film
T. Higuchi, M. Matsumoto and J. Guo

12） Electronic States of Superconductor without Inverse Symmetry
M. Hirai, H. Okazaki, Y.Yao, S. Yoshida, Y. Muraoka, and T. Yokoya

13) Atomic and electronic band structure of the $\sqrt{21}\times\sqrt{21}$ phase formed by Au adsorption on the Ag/Si(111)-6×1 surface
F. Nakamura, Y. Takeichi, A. Harasawa, A. Kakizaki, and I. Matsuda

14) A New Soft X-ray Beamline BL07LSU at SPring-8: Design and Status
S. Yamamoto, Y. Senba, H. Ohashi and, I. Matsuda

15) Development of picosecond time-resolved soft x-ray spectroscopy system at SPring-8
M. Ogawa, S. Yamamoto, Y. Kousa, A. Fukushima, A. Harasawa, H. Kondo, A. Kakizaki, and I. Matsuda

16) Direct spectroscopic evidence of spin-dependent hybridization between Rashba-split surface states and quantum-well states
K. He, Y. Takeichi, M. Ogawa, T. Okuda, P. Moras, D. Topwal, A. Harasawa, C. Carbone, A. Kakizaki, and I. Matsuda

17) Direct mapping of the spin-filtered surface bands of a three-dimensional quantum spin Hall insulator
A. Nishide, A. A. Taskin, Y. Takeichi, T. Okuda, A. Kakizaki, T. Hirahara, K. Nakatsuji, F. Komori, Y. Ando, and I. Matsuda

6.2. Accelerator Studies

1) R&D Efforts of ERL Main Linac Superconducting Cavity
H. Sakai, T. Furuya, T. Takahashi, K. Umemori, K. Shinoe, N Nakamura, and M. Sawamura

2) Development of an Yb-Doped Fiber Laser System for an ERL Photocathode Gun
I. Ito, N. Nakamura, D. Yoshitomi, K. Torizuka, and Y. Honda

3) Tolerance Study on RF Amplitude and Phase of Main Superconducting Cavities and Injection Timing for the Compact ERL
N. Nakamura, M. Shimada, T. Miyajima, Y. Kobayashi, S. Sakanaka, and R. Hajima

4) Effects of Alignment Error of Main Superconducting Cavities on ERLs and their Compensation
N. Nakamura, K. Harada, M. Shimada, Y. Kobayashi, S. Sakanaka, and R. Hajima

5) Application of the Eigenvector Method with Constraints to Orbit Correction for ERLs
N. Nakamura and K. Harada

6) New Pulsed Power Supply for the Pulsed Sextupole Injection System at the PF Ring
H. Takaki, K. Harada, T. Honda, Y. Kobayashi, T. Miyajima, S. Nagahashi, N. Nakamura, T. Obina, M. Shimada, R. Takai, and A. Ueda

7) Performance Tests of a Phase Shifter Prototype for a Polarization-Controlled Undulator
N. Nakamura, I. Ito, K. Shinoe, T. Shibuya, H. Kudo, H. Takaki, K. Onoue, T. Tanaka, H. Kitamura, and T. Bizen

Staff

List of Publications

Preface

The Synchrotron Radiation Laboratory (SRL) consists of solid state spectroscopy and accelerator groups. The SRL have been taking part in the Synchrotron Radiation Research Organization (SRRO) of the University of Tokyo since 2005, and operating a new beamline (BL07LSU) at the SPring-8 and experimental apparatuses in SX region. The beamline has a 27m-long polarization-controlled undulator and a monochromator covering the photon energy range from 250 eV to 2 keV. The undulator consists of eight segments of Figure-8 undulator, four of which are for SR with horizontal polarization and others for vertical ones, the installation of which was completed in the summer of 2010. To control the polarization we have installed seven phase-shifters between horizontal- and vertical-polarization undutlators, some parts of which were developed by the accelerator group of SRL. The beamline at the SPring-8 was fully opened to users since 2009 and members of solid state spectroscopy group of SRL play an essential role to promote advanced materials sciences utilizing high brilliance SR from the new undulator.

The staff members of SRL also maintain three beamlines (BL18A, BL19A and 19B) in the Photon Factory (PF). In 2009, the quality of the monochromator at BL19A was improved by adjusting the alignment of optical elements. The new spin- and angle-resolved photoelectron spectrometer at this beamline attracted attentions of many users and fully occupied by those from China, Korea and other countries. The members of the accelerator group SRL have been working in collaboration with Japan Atomic Energy Agency (JAEA) and High Energy Accelerator Research Organization (KEK) to develop a new accelerator system, an energy recovering linac (ERL), a prototype of which is in construction at KEK as a new light source in VSX region.

October 20, 2010

Akito Kakizaki

Director of SRL-ISSP

1 Status of Beamlines at the Photon Factory, KEK

1.1. Beamline 18A

The beamline 18A has been dedicated to photoemission experiments to investigate electronic structures of surfaces and interfaces of metals, semiconductors and those of adsorbed by various atoms and molecules. The beamline is equipped with a constant deviation angle grazing incidence monochromator. The monochromator covers the photon energy range from 15 to 170 eV with resolving power of more than 1000.

At the end-station, two commercial angle-resolved photoemission spectrometers are installed. The one is VG ADES500. The other is VG Scienta SES-100 with the rotational flange and the linear transfer mechanism. By the installation of Scienta SES-100, the end-station now provides opportunities of photoemission experiments such as, , k_x, k_y, k_z-band mapping, k_x, k_y, k_z Fermi surface image with high energy (2.2 meV) and angle resolution (<0.2^o), and polarization dependent measurements.

At the sample preparation chamber, samples can be heated by a direct current heating or electron bombardment, and cooled by a closed cycle He Cryostat down to 50 K. By the load-lock and sample transfer systems, samples can be changed without breaking ultra high vacuum (UHV). Evaporators also can be replaced without breaking UHV by a system combined valves and differential pumping. The other surface evaluating and preparing apparatuses, LEED, XPS, Sputter-gun, Quadrupole mass spectrometer, quartz thickness monitor are also equipped.

Recent works performed at this beamline were Fermi surface and band mappings by angle-resolved photoemission (ARPES) measurements of (1) surfaces and thin films with strong spin-orbit interaction inducing the Rashba effect, (2) one-dimensional system or nano-scale materials fabricated on Si surfaces by metal or gas adsorption, (3) magnetic materials such as magnetic semiconductor or transition metal silicides, and so on.

1.2. Beamline 19A

The beamline 19A is an undulator beamline equipped with a constant deviation angle grazing incidence monochromator and covers the output photon energy from 20-250 eV and is dedicated to the spin- and angle-resolved photoemission (SARPES) experiments. The quality of the monochromator at BL19A was improved by adjusting the alignment

of optical elements in 2009.

At the end-station of this beamline, a high-energy resolution photoelectron analyzer (PHOIBOS 150, SPECS GmbH) is equipped together with high efficient spin detector associating very low energy electron diffraction (VLEED). The system is designed to provide high stability, high-energy resolution and high efficiency of spin detection for spin-resolved photoemission experiments. The end-station also consists of a manipulator with He cryostat (<60 K), a preparation chamber equipped with surface preparation apparatuses (LEED, AES, sputter-gun and others) and a load-lock chamber. The new spin polarimeter achieved approximately 100 times higher efficiency than a conventional Mott detector. The figure of merit of it is about 1.9×10^{-2} with Sherman function of 0.4, which enables us to measure SARPES spectra with relatively high-energy resolution (~60 meV). Figure shows the new SARPES system at BL19A.

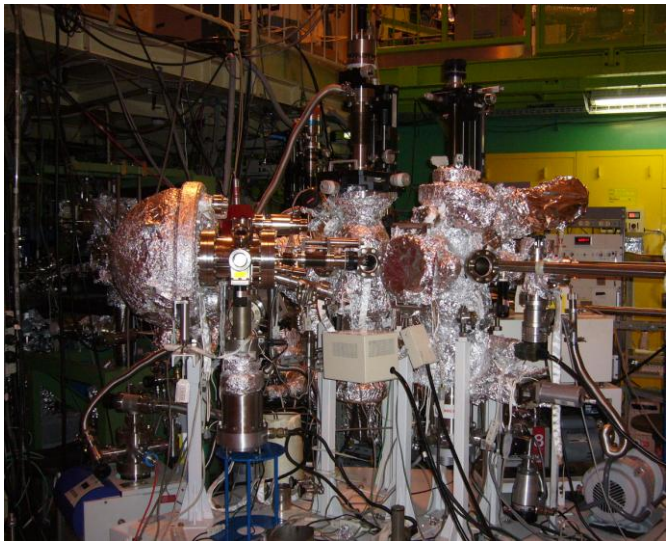

Recently, the new spin system has been utilized to obtain precise information on spin-dependent electronic structures of surfaces and thin films with strong spin-orbit interaction inducing the Rashba effect and topological insulators.

At the beamline 19A, onventional spin- and angle-resolved photoelectron spectroscopy measurements by the small Mott detector (25 keV), the synchrotron radiation illuminated scanning tunneling microscope (SR-STM) measurements and photoemission electron microscopy (PEEM) are also available.

1.3. Beamline 19B

The beamline 19B is an undulator based soft X-ray beamline. In this beeamline, measurements of X-ray emission spectroscopy (XES), X-ray absorption spectroscopy (XAS) and X-ray photoemission spectroscopy (XPS) are available. This beamline has a plane grating monochromator with varied line spacing plane gratings (VSPG). The available photon energy is from 70 to 1100eV. At the end-station, a soft X-ray emission

spectrometer and an angle-integrated photoemission spectrometer (CLAM4, $E/\Delta E$= 50~200) are installed. X-ray absorption can be measured by the two ways; the electron yield using the sample current, the photon yield using the Si-photodiode. Samples can be cooled down to 20 K using a manipulator with a He-refrigerator. The soft X-ray emission spectrometer is Rowland-circle grating emission spectrometer. It has a fixed (100 μm) entrance slit and two interchangeable gratings to cover the photon energy from 50 to 1200 eV. The energy resolution of the XES is about 70 meV at 100 eV. Recently, we have improved the software for the emission spectra measurement, which makes it possible to analyze the emission image data with higher energy resolution.

2. Status of Beamline BL07LSU at the SPring-8

Since foundation of the Synchrotron Radiation Research Organization in the University of Tokyo in 2006, members of the synchrotron radiation laboratory have particiapted in a project to construct a new high-brilliant soft X-ray beamline BL07LSU, University-of-Tokyo Synchrotron Radiation Outstation Beamline, with a 27-m-long undulator at SPring-8 with collaborations of Japan Synchrotron Radiation Research Institute and RIKEN. We set up the Harima branch at SPring-8 with two permanent staffs and an adjunct.

The long undulator was designed to cover the photon energy range of 250~2000 eV and to generate circularly and linearly polarized soft X-rays with the fast switching. It consists of the eight figure-8 undulators (the four horizontal polarization type and four vertical polarization type) with seven phase shifters. The beamline BL07LSU is aimed to realize advanced spectroscopy such as nano-beam photoemission spectroscopy, time-resolved spectroscopy, and ultra-highresolution soft X-ray emission spectroscopy. These experiments require a high energy resolving power ($E/\Delta E>10^4$),high photon flux ($>10^{12}$ photons/s/0.01%B.W.), and a small beam size of a few microns at the sample position. To achieve these conditions (Table 1), an entrance-slitless variable-included-angle Monk-Gillieson mounting monochromator with a varied-line-spacing plane grating has been employed at the beamline BL07LSU.

The four figure-8 undulators of the horizontal polarization type and the three phase shifters were installed at the SPring-8 storage ring in august in 2008, Fig.1 and 2, and the whole beamline was assembled in 2009, Fig.3, with the four experimental endstations. The first beam at the beamline was identified at the beginning of October 1 and the opening ceremony was held on October 9, Fig.4. The beamline has been opened for users since November in 2009 and it has now become a research site for frontier spectroscopy experiments with high-brilliant soft x-ray.

Table1: Optical Specifications at BL07LSU

Photon energy: 250~2000 eV
Photon Flux: > 10^{12} photons/s
Resolution, $E/\Delta E$: > 10,000
Spot size: < 10 μm
Polarization: circular, linear

Fig.1 Four figure-8 undulators in the SPring-8 storage ring.

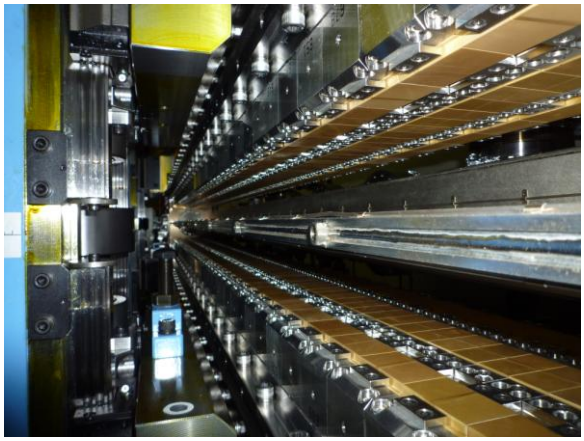

Fig.2 Arrangement of magnets in the figure-8 undulator.

Fig.3 The beamline BL07LSU

Fig.4 The opening ceremony on October 9, 2009.

3. Activities of Accelerator Group

3.1. Accelerator Research and Development

Development of ERL accelerator components was in progress. The first prototype of the ERL main superconducting(SC) cavity could reach the accelerating field of 25 MV/m, after a tip that might cause field emission at high fields was polished and the inner surface was refreshed by the electro-polishing(EP). The second prototype was also fabricated. For an input coupler of the ERL main SC cavity, the ceramic window design was modified by changing the ceramic thickness from 6.2 to 5.4 mm to sufficiently deviate the resonant frequency of the dipole mode standing on the choke of the ceramic window from the accelerating frequency of 1.3 GHz and a cold ceramic window was fabricated according to the new design. As a result the target input power of 20 kW was successfully input to the new ceramic window (Fig.1). Design of a cryomodule and HOM damper is on going.

A 10-W fiber laser amplifier using an Yb-doped photonic crystal fiber was successfully developed as a part of a drive laser system for an ERL photocathode gun. The nonlinear optical effects that cause pulse distortion were well suppressed in the amplifier. The second harmonic generation was demonstrated using output of the developed 10-W amplifier and a LBO crystal and the second harmonic (518 nm) of 4.8 W was generated by the conversion efficiency of 49 % (Fig. 2). Furthermore the active harmonic mode-locking Yb fiber laser oscillator was developed to achieve the pulse repetition rate of 1.3 GHz. We could already generate a 421-MHz pulse train.

Error effects and their compensation were studied for a compact ERL model that has eight main SC cavities with the acceleration field of 15 MV/m. Individual tolerances for RF amplitude and phase errors of main SC cavities and injection timing jitter were studied with simulation for the compact ERL. From the simulation result, required stability for RF control and injection timing was obtained for three operation modes. Effects of alignment error of the main SC cavities on the ERL beam were also evaluated and as a result it was found that orbit distortion, emittance growth and bunch lengthening due to the alignment error could be significant. However they could be almost compensated for the alignment error up to 1 mm by sophisticated orbit correction using the eigenvector method with constraints that we had originally formulated.

For a pulsed sextupole magnet(PSM) installed in the PF ring, a new power supply was fabricated to improve the injection efficiency. The new power supply has a pulse width of

about twice the revolution period, which is shorter by a factor of two than that of the old one. Beam injection study using the new power supply is underway.

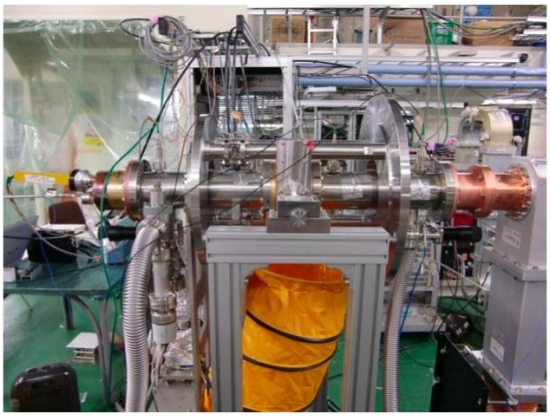

Fig. 1 High power test of a new ceramic window for an ERL superconducting cavity.

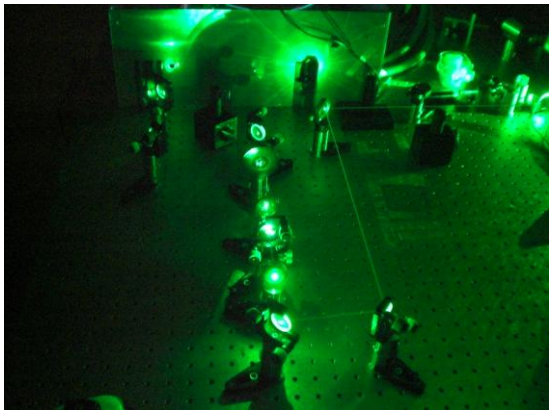

Fig. 2 Development of a drive laser system for an ERL photocathode gun.

3.2. Development of phase shifter for fast helicity switching

An electromagnetic phase shifter prototype for fast helicity switching of the polarization-controlled undulator that is under construction for the material-science beamline (BL07LSU) of the University of Tokyo at SPring-8 has been developed and tested at ISSP. We confirmed that the field reproducibility of the permalloy yoke is very high due to the ultra-low hysteresis as compared with that of a yoke made of the 0.1-mm-thick silicon-steel laminations. Frequency response of the phase shifter prototype with and without the stainless-steel vacuum duct was measured and compared with the result of 3-D magnetic field analysis for evaluating effects of eddy currents of the vacuum duct. The residual AC field integral of the phase shifter prototype in RMS was measured by a long coil system at excitation frequencies of 10-Hz and 100-Hz and could be reduced down to less than 1 G·cm by adjusting the output currents of three power supplies. This means that the phase shifter can suppress the electron beam movement due to the residual AC field integral down to submicron level for the fast helicity switching.

4. Workshops & Meetings

ISSP workshop "Development of material science by frontier spectroscopy with brilliant VSX source"

Date: July 23-24, 2009

Place: Lecture Room (A632), 6th Floor, ISSP

Recently there have been remarkable progresses in experimental researches with high-brilliant vacuum ultraviolet ~ soft X-ray (VSX) synchrotron radiation sources. Among the various frontier VSX spectroscopy techniques, the present workshop focused on 1) soft X-ray emission spectroscopy, 2) time-resolved soft X-ray spectroscopy, and 3) nanometer-region spectroscopy. Twenty six scientists were invited to present their recent investigations and they discussed the experimental advances with the audience. The workshop was composed of the following sessions.

1) Status and future of nano-spectroscopy methods

2) High resolution soft X-ray emission spectroscopy and the future developments

3) Real time observations by time-resolved soft X-ray spectroscopy and imaging techniques

4) Researches on electronic properties of organic devices

5) The University-of-Tokyo Synchrotron Radiation Outstation Beamline

In the session 5), schedule and design of a new high-brilliant soft x-ray beamline, SPring-8 BL07LSU, that would be constructed at SPring-8 in October, 2009, were described. Posters of the beamline and the experimental end-stations were also exhibited at the site. The participants, especially young scientists, showed their high expectations for the state-of-the-art spectroscopy techniques with new high-brilliant photon sources and they engaged in a lively exchange of opinions regarding the future experiments through the workshop.

Program

July 23

13:00- **Opening Address**
Jun Yoshinobu (Institute for Solid State Physics, the University of Tokyo)

13:10- **University-of-Tokyo Synchrotron Radiation Research Organization and UT SR Outstation**
Masaharu Oshima (SRRO, The University of Tokyo, The University of Tokyo)

13:30- **Cooperative user beamtime of the SRRO beamline BL07LSU at SPring-8**
Akito Kakizaki (ISSP, the University of Tokyo SRRO, the University of Tokyo)

13:50- **Present status of soft X-ray beamline BL07LSU at SPring-8**
Yasunori Senba and Haruhiko Ohashi (SPring-8)

14:10- **Post focus mirror system at Spring8 BL07LSU**
Masami Fujisawa (ISSP, the University of Tokyo SRRO, the University of Tokyo)

14:30- **Coffee Break**

14:50 **Development of three-dimensional scanning photoelectron microscope (3D nano-ESCA)** Koji Horiba[1](The University of Tokyo)

15:10- **Development of adaptive optical system for hard X-ray nanofocusing**
Hidekazu Mimura (Osaka University)

15:30- **Development of time-resolved micro XMCD measurement using hard X-rays for characterization of magnetic microstructures**
Motohiro Suzuki (JASRI/SPring-8)

15-50- **Principle, present status, and future prospect of the generation of the soft X-ray microbea** Kenta Amemiya (KEK)

16:10- **Imaging of Nano Materials Using Soft X-ray Spectro-Holography**
Kanta Ono (KEK)

16:30- **Outlook of nanospectroscopy in SPring-8 using photoelectron emission microscope** Masato Kotsugi (SPring-8/JASRI)

16:50- **X-ray nanospectroscopy using photoelectron emission microscopy**
Kanta Ono (KEK)

17:10- **Analysis of surface and electronic structure by a new two-dimentional photoelectron microscopic spectrometer**
Hiroshi Daimon (Nara Institute of Science and Technology)

17:30- **X-ray Raman Scattering Study of Ti-Oxides.**
Yasuhisa Tezuka (Hirosaki Universitz)

July 24

9:30- **Ultra-high resolution soft X-ray emission : a challenge to bio-materials science**
Yoshihisa Harada (Department of Applied Chemistry, the University of Tokyo SRRO)

9:50- **Resonant Soft-X-Ray Inelastic Scattering of Perovskite-Type Fe Oxide**
Tohru Higuchi (Department of Applied Physics, Tokyo University of Science)

10:10- **Study of the structure in perovskite titanates under the electric field**
Nobuo Nakajima (Hiroshima University)

10:30- **Site-specific observation of valence electronic structures at solid-solid interfaces: soft x-ray absorption and emission study**
Yoshiyuki Yamashita (National Institute for Materials Science)

10:50- **Coffee Break**

11:10- **Toward experiments of two-dimensional photoemission spectroscopy by high-brilliant soft X-ray**
Iwao Matsuda (The Institute for Solid State Physics, the University of Tokyo)

11:30- **Time-resolved photoemission electron microscopy observation combined with pump &probe method** Toyohiko Kinoshita (JASRI/SPring-8, JST-CREST)

11:50- **Time-resolved Photoemission Study at SAGA-LS**
Kazutoshi Takahashi (Saga university)

12:10- **lunch**

13:30- **Attempt to probe atoms and molecules in an intense laser field with SR**
Jun-ichi Adachi（KEK)

13:50- **Synchrotron-based time-resolved spectroscopy for molecular adsorption system** Hiroshi Kondoh (Keio University)

14:10- **Observation of the electronic structures of organic thin films and single crystals by photoelectron yield spectroscopy in various environments**
Hisao Ishii (Center for Frontier Science, Chiba University)

14:30- **Electronic properties of highly ordered organic thin films and interfaces**
Hiroyuki Yamane (Institute for Molecular Science)

14:50- **Photoelectron spectroscopy for organic molecular assembly: In terorbital interaction and electronic structure** Kera Satoshi (Chiba University)

15:10- **Elucidation of Electronic Structure of Electronic Functional Organic Materials by Soft X-ray Emission Spectroscopy**
Kaname Kanai (Okayama University)

15:30- **Perspectives of a high-brilliant VSX beamline for study of structures, electronic structures, and dynamics of organic thin films**
Kazuhiko Mase (KEK)

15:50- **Closing Address**
Masaharu Oshima (SRRO, the University of Tokyo, the University of Tokyo)

ISSP workshop "New opportunities in VUV Solid State Spectroscopy by improving PF BL19 undulator beamline"

Date: December18, 2009
Place: Lecture Room (A632), 6th Floor, ISSP

In this ISSP workshop, we have discussed the renovation of PF BL19 undulator beam line and new opportunities in condensed matter physics using VUV spectroscopy. New designs including an electromagnetic undulator and a monochrometer for PF BL19 were proposed. The current statuses of VUV beamlines in Japan were also reported. In addition, several state-of-the-art experiments using VUV spectroscopy were presented.

The undulator beam line BL-19 at Photon Factory (PF) was developed by the Institute for Solid State Physics in 1986. It has been the joint-research site of VUV spectroscopy and a great number of researchers over the world have made interesting experiments. To meet their further needs of the better performance as the VUV source, we have organized this ISSP workshop to discuss the renovation of PF BL19 and new opportunities in condensed matter

physics using high-brilliant VUV spectroscopy. New designs including an electromagnetic undulator and a high-resolution monochromator for PF BL19 were proposed. The current statuses of VUV beamlines in Japan were also reported by beamline managers of other facilities. In the workshop, researchers, including users of BL-19, introduced their recent works and presented their state-of-the-art VUV spectroscopy measurements. Possible new experiments were vigorously discussed by the participants with high expectations of the BL-19 renovation project.

Program

10:00- **Opening Address**
Akito Kakizaki (Institute for Solid State Physics, the University of Tokyo)

10:20- **Renewal Plan for Optical System of BL19**
Masami Fujisawa (Institute for Solid State Physics, the University of Tokyo)

10:40- **Design study of a new BL#19 undulator with an electro-magnet option at the Photon Factory, KEK** Shigeru Yamamoto (KEK)

11:00- **Status of low energy Beamlines at UVSOR-Ⅱ** Shin-ichi Kimura (UVSOR)

11:20- **Status of low energy Beamlines at HiSOR**
Akio Kimura (Hiroshima University)

11:40- **lunch**

13:00- **A new horizon in spin-resolved photoelectron spectroscopy; from COPHEE to ESPRESSO** Taichi Okuda (HiSOR, Hiroshima University)

13:20- **Peculiar Rashba effect caused by the symmetry of the surface**
Kazuyuki Sakamoto (Chiba University)

13:40- **The Rashba-type spin-splittings of Bi or Pb-adsorbed Ge(111) surfaces**
Shinichiro Hatta (Kyoto University)

14:00- **Coffee Break**

14:20- **Controlled electron doping into metallic wires; the case of Si(111)4×1-ln**
Harumo Morikawa (Yonsei University)

14:40- S**train Induced Modification of Metallic Surface State on Reconstructed Structure of Semiconductor Surfaces**
Yukichi Shigeta (Yokohama Citiy University)

15:00- **Electronic structure of Au adsorbed Ge surfaces**
Kan Nakatsuji ((Institute for Solid State Physics, the University of Tokyo)

15:20- **Coffee Break**

15:30- **Electronic-state studies of metal hydrides**
Daiichiro Sekiba (Tsukuba University)

15:50- **Analysis of enhanced silicon oxidation just below titanium thin films**
Sinya Ohno (Yokohama National University)

16:10- **The questionnaire results on upgrading the undulator beamline BL-19 at Photon Factory**
Iwao Matsuda (Institute for Solid State Physics, the University of Tokyo)

ISSP workshop “New opportunities in VUV Solid State Spectroscopy by improving PF BL19 undulator beamline” at ISSP

5. Seminar

Date: July 17, 2009
Title: Picosecond timing control of laser and SR pulses for time-resolved X-ray diffraction
Speaker: Dr. Yoshihito Tanaka (RIKEN)

Date: October 5, 2009
Title: Surface Magnon Studies by Spin-Polarized Electron a Energy Loss Spectroscopy
Speaker: Dr. Jürgen. Kirschner (Max-Planck-Institute für Mikrostrukturphysik, Germany)

Date: November 9, 2009
Title: Current studies on chemical reactions at surfaces and interfaces using synchrotron radiation and expected future progress
Speaker: Dr. Hiroshi Kondoh (Keio University)

Date: November 9, 2009
Title: Dynamics of Surface Chemical Reactions Studied by Time-Resolved Soft X-ray Spectroscopy
Speaker: Dr. Susumu Yamamoto (Institute for Solid State Physics, the University of Tokyo)

Date: November 25, 2009
Title: Interface atomic structure of mid-gap coulomb blockade of silicide type nanostructure
Speaker: Dr. Hisashi Narita (Institute for Solid State Physics, the University of Tokyo)

6. Activities

Measurement of the intermolecular band dispersion in multilayer guanine assemblies

Rainer Friedlein, Ying Wang, Antoine Fleurence, Yukiko Yamada-Takamura

School of Materials Science & Research Center for Integrated Science, Japan Advanced Institute of Science and Technology (JAIST)

The nature of charge migration in deoxyribonucleic acid (DNA) has been studied for almost 50 years [1], mainly for biological reasons. A detailed understanding is important since oxidation and reduction of the DNA bases are the main steps in the DNA damage process [2]. Recently, the possibility to use DNA in molecular electronics has triggered an extensive study of the subject also among physicists [3–6]. Still, due to the particular complexity involved in both experiments and theoretical modeling, the fundamental question whether the DNA molecule is an electrical conductor or not remains controversial. Among the four nucleic acids constituting the DNA molecule, guanine has the lowest ionization potential and may therefore be responsible for charge carrier trapping [6]. Such trapping may be prevented in quasi-one-dimensional assemblies of a single constituent.

Guanine multilayer films were prepared in a home-based set-up by vapor deposition under ultrahigh vacuum conditions [7], the substrate held at 80 °C. Exposure to water vapor at 10^{-4} Torr for 30 min was carried out in a separate chamber equipped with a leak valve connected to a glass vial containing distilled water. Guanine grows on graphite in a layer-by-layer mode where molecules are flat with respect to the substrate surface. Intermolecular hydrogen bonds stabilize the network. While some hydrogen bonds are affected upon hydration [7], the structural integrity is maintained.

The sample has then been transferred in air to the ISSP beamline 18A of the Photon Factory synchrotron radiation facility located in Tsukuba, Japan. The intermolecular band dispersion has been measured using photon-energy dependent ultraviolet photoelectron spectroscopy in the direction normal to the substrate surface.

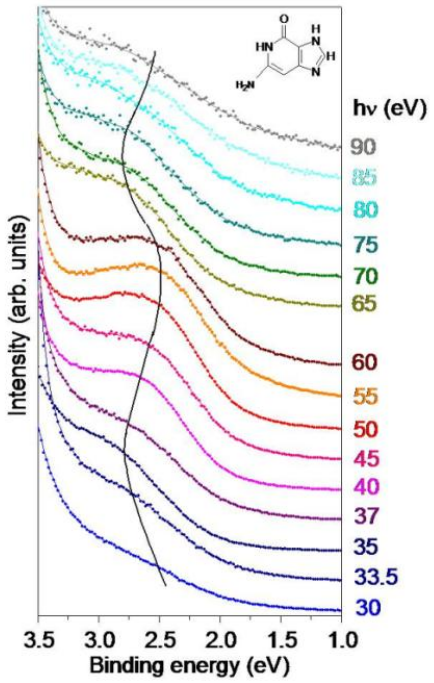

Figure 1: Photon-energy dependent UPS spectra of the hydrated multilayer recorded in the binding energy region of electronic states related to the guanine HOMO.

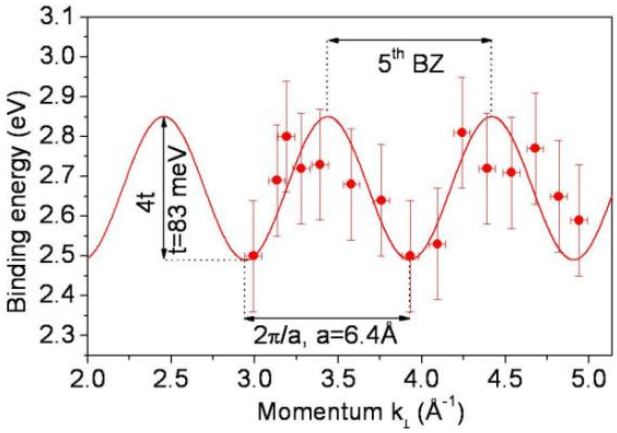

Figure 2: Experimental peak positions of the spectral feature related to the guanine HOMO (dots) as a function of the out-of-plane electron momentum, $k_\perp$, and a fit of the dispersion around the 5th Brillouin zone (BZ) using a one-dimensional tight-binding model (solid line).

Photon-energy dependent spectra of a first hydrated and then air-exposed multilayer film are plotted within the low-binding energy region in Fig. 1. At energies in between about 2 and 3 eV, a clearly recognizable, strongly-dispersing spectral feature develops into a distinctive peak at intermediate photon energies hν, and is assigned to electronic states related to the HOMO. The dispersion can clearly be traced over two periods and is evidence for the formation of at least one intermolecular band or of the parallel dispersion of several bands predicted for the guanine monohydrate crystal [5]. As discussed theoretically [6,7], a large band width can only be obtained for optimal geometries where guanine molecules face each other in a flipped configuration, with a vanishing in-plane rotation with respect to each other.

Applying a one-dimensional tight-binding model $E_B(k\perp)=E_B^0-2t\cos(k\perp a)$ to fit the experimental data points, as shown in Fig. 2, parameters related to the intermolecular band dispersion are derived: the position of the center of the band of E_B^0=2.67 eV, a band width of 331±8 meV corresponding to a π-π overlap (or transfer) integral of t=83±2 meV, and the length of the unit cell consisting of two molecules along the stacking direction of a=6.4±0.1 Å.

These values provide an intrinsic hole mobility μ_h at room temperature of larger than 18 cm^2/Vs along the stacking direction. With this work [8], hydrogen-bound, self-assembled thin films made of relatively small heterocyclic molecules emerge as a new class of materials with excellent and highly anisotropic transport properties.

Experimental help from A. Harasawa (ISSP) and support from Special Coordination Funds for Promoting Science and Technology, commissioned by MEXT, Japan, is acknowledged.

References

[1] D.D. Eley, D. I. Spivey, Trans. Faraday Soc. **58** (1962), 411.
[2] P. J. Dandliker, M. E. Núñez, J. K. Barton, Biochemistry **37** (1998), 6491.
[3] H.W. Fink and C. Schönenberger, Nature (London) **398** (1999), 407.
[4] D. Porath, A. Bezryadin, S. De Vries, C. Dekker, Nature (London) **403** (2000), 635.
[5] F. Ortmann, K. Hannewald, F. Bechstedt, J. Phys. Chem. B **112** (2008), 1540.
[6] R. Di Felice, A. Calzolari, E. Molinari, A. Garbesi, Phys. Rev. B. **65** (2001) 045104.
[7] W. J. Doherty III, S. L. Sorensen, R. Friedlein, J. Electr. Spectr. Relat. Phenom. **174** (2009), 107.
[8] R. Friedlein, Y. Wang, A. Fleurence, F. Bussolotti, Y. Ogata, Y. Yamada-Takamura, submitted.

Electronic structure of the α-Bi/Si(111)-(√3×√3) surface

Yuta Yamamoto[1], Takuya Kuzumaki[1], Yusuke Tanaka[2], Kunihiro Hotta[1], Ayumi Harasawa[3], Nobuo Ueno[1], Kazuyuki Sakamoto[1*]

[1]*Graduate School of Advanced Integration Science, Chiba University, Chiba 263-8522, Japan*

[2]*Department of Chemistry, Nagoya University, Nagoya 464-8602, Japan*

[3]*The Institute for Solid State Physics, the University of Tokyo, Chiba 277-8581, Japan*

The electronic structure of a 1/3 monolayer Bi adsorbed Si(111)-(√3×√3) surface (the α-phase) has been investigated by angle-resolved photoemission measurement. A large Rashba spin splitting with a Rashba parameter (α_R) of 2.2 eVÅ was observed at the $\bar{\Gamma}$ point.

Introduction

On a two-dimensional (2D) system such as surface, a spin polarized 2D electron structure that originates from a combined effect of structural inversion asymmetry (SIA) and spin-orbit interaction (SOI) is formed even for nonmagnetic materials. This effect, which is called the Rashba-Bychkov (RB) effect [1] or simply Rashba effect, is the key concept for spintronic devices, devices that use the spin degree of freedom of an electron in addition to its charge to add substantially new functionalities in electronic devices. The RB effect was observed on clean surfaces of noble metals [2] and heavy group V elements [3], and has reported to be enhanced in systems in which heavy element atoms are adsorbed on light element substrates [4]. The heavy element Bi adsorbed light element Si surface is a candidate to show exotic RB effect. Bi adsorption induces two different (√3×√3) phases on Si(111) depending on the coverage. The (√3×√3) surface formed at a coverage of 1 monolayer (ML) is called the β-phase, and the one formed at 1/3 ML is called the α-phase (the atomic structures of the two phases are shown in Fig. 1 [5]). Of these two phases, the β-phase has been reported to show peculiar RB splitting that originate from the C_{3v} symmetry of this surface [6]. The α-phase has the same symmetry, and thus has possibility to show interesting phenomena as well. Further, a study on systems that are formed by the same elements and have the same symmetry but with different adsorbate coverage would give important information about the origins of the exotic RB effects.

Experimental details

The angle-resolved photoelectron spectroscopy (ARPES) measurements have been performed at BL18A of KEK-PF, using a photon energy of 40 eV. In order to obtain a clean surface, the sample was annealed at 1520 K by direct resistive heating in the vacuum chamber. After the annealing, the sample showed a sharp (7x7) LEED pattern with low background intensity, and no trace of contamination has been observed in the photoelectron spectra. The α-Bi/Si(111)-(√3×√3) (hereafter α-√3) surface was prepared by depositing Bi on a clean Si(111) surface at a substrate temperature of 600 K, followed by an annealing at 900 K. The formation of the α-√3 surface was confirmed by LEED and photoemission.

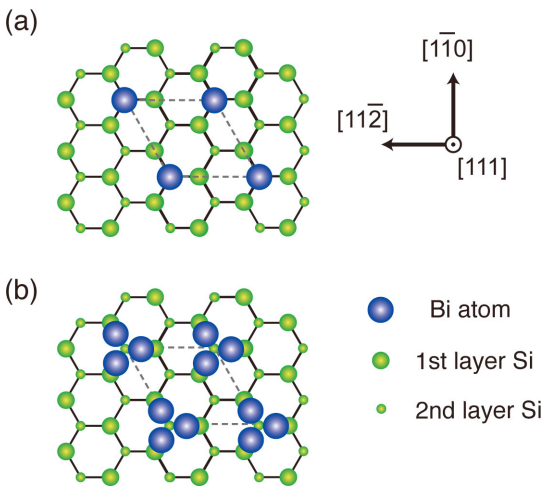

Figure 0: Schematic illustrations of (a) the α-Bi/Si(111)-(√3×√3) surface and (b) β-Bi/Si(111)-(√3×√3) one.

- **Results and Discussion**

Figure 2(a) shows the surface Brillouin zones (SBZs) of the Si(111)-(1x1) and α-√3 surfaces, and the energy band structure of α-√3 measured along the $\bar{\Gamma}-\bar{M}$ direction is shown in Fig. 2(b). A large RB splitting is clearly observed in Fig. 2(b) at the $\bar{\Gamma}$ point. The momentum offset of the band top (k_0) is ca. 0.09 Å^{-1}, and the Rashba energy (E_R; the energy difference between the band top and the binding energy at the $\bar{\Gamma}$ point) is ca. 0.1 eV. By using these value and the relation between the Rashba parameter (α_R) and k_0 and E_R, $\alpha_R \sim 2E_R/k_0$, we obtained α_R~2.2 eVÅ. This value is almost the same as that of the RB splitting observed at the $\bar{M}$ point on the β-phase (2.3 eVÅ) [6] though the Bi coverage is quite different on the two surfaces. This result suggests that the amount of adsorbate would not contribute to the origin of the large RB effect observed on heavy element adsorbed light element substrates.

- **Summary**

We have investigated the electronic structure of the α-√3 surface by ARPES. A large Rashba spin splitting with α_R~2.2 eVÅ, whose value is almost the same as that of the RB splitting observed on the β-phase, was observed at the $\bar{\Gamma}$ point.

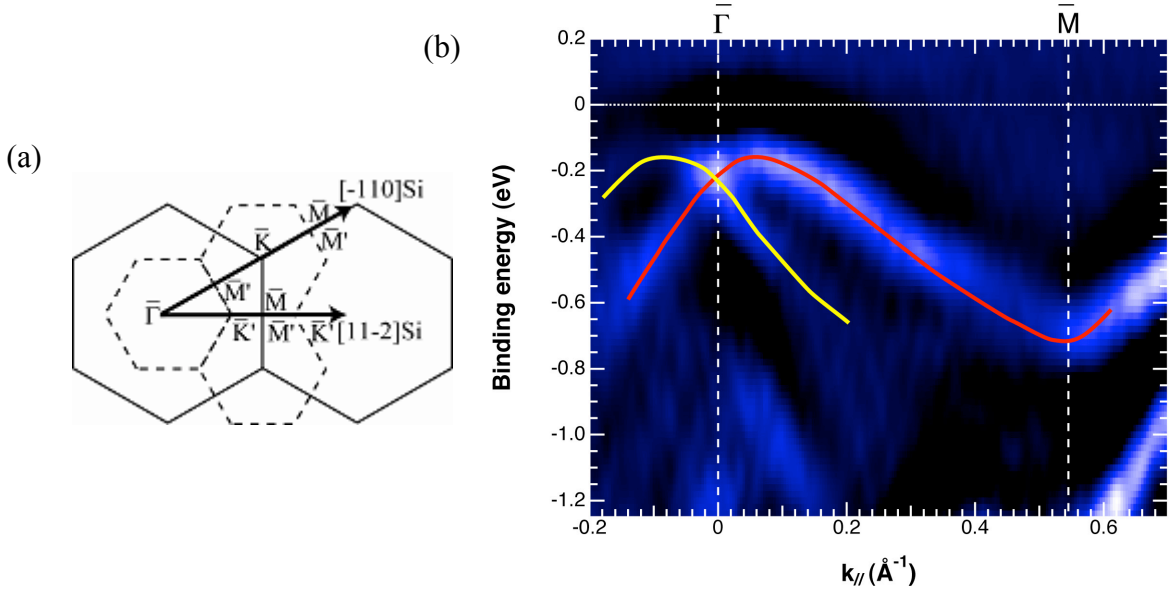

Figure 2: (a) Surface Brillouin zones (SBZ's) of Si(111)-(1x1) (solid lines) and (√3x√3) (dashed lines). (b) Band structure of the α-√3 surface measured using a photon energy of 40 eV.

References

[1] Y.A. Bychkov and E.I. Rashba, JETP Lett. **39**, 78 (1984).
[2] *see for example,* S. LaShell, B. A. McDougall, and E. Jensen, Phys. Rev. Lett. **77**, 3419 (1996).
[3] *see for example,* Yu.M. Koroteev *et al.*, Phys. Rev. Lett. **93**, 046403 (2004).
[4] C. R. Ast *et al.*, Phys. Rev. Lett. **98**, 186807 (2007).
[5] T. Kuzumaki et al., Surf. Sci. **604**, 1044 (2010).
[6] K. Sakamoto *et al.,* Phys. Rev Lett **103**, 156801 (2009).

EFFECT OF STRAIN ON ELECTRONIC STATES OF √3×√3-Ag STRUCTURE ON THE (111) SURFACE OF Si/Ge SYSTEM

Izumi MOCHIZUKI, Ryota NEGISHI, Yukichi SHIGETA

Nanoscience and Technology International Graduate School of Arts and Sciences, Yokohama City University.

It is very important to investigate electronic states of nanostructures creating new devices. The electronic state of the nanostructure depends on its structure involving the lattice strain to stabilize the nanostructure. To make clear the relation between electronic states and strain in nanoscale, the study in two-dimensional system is very useful and the results will give possibilities for nano-electronics applications. To control the strain in the surface lattice, we have selected the √3×√3-Ag (hereafter √3) structure which is typically formed on both surfaces of Si(111) and Ge(111) by a Ag adsorption[1,2]. Since the lattice constant of Si is about 4 % smaller than that of the Ge[3,4], the compressive strain is induced in the Ge layer grown on the Si(111) and the tensile strain is induced in the Si layer on the Ge(111) such as a Ge/Si(111) and a Si/Ge(111)[5,6].

We focused on the quasi two-dimensional electron gas (2DEG) state formed on the √3×√3-Ag structure, because the dispersion of the 2DEG state could be modified with the lattice strain introduced by hetero-epitaxial growth such as the Ge/Si(111) or the Si/Ge(111). We investigated that the electronic states of the compressive and tensile √3×√3-Ag structure on the Ge/Si(111) and Si/Ge(111) measured with a scanning tunnelling microscope (STM) and an angle resolved ultraviolet photoelectron spectroscopy (ARUPS).

The STM observations were performed in our laboratory (U-STM, ULVAC), and the ARUPS observations were performed in BL-18A (Institute for Solid State Physics, University of Tokyo). The STM images were taken in the constant-current mode with a tunnel current I_t, of 50 pA and several sample bias voltages V_s, at room temperature (RT). All ARUPS spectra were measured with the polarized light with the photon-energy of 21.2 eV at low temperature (about 120 K). The angular resolution was less than 0.3°, which corresponds to 0.010 $Å^{-1}$ indicated by a wave number, and the energy resolution was less than 0.05 eV.

Figures 1(a)-(d) show the STM images: (a) the Si(111)-√3×√3-Ag surface, (b) the Si/Ge (111)-√3×√3-Ag surface (the S-√3Ag) with a coverage of Si at 1.0 BL and (d) the Ge/Si(111)-√3×√3-Ag surface (the Ge-√3Ag) with a coverage of Ge at 1.0 BL [5,6]. These images show a same feature from the honeycomb chained trimer (HCT) structure at RT [1], and we have confirmed that each electronic structure observed with the ARUPS is similar to each other.

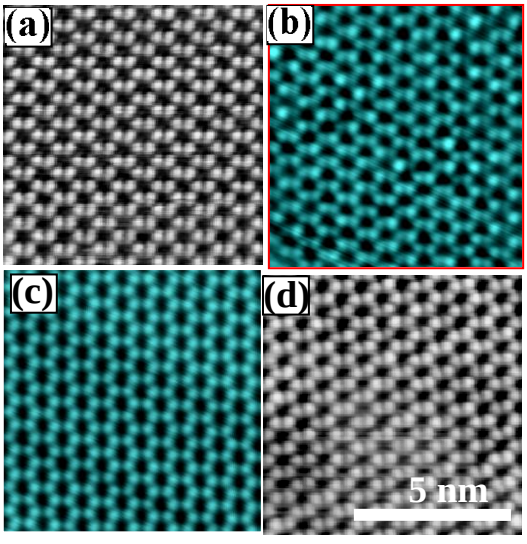

Fig. 1 RT-STM images of (a) Si(111) -√3×√3-Ag, (b) S-√3Ag surface with θ_S = 1.0 BL, (c) Ge(111)-√3×√3-Ag and (d) G-√3Ag surface with θ_G = 1.0 BL (8 × 8 nm^2). All STM images show a typical feature of the HCT structure.

We find the dispersion of the S_1 state on each √3 surface, which is a metallic band crossing the Fermi level, varies depending on θ_G. Figures 2 show gray-scale diagrams of the band dispersion for the S_1 state at (a) the Si(111)-√3×√3-Ag, (b) the S-√3Ag, (c) the Ge(111)-√3×√3-Ag and (d) the G-√3Ag. Since the dispersion depends on the amount of excess Ag atom (n_A), each value of excess Ag atom in (a) and (b) is 0.019 ML, and that in (c) and (d) is 0.015 ML. Each solid line indicates the position of the second $\overline{\Gamma}$ point of the √3×√3 Brillouin zone, whose wave number (k_Γ) are (a) 1.090 Å^{-1}, (b) 1.069 Å^{-1}, (c) 1.049 Å^{-1}and (d) 1.076 Å^{-1}, respectively.

The effective mass (m^*) is also estimated from the dispersion fitted by each parabolic function. m^*/m_e for each case are (a) 0.20 ± 0.02, (b) 0.26 ± 0.03, (c) 0.30 ± 0.04 and (d) 0.20 ± 0.02, respectively.

The relationship between the m^* and the lattice expansion is plotted with error bars in Fig. 3. The open and closed circles are values obtained from the √3 on the Si(111) and the Si/Ge(111), and the open and closed squares are obtained from that on the Ge(111) and the Ge/Si(111). The difference of m^* between on the Si(111) and on the Ge(111) is considered to be attributed to the difference in the n_A.

The relationship is consistent with a model called the "d-band model" [7] on some metal surfaces, qualitatively, in which the reactivity increases with an expansion of interatomic spacing of the lattice parallel to the surface due to an instability of electronic states by missing interaction between the wave functions.

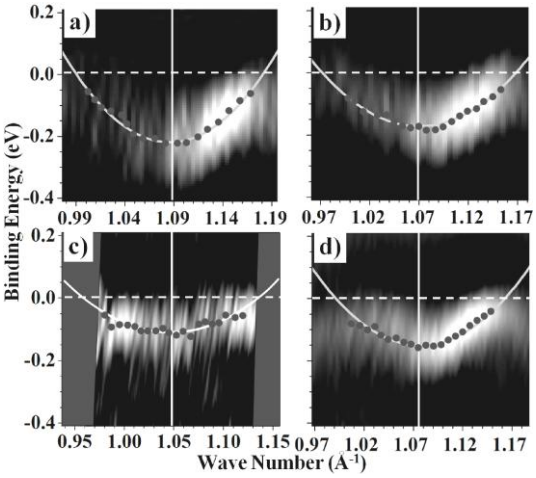

Fig. 2. Dspersions of the S_1 state with ARUPS from (a) the Si(111)-√3×√3-Ag, (b) the S-√3Ag, (c) the Ge(111)-√3×√3-Ag and (d) the G-√3Ag. Each value of excess Ag atom in (a) and (b) is 0.019 ML, and that in (c) and (d) is 0.015 ML.

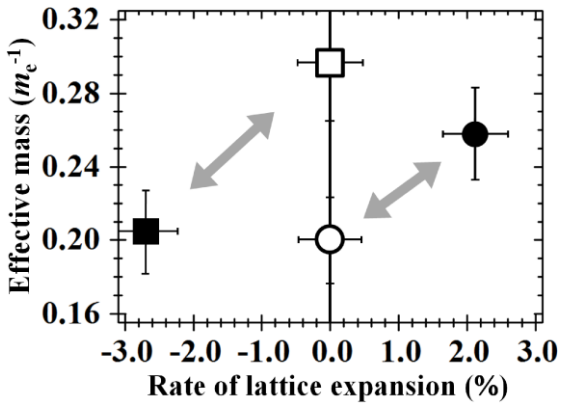

Fig. 3. Relation between m^* and lattice strain. The circles are results for the √3 structure from the Si(111) and the Si/Ge(111), and the squares are obtained from that on the Ge(111) and the Ge/Si(111) with error bars. The slope, $\Delta m^*/\Delta k_\Gamma$, is estimated to be about 3.1 m_eÅ.

References

[1] N. Sato et al., Surf. Sci. **442**, 65 (1999).
[2] H. M. Zhang, and R. I. G. Uhrberg, Surf. Sci. **546**, L789 (2003)
[3] E. A. Fitzgerald, et al., J. Vac. Sci. Technol. **B10**, 1807 (1992).
[4] P. W. Deelman, T. Thundat, and L. J. Schowalter, Appl. Surf. Sci. **104/105**, 510 (1996).
[5] I. Mochizuki, R. Negishi, and Y. Shigeta, J. Appl. Phys., **106**, 013709 (2009).
[6] I. Mochizuki, R. Negishi, and Y. Shigeta, J. Appl. Phys., **107**, 084317 (2010).
[7] D. Sekiba,et al. Phys. Rev. B **75**, 115404 (2007).

Effect of titanium on silicon oxide and titanium silicate formation processes on Si(001)

Shin-ya Ohno[1], Yuichi Ichikawa[1], Fumito Nakayama[1], Kazuaki Yamazaki[1],
Tomohiko Shimatsu[1], Masatoshi Tanaka[1],
Taichi Okuda[2], Ayumi Harasawa[2], Iwao Matsuda[2], Akito Kakizaki[2]
[1]*Department of Physics, Faculty of Engineering, Yokohama National University*

[2]*Synchrotron Radiation Laboratory, The Institute for Solid State Physics, The University of Tokyo*

Introduction

Recent applications of high-*k* gate dielectrics pose several problems, such as reduction of mobility, regardless of the dielectric material [1]. Mechanisms involving surface optical phonons [2] and remote charge scattering (RCS) [3] have been proposed. Ultrathin SiO_2 film with a thickness of about 1 nm is of vital importance, since it can be used as a buffer layer for the growth of high-*k* materials [4]. Hence, precise control of the thickness and interface morphology of the SiO_x interlayer below the high-*k* oxides appears to be critical. The objective of the present study was to develop a method to from a high quality SiO_x interlayer close to the stoichiometry of SiO_2 below the high-*k* oxides by means of exposure of metal-covered Si(001) to oxygen molecules. Exposure of a clean Si(001) to O_2 at room temperature (RT) leads to oxygen adsorption up to the Si dimer backbond site, limited to the monolayer regime (about 0.26 nm). In order to form thick oxide film, it is common to enhance reactivity of oxygen, thorough hyperthermal atomic oxygen with high translational energy [5], electron stimulated oxidation involving O^{2-} species [6] and alkali metals to promote oxidation [7].

Experimental

The x-ray photoemission spectroscopy (XPS) measurements were performed at BL-18A of the Photon Factory at the Institute of Materials Structure Science, High Energy Accelerator Research Organization (KEK-PF). With synchrotron x-rays at $h\nu$=130 eV, photoelectrons for the Si 2p state were detected using the SIENTA SES-100 electron energy analyzer. We measured Ti 2p and O 1s states using a conventional XPS apparatus. In both measurements, photoelectrons were collected at normal emission.

Results and discussion

Fig. 1 shows the Si 2p spectra. After deposition of titanium at RT, a broad peak was formed at around -0.4 eV, as shown in Fig. 1(b). No well-crystallized silicide island was observed just after deposition of titanium (0.3-0.4 nm) at RT, as confirmed in our scanning tunnelling microscopy (STM) studies [8]. According to the valence band measurements, only weak bonding between Ti and Si is possible through hybridization of Ti 3d and Si 3p states at this stage [9]. The large binding energy shift to 3.30 eV occurs after subsequent oxygen exposure of 60 L at RT (Fig. 1(c)). After oxidation, almost all the Si 2p component is shifted close to the Si^{4+} region. On the other hand, the surface component at around -0.5 eV diminishes after a larger amount of oxygen exposure at 750 L on clean Si(001), while only a weak tail is observed at the suboxide (Si^{+}, Si^{2+}, Si^{3+}) region. In contrast, no distinct peak is discernible at the Si^{4+} region (Fig. 1(d)).

In Fig. 2, we present oxygen exposure dependence of the Si 2p state on titanium-covered Si(001) at RT. There are almost no components of Si^{+} state and Si^{2+} state even at low oxygen coverage. This is a marked difference from oxidation on a clean Si(001) surface. We consider

that number of stable adsorption sites for oxygen largely increases at the interface of Ti/Si(001).

There are two main features of the present results obtained at RT. The estimated thickness of the oxide layer is large at about 0.9 nm. Quite small amounts of suboxide components are observed, indicating the formation of high-quality SiO_2 below the TiO_x film. Here, we assume that the titanium atoms do not migrate into the silicon substrate or SiO_2 layer during oxidation at RT, though intermixing of titanium atom with Si dimer is known to occur at high temperature above 440 K [10]. The estimated oxide thickness of about 0.9 nm suggests that oxidation should occur at the subsurface adsorption sites even at RT.

Effect of thermal treatment was also investigated. An energy shift to 3.52 eV occurs during annealing to 570 K. The peak position for the oxidized Si 2p state increases to 4.43 eV with consecutive heating up to 970 K. Formation of titanium silicate ($TiSi_xO_y$) was confirmed by changes of Ti 2p and O 1s states at high temperatures.

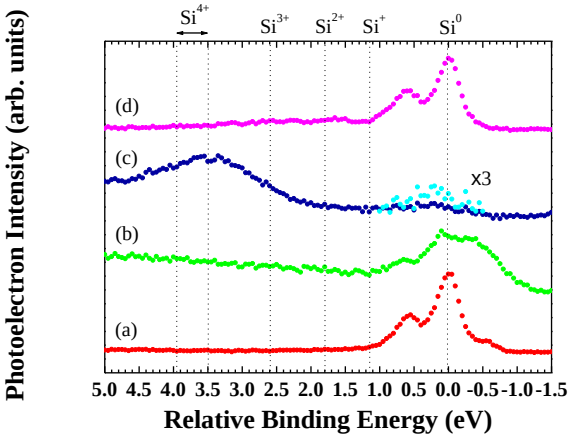

Fig. 1 A series of Si 2p PES spectra obtained at RT for (a) a clean Si(001) surface, (b) titanium-deposited surface at the coverage of 0.3-0.4 nm, (c) followed by an oxygen exposure of 60 L, and (d) the oxidized Si(001) surface at 750 L.

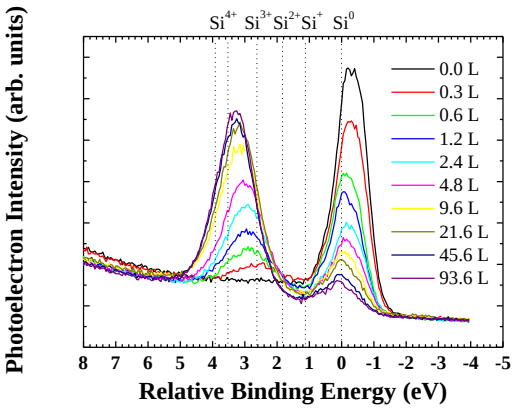

Fig. 2 Oxygen exposure dependence of the Si 2p spectra on a titanium-covered Si(001) surface.

References

[1] G.D. Wilk *et al.*, J. Appl. Phys. 89, 5243 (2001).
[2] M.V. Fischetti *et al.*, J. Appl. Phys. 90, 4587 (2001).
[3] S. Barraud *et al.*, J. Appl. Phys. 104, 073725 (2008).
[4] S. Sayan *et al.*, Appl. Phys. Lett. 80, 2135 (2002).
[5] Y. Teraoka, *et al.*, Jpn. J. Appl. Phys. 41, 4253 (2002).
[6] J. Xu *et al.*, J. Appl. Phys. 82, 6289 (1997).
[7] P. Soukiassian *et al.*, Phys. Rev. B 35, 4176 (1987).
[8] M. Toramaru *et al.*, J. Phys.:Condens. Matter 20, 485006 (2008).
[9] A. Arranz *et al.*, Surf. Sci. 588, 92 (2005).
[10] K. Ishiyama *et al.*, Phys. Rev. B 51, 2380 (1995).

Rashba spin splitting of a metallic surface state band of Pb/Ge(111)-(√3×√3)*R*30°

Koichiro YAJI[*1,2], Shinichiro HATTA[1,2], Yoshiyuki OHTSUBO[1,2], Ayumi HARASAWA[3], and Tetsuya ARUGA[1,2]
[1]*Graduate School of Science, Kyoto University, Kyoto, 606-8502, Japan.*
[2]*JST CREST, Saitama 332-0012, Japan.*
[3]*Institute for Solid State Physics, University of Tokyo, Kashiwashi, Chiba 277-8581, Japan.*

Introduction

Spin-orbit interaction (SOI) is believed to play a decisive role in coming spintronic devices that do not need ferromagnets or external magnetic field and hence are highly compatible with the existing semiconductor-based electronics. Among the phenomena related to SOI, the Rashba effect [1,2] refers to the spin splitting of two-dimensional electronic states induced by the structural inversion asymmetry at, for instance, semiconductor heterojunctions. Discovery of the giant Rashba effect at crystal surfaces such as Au [3,4], Bi [5], and Bi-covered Ag [6,7], where spin splitting is orders of magnitude larger than those in semiconductor heterojunctions, has been attracting significant interests because of a possibility of new physics related with surface spin transport/accumulation. Most of the known surface Rashba systems are based on the metal and semimetal substrates. We remark that, in order to study surface spin transport or to find spintronic applications, it is crucial to establish a metallic surface-state band that is spin-split by the Rashba effect on a semiconductor surface. Recently, the Rashba spin-split bands on semiconductor surfaces have been identified on Si(111) and Ge(111) surfaces [8-10]. However, there are no metallic surface state bands for these surfaces and hence cannot contribute to the transport of spins. In the present study, we report an electronic states for a monolayer Pb-adsorbed Ge(111) (Pb/Ge(111)-β) surface measured by angle-resolved photoelectron spectroscopy (ARPES). We have found a metallic surface-state band with a free-electron-like dispersion, which exhibits the Rashba spin splitting.

Experiment

The ARPES was performed at KEK-PF BL18A. The photon energy was set to 30 eV. A Ge(111) substrate was prepared by several cycles of 1.0 keV Ar^+ bombardment and subsequent annealing up to 870 K for a few seconds. Orderliness and cleanliness of the surface were checked by a sharp c(2×8) low-energy electron diffraction (LEED) pattern. Pb was deposited onto the surface at room temperature, which was then annealed at 570 K for five minutes to prepare a well-ordered wide terrace of Pb/Ge(111)-β. Here, the structural model and LEED pattern of the Pb/Ge(111)-β surface are shown in Fig. 1(a) and (b), respectively.

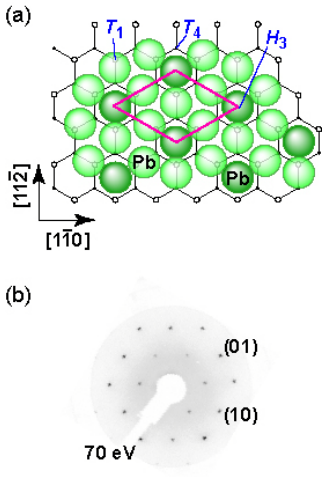

Fig. 1 (a) Top view of Pb/Ge(111)-β. The large and small circles indicate Pb adatoms and Ge atoms in the first bilayer, respectively. The solid parallelogram denotes the unit cell. (b) LEED pattern of Pb/Ge(111)-β.

Results and discussion

Figure 2(a) displays the angle-resolved photoelectron spectra taken along the $M_1\Gamma_1M_1$ direction of (√3×√3)*R*30° surface Brillouin zone and a

binding energy versus in-plane momentum (band dispersion) image is shown in Fig. 2(b). Three Pb-induced bands named S_1, S_2 and S_3 are observed. These bands are not observed on the clean Ge(111)-c(2×8) surface. The S_1 band is located in the projected bulk band gap and crosses the Fermi level. The S_2 and S_3 bands are surface resonance states because the states appear in the projection of bulk bands. The S_1-S_3 bands are also observed in the ARPES data taken with $h\nu$ = 21.2, 40.8 eV. This supports the assignment of the S_1-S_3 bands to the surface states. The overall dispersion of S_1, S_2 and S_3 suggests that a *free-electron-like* parabolic band is hybridized with a nearly flat band at 0.9 eV (S_2), yielding upper (S_1) and lower (S_3) branches. From the high resolution ARPES [11], the energy splitting value between the spin-up and spin-down states for the *S*1 band was estimated to be 200 meV at the Fermi wave number k_F = 0.36 Å^{-1} . In addition, we have characterized that the S_1 band splits into two due to the surface Rashba effect by means of spin-resolved photoelectron spectroscopy [11]. A first-principles calculation suggests that the S_1 and S_3 bands are predominantly of Pb 6$p_{x,y}$ character. On the other hand, the S_2 band has a character of bonding orbital between Pb 6p_z and Ge 4p_z of the topmost Ge atoms. We conclude that the Rashba spin splitting is realized for a metallic surface-state band on a semiconductor surface, thus serving as a basis for surface spin transport.

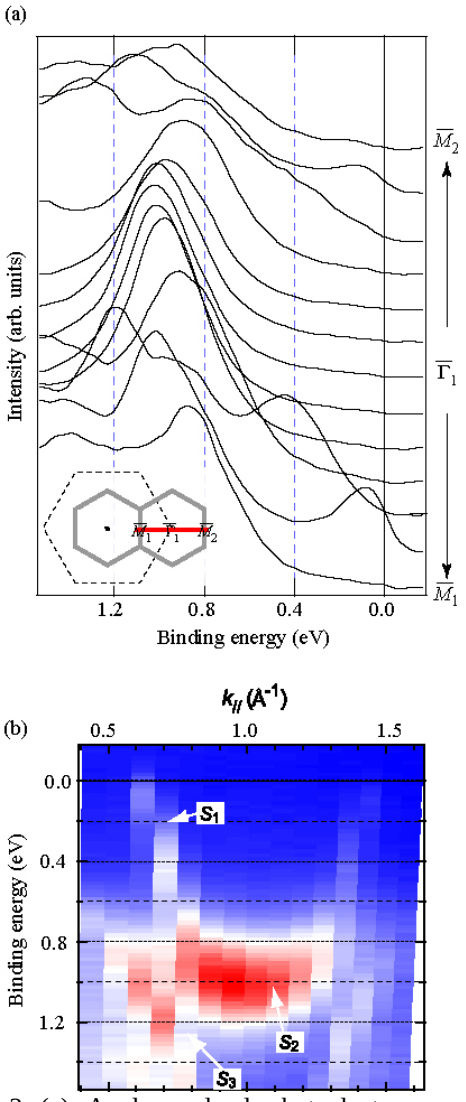

Fig. 2 (a) Angle-resolved photoelectron spectra taken along $M_1\Gamma_1M_2$ of the ($\sqrt{3}\times\sqrt{3}$)*R*30° surface Brillouin zone as shown in the inset. (b) Energy band dispersion.

References

[1] E. I. Rashba, Sov. Phys.: Solid State **2**, 1109 (1960).
[2] Y. A. Bychkov and E. I. Rashba, JETP Lett. **39**, 78 (1984).
[3] S. Lashell, B. A. McDougall, and E. Jensen, Phys. Rev. Lett. **77**, 3419 (1996).
[4] M. Hoesch *et al.*, Phys. Rev. B **69**, 241401(R) (2004).
[5] Yu.M. Koroteev *et al.*, Phys. Rev. Lett. **93**, 046403 (2004).
[6] C. R. Ast *et al.*, Phys. Rev. Lett. **98**, 186807 (2007).
[7] F. Meier *et al.*, Phys. Rev. B **77**, 165431 (2008).
[8] I. Gierz *et al.*, Phys. Rev. Lett. **103**, 046803 (2009).
[9] S. Hatta *et al.*, Phys. Rev. B **80**, 113309 (2009).
[10] K. Sakamoto *et al.*, Phys. Rev. Lett. **103**, 156801 (2009).
[11] K. Yaji *et al.*, Nat. *Commun.* 1:17 doi: 10.1038 / ncomms1016 (2010).

Spin and Angle-resolved Photoelectron Spectroscopy on Si(557)-Au surface

[1]Taichi Okuda[*], [1]Koji Miyamoto, [2]Yasuo Takeichi, [3]Hirokazu Miyahara, [2]Manami Ogawa, [3]Akio Kimura, [2]Ayumi Harasawa, [2]Akito Kakizaki, [4]Tatsuya Shishidou and [4]Tamio Oguchi

[1]Hiroshima Synchrotron Radiation Center, Hiroshima University*

[2]Institute for Solid State Physics, The University of Tokyo

[3]Graduate School of Science, Hiroshima University

[4]ADSM&IAMR, Hiroshima University

Rashba effect in which spin-splitting surface states are arisen by strong spin-orbit interaction with spatial symmetry breaking is one of the intriguing phenomena on two-dimensional system such as surface or interface and has been investigated extensively these days. The Rashba effect in one-dimensional system, however, has not been demonstrated so far. Au induced one-dimensional atomic chain structure on Si(557) surface is one of the optimum candidates to investigate the Rashba effect in one-dimensional system. In fact, the electronic structure of the Si(557)-Au observed by high-resolution angle-resolved photoelectron spectroscopy (ARPES) shows nice metallic surface states which indicate strong one-dimensionality having straight Fermi lines[1]. Further, interesting double bands were observed in the surface states by detailed ARPES measurement[2]. The origin of the double bands is, however, still unknown. Ahn *et al.* attributed the double surface states to the different one-dimensional surface structures on the Si(557)-Au surface[3]. On the other hand, Sánchez-Portal and co-workers suggested that the strong spin-orbit interaction of Au causes the spin-splitting on the surface states, *i.e.* Rashba spin-splitting[4]. Although some indirect evidences of the spin-splitting by the Rashba effect for the surface states have been reported by some experiments[5][6] the direct observation of the spin structure of the surface states can only settle the issue and spin-resolved photoelectron spectroscopy was strongly. In this report we show the results of the direct observation of the spin-structure of the surface states by means of high-resolution "spin-" ARPES measurement for the first time.

Spin-resolved ARPES measurement has been done at BL-19A of Photon Factory, KEK with using homemade high-yield spin-detector[7] combined with the high energy-resolution photoelectron analyzer (PHOIBOS-150, SPECS GmbH). "Spin-unresolved" ARPES measurement has been also done at BL-18A in advance. One dimensional Au atomic chain structure was prepared on Si(557) surface by depositing 0.2 ML Au atoms on the clean surface at 650 °C.

Fig.1 shows the "spin-unresolved" ARPES result of the Si(557)-Au surface taken at hν=34 eV. The metallic surface states of one-dimensional atomic Au having double parabola are clearly observed as reported in literatures[2]. The strong intensity asymmetry between two branches of double surface states is due to the photoemission matrix element effect.

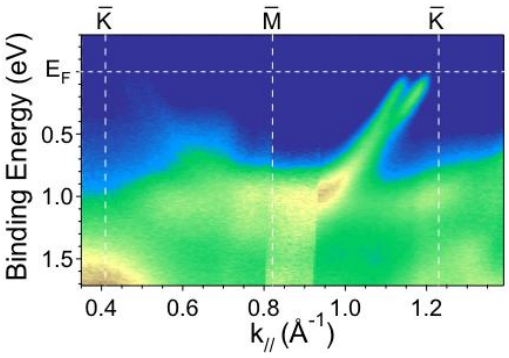

Fig.1 Band structure of the surface states of Si(557)-Au obtained by "spin-unresolved" ARPES measurement.

The spin resolved ARPES spectra are shown in Fig.2(a) taken at the same photon energy as the

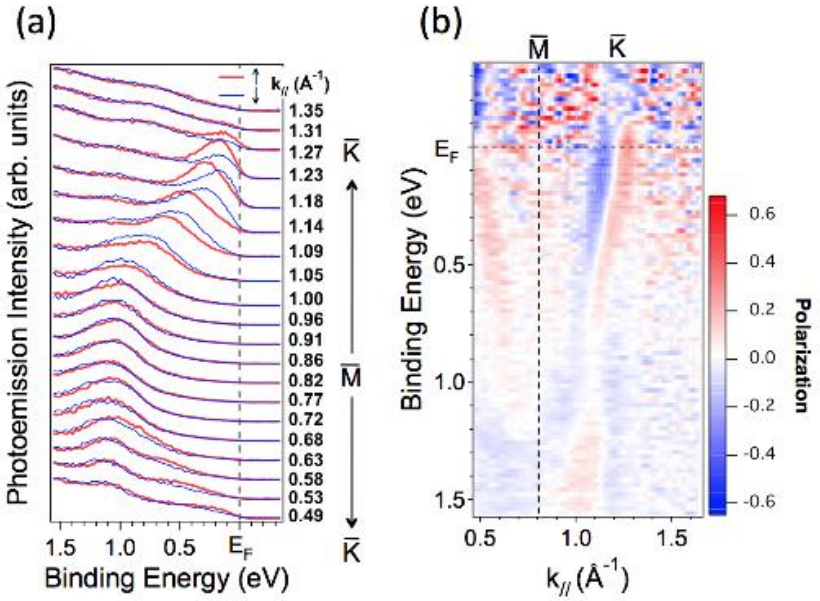

Fig.2 (a) Spin-resolved ARPES spectra of the surface states. Red and blue curves correspond to up- and down-spin states, respectively. (b) The spin-polarization map obtained by (a). The spin-polarization reversal against M bar point is seen.

"spin-integrated" measurement. In the figure red and blue curves indicate up- and down-spin states, respectively. As in the figure, the peak positions of up- and down spin states shift each other and at $k_{//}$ >1.00 Å^{-1} down-spin state is shifted to lower binding energies than that of up-spin state. On the contrary, at $k_{//}$ <0.68 Å^{-1} the shift is opposite and up-spin state is shifted to lower binding energies. This spin-polarization reversal against M bar point is more clearly seen in the spin-polarization map in Fig. 2(b) where the spin polarization of one branch of the surface state indicated by color scale changes from positive to negative at the M bar point. The spin-splitting of the surface states and the spin-polarization reversal against the time-reversal invariant point (=M bar) are the criteria of the Rashba effect and the results clearly indicate that the origin of the double surface states is the Rashba effect. This is the first observation of the Rashba effect in one-dimensional surface states.

References

[1] J. N. Crain, J. L. McChesney, Fan Zheng, M. C. Gallagher, P.C. Snijders, M. Bissen, C. Gundelach, S. C. Erwin and F. J. Himpsel, Phys. Rev. B **69**, 125401 (2004) and references therein.

[2] R. Losio, K. N. Altmann, A. Kirakosian, J.-L. Lin, D. Y. Petrovykh, and F. J. Himpsel, Phys. Rev. Lett. **86**, 4632 (2001).

[3] J. R. Ahn, H. W. Yeom, H. S. Yoon, and I. –W. Lyo, Phys. Rev. Lett. 91, 196403 (2003).

[4] D. Sánchez-Portal, S. Riikonen, and R. M. Martin, Phys. Rev. Lett. 93, 146803 (2004).

[5] I. Barke, F. Zheng, T. K. Rugheimer and F. J. Himpsel, Phys. Rev. Lett. 97, 226405 (2006).

[6] T. Nagao, S. Yaginuma, T. Inaoka, and T. Sakurai, Phys. Rev. lett. 97, 116802 (2006).

[7] T. Okuda, Y. Takeichi, Y. Maeda, A. Harasawa, I. Matsuda, T. Kinoshita, and A. Kakizaki, Rev. Sci. Instrum. 79, 123117 (2008), T. Okuda, Y. Takeichi, A. Harasawa, I. Matsuda, T. Kinoshita, and A. Kakizaki., Eur. Phys. J. Special Topics 169, 181 (2009).

Spin-resolved photoemission study on Dirac-like surface states of ultrathin Bi_2Se_3 films

Yusuke Sakamoto[1], Toru Hirahara[1], Yasuo Takeichi[2], Iwao Matsuda[2], Akito Kakizaki[2], Shuji Hasegewa[1]

[1] *Department of Physics, Graduate School of Science, The University of Tokyo*

[2] *Synchrotron Radiation Laboratory, The Institute for Solid State Physics, The University of Tokyo*

Introduction

Recently there has been growing interest in *topological insulators* (3D) or the *quantum spin Hall (QSH) phase* (2D), which are insulating materials with bulk band gaps but have metallic edge states that are formed topologically and robust against any non-magnetic impurity [1]. In a three-dimensional material, the two-dimensional surface states correspond to the edge states (topological metal). Due to the loss of the inversion symmetry, they have spin-filtered properties which are actually the origin of the topological robustness. Since the surface states of Bi_2Se_3 with Dirac-like linear band dispersion have a very small Fermi wave number, it has been difficult to actually observe the spin-split properties. Therefore in the present study, we have conducted high-resolution spin- and angle- resolved photoemission (SARPES) studies on ultrathin Bi_2Se_3 films to directly verify their spin polarization.

Experiment

The experiments were performed at BL-19A of Photon Factory-KEK. The system has a hemispherical analyzer (SPECS Phoibos-150) equipped with a homemade high-yield spin-polarimeter using spin-dependent very-low-energy electron diffraction (VLEED) [1]. A He lamp (He Iα =21.2 eV) was used as the excitation source and the SARPES spectra were recorded at 150 K with the energy and angle resolutions of 30 meV and 0.7°, respectively. The effective Sherman function in this experiment was 0.3 as calibrated by the spin-polarized secondary electrons from a standard Ni sample.

The ultrathin Bi_2Se_3 films were fabricated *in situ* in a method similar to the report of Ref. [2]. First, a clean Si(111)-7$\times$7 surface was prepared on an *n*-type substrate (P-doped, 1-10 Ωcm at room temperature) by a cycle of resistive heat treatments. The Si(111)β $\sqrt{3}\times\sqrt{3}$-Bi surface was formed by 1~ML (7.83×10^{14} cm^{-2}) of Bi deposition on the 7$\times$7 surface at 620 K monitored by Reflection High Energy Electron Diffraction. Then Bi was deposited on the β $\sqrt{3}\times\sqrt{3}$-Bi structure at ~400 K in a Se-rich condition. Such a procedure is reported to result in a smooth epitaxial film formation with the stoichiometric ratio of Bi:Se=2:3 [2]. It is also known that the minimum film thickness that can be achieved in this method is one quintuple layer (1 QL = 10 Å), and the films can be formed QL-by-QL. We have carefully checked the film thickness by monitoring the spot intensity of the RHEED pattern [3] and the film thickness in the present measurements was 8 QL (80Å).

Results and discussions

Figures 1(a) and (c) show the SARPES spectra ($I_\uparrow$, $I_\downarrow$) near the Γ point along the Γ-M direction (x direction) for negative (a) and positive (c) emission angles, respectively, and Figs. 1(b) and (d) show the corresponding spin-polarization curves $P=(I_\uparrow - I_\downarrow)/(I_\uparrow + I_\downarrow)$. The spin orientation is in the +y (red curves) [-y (blue curves)] direction. The photoemission intensity for the bulk states is much stronger than that of the surface states and it is really

difficult to resolve the two in the energy distribution curves of Figs. 1(a) and (c). However, if we look carefully at $I_{\uparrow}$ and $I_{\downarrow}$ we notice that $I_{\uparrow} < I_{\downarrow}$ for negative angles, $I_{\uparrow} = I_{\downarrow}$ just near normal emission, and $I_{\uparrow} > I_{\downarrow}$ for positive angles near the Fermi level. This can also be noticed by the hatched areas in the spin-polarization curves of Figs. 1(b) and (d). The spin-polarized states seem to disperse toward E_F as they pull off from normal emission. We believe that this is representing the helical nature of the spin-split surface states. The obtained spin-polarization values are ~10 % at maximum, which is very small probably due to the bulk state close by. Another effect may come from a technical problem concerning the He I β and/or He II radiation enhancing the background of the spectra.

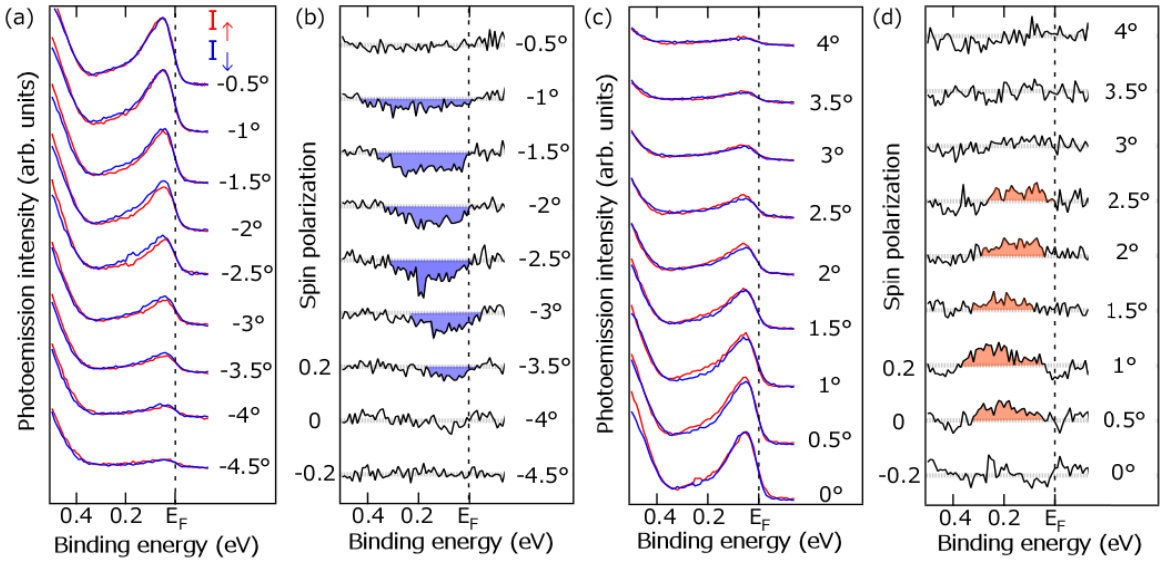

Figure 1: Spin-resolved ARPES spectra of an 8~QL ultrathin Bi_2Se_3 film along the Γ-M direction (x direction) [(a) and (c)] and the spin polarization curves deduced from them [(b) and (d)]. The spin orientation is along the Γ-M direction (y direction, red (blue) is for +y (-y) direction).

References

[1] T. Okuda, Y. Takeichi, Y. Maeda, A. Harasawa, I. Matsuda, T. Kinoshita, and A. Kakizaki, Rev. Sci. Instrum. **79**, 123117 (2008).

[2] G. Zhang, H. Qin, J. Teng, J. Guo, X. Dai, Z. Fang, and K. Wu, Appl. Phys. Lett. **95**, 053114 (2009).

[3] Y. Sakamoto, T. Hirahara, H. Miyazaki, S. Kimura, and S. Hasegawa, Phys. Rev. B **81**, 165432 (2010).

Electronic structure of $BaPrO_3$-based oxides studied with soft X-ray absorption and emission spectroscopy

Shu Yamaguchi [1], Tohru Higuchi [2], Yukiko Oyama [1],

Shogo Miyoshi [1], Shin Mimuro [1], Takeo Kikuchi [1]

1 *Department of Materials Engineering, The University of Tokyo*

2 *Department of Applied Physics, Tokyo University of Science*

Introduction

Solid Oxide Fuel Cells (SOFCs) employing proton-conducting oxides as electrolyte is expected to realize low-temperature operation compared with the ones based on oxide-ion conducting electrolytes. While numerous studies have been devoted to proton-conducting oxides as the electrolytes, there have been fewer reports on the cathode materials for proton-conducting SOFCs (PC-SOFCs). It is considered that protonic and electronic mixed conductivity is an important property for high cathode performance.

In our previous studies, the electrochemical properties of $BaPr_{1-x}Yb_xO_3$ have been investigated in expectation of proton-hole mixed conduction [1]. To the contrary, it was found that its proton solubility is rather small, implying poor protonic conduction in the material. On the other hand, the oxide shows predominant hole conductivity, which increases almost linearly with the dopant concentration, but the conductivity itself is very low. While the observed conduction behaviour appears to follow a classic defect-chemical scheme and rigid-band model, we have recently found anomalous electronic structures via X-ray spectroscopy [2]. It has been inferred that both of the unoccupied state which corresponds to a non-bonding O2*p* level doped with hole (O^-) and the occupied state which corresponds to Pr^{3+} simultaneously decreases in intensity upon doping with Yb. Therefore, it is considered that the two defect species O^- and Pr^{3+} generate together via an auto-ionization reaction: $Pr^{4+} + O^{2-} \rightarrow Pr^{3+} + O^-$. In order to further understand the overall picture of the electric transport property as well as electronic structure in the $BaPrO_3$-based system, it is necessary to extend the investigation to the donor-doped compositions.

In this report, we present the results of soft X-ray spectroscopy on $Ba_{0.95}La_{0.05}PrO_3$, in which La^{3+} should act as a donor. Additionally, the effect of heat-treatment, which controls the oxidation state and carrier concentration, will be reported.

Experimental

The powders of $Ba_{0.95}La_{0.05}PrO_3$, $BaPrO_3$, and $BaPr_{0.7}Yb_{0.3}O_3$ have been prepared via a citric acid method, and then sintered at 1673K. Some samples have been equilibrated at 1073 K in dry O_2, wet O_2 or dry Ar atmosphere. Soft X-ray absorption spectra have been collected by a total fluorescence method at BL-19B of Photon Factory, KEK.

Results and discussion

Figure 1 shows the O1*s*-2*p* and Pr3*d*-4*f* X-ray Absorption (XAS) spectra of $BaPrO_3$ (BP), $Ba_{0.95}La_{0.05}PrO_3$ (BLP5), and $BaPr_{0.7}Yb_{0.3}O_3$ (BPY30), which reflect respective partial

unoccupied density of state. In the O1*s*-2*p* XAS (Fig. 1 (a)), as has been observed for $BaPr_{1-x}Yb_xO_3$, a pre-edge peak (A) has been observed at 534 eV, which has been attributed to an unoccupied non-bonding O2*p* level, O^-. The peak (A) of BPY is smaller in intensity than that of BP, which corresponds to the decrease in the hole concentration by the auto-ionization. Another important observation is that in the case of BPY30, a shoulder (B) is observed at the low energy side of the peak (A). Since the hole conductivity of $BaPr_{1-x}Yb_xO_3$ increases with *x* [1], it is deduced that the unoccupied state (B) corresponds to the electron holes introduced by Yb^{3+}-doping. Thus the two hole states originating from auto-ionization and chemical doping of Yb have been distinguished. On the other hand, no significant difference can be found between the O1*s*-2*p* XAS spectra of BP and BLP5, indicating that the carriers introduced by La-doping are electrons. The Pr3*d*-4*f* XAS spectra (Fig. 1(b)) shows almost no difference between the compositions, indicating that the charge compensation for acceptor(Yb)-doping is mostly taken by contributed to by oxygen rather than praseodymium.

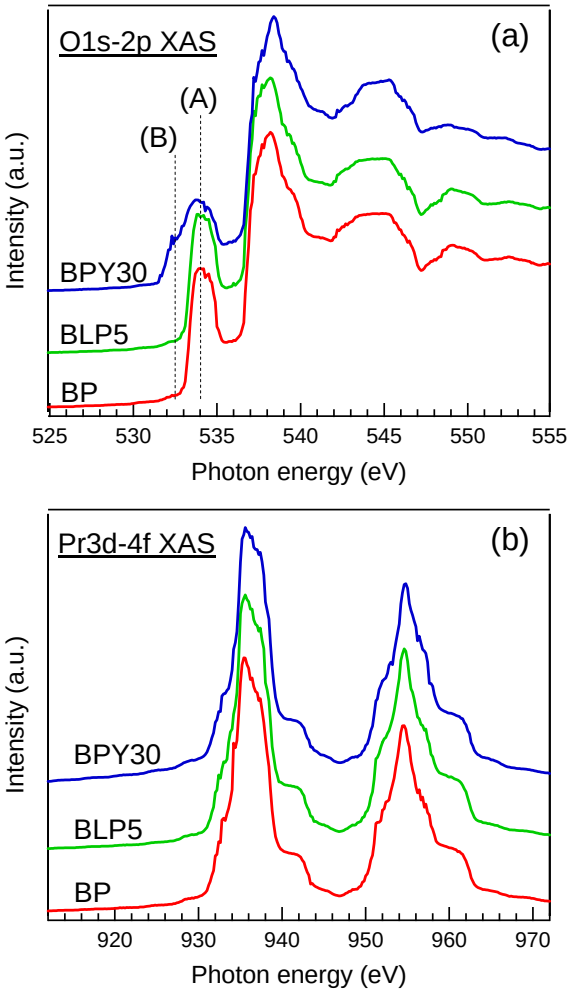

Fig. 1: O1*s*-2*p* (a) and Pr3*d*-4*f* (b) XAS spectra of BP, BPY30 and BLP5.

Figure 2 shows the effect of heat-treatment on the O1*s*-2*p* XAS spectra of BPY30. The sample heat-treated in O_2 atmosphere shows the peak (B) being prominent. On the other hand, the peak (B) is almost absent after reduction in Ar atmosphere. This agrees with the observation that the conductivity decreases upon reduction, which accompanies the formation of oxide ion vacancy. This again confirms that the peak (B) originates from the hole state introduced by Yb-doping, which contributes to the electric conduction. The decrease in the intensity of peak (B) of the sample treated in wet O_2 suggests any interaction with water vapor, probably dissolution of protons into the oxide.

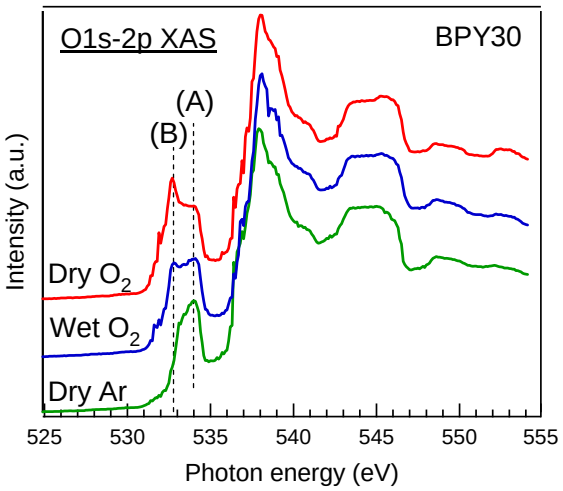

Fig. 2: O1*s*-2*p* XAS spectra of BPY30 heat-treated in dry O_2, wet O_2 and dry Ar at 1073 K.

Reference

[1] S. Mimuro et al., Solid State Ionics 178, 641 (2007).
[2] S. Yamaguchi et al., Activity Report of Synchrotron Radiation Laboratory 2008.

Characterizations of Core Level Electronic Structure and Interaction of Ln-M Cyano DMF Complex by Soft-X-ray Spectroscopy (in 2009)

Takashiro Akitsu*

*Department of Chemistry, Faculty of Science, Tokyo University of Science

During searching for new functional materials acting as photo-controllable molecule-based magnets [1-10], we discovered $Nd(DMF)_4(H_2O)_3Fe(CN)_6 \cdot H_2O$ complex as the first material among 3d-4f cyano-bridged complexes [1]. In order to discuss the role of crystal lattice (intermolecular hydrogen bonds) and coordination environment (3d electronic states coupled with 4f ions) separately, we carried out the measurements of soft X-ray absorption spectra (XAS) under variable temperature conditions by comparing X-ray crystal structure analysis. In this year, we have examined various Ln(III) ions in isostructural $Ln(DMF)_4(H_2O)_3Fe(CN)_6 \cdot H_2O$ complexes (Figure 1) and H/D isotope effects for some compounds.

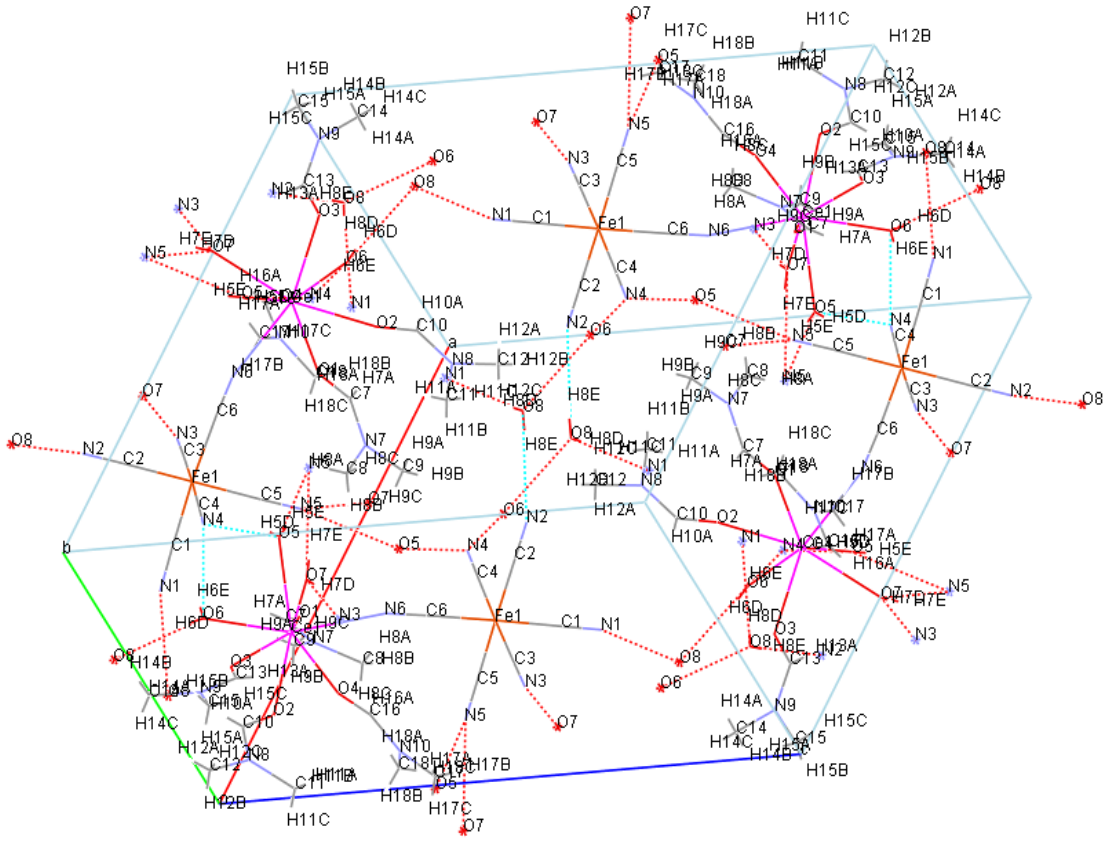

Figure 1. Crystal structure of $Ln(DMF)_4(H_2O)_3Fe(CN)_6 \cdot H_2O$

$Ln(DMF)_4(H_2O)_3Fe(CN)_6 \cdot H_2O$ complexes substituted by Ce(III), Sm(III), Gd(III), and Er(III) ions (abbreviated as **CeFe**, **SmFe**, **GdFe**, and **ErFe**) and some H/D isotope complexes (abbreviated as **HH**, **DH**, **HD**, and **DD**) were prepared by using the corresponding D_2O and DMF-d1 solvents according to the literature [1]. The $Fe2p_{3/2}$ and $2p_{1/2}$ XAS were measured at KEK PF BL-19B under variable temperature. The spectra were corrected by the standard Au sample.

The $\chi_M T$ vs T plots at various temperature exhibited H/D isotope effects due to intermolecular hydrogen bonds. However, The $Fe2p_{3/2}$ and $2p_{1/2}$ XAS and ^{57}Fe Mössbauer

spectra indicated that low-spin Fe(III) states were kept for all the conditions. For example, the $Fe2p_{3/2}$ and $2p_{1/2}$ XAS for **CeFeHH** at 298 and 70 K are depicted in Figure 2. The $Fe2p_{3/2}$ and $2p_{1/2}$ XAS spectral information is ascribed to temperature dependence of local coordination environment around Fe ions as well as electronic states. For all compounds measured, low-spin Fe(III) state is also conserved for **DH**, as is **HH**, and little H/D isotope effect can be observed by means of XAS.

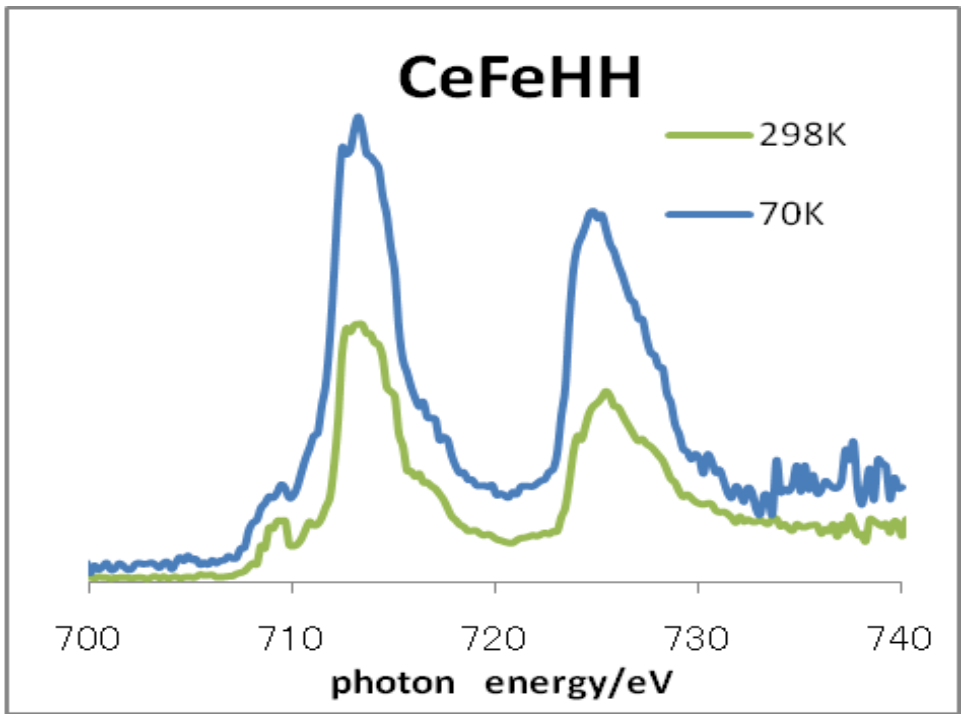

Figure 2. Crystal structure of $Ln(DMF)_4(H_2O)_3Fe(CN)_6 \cdot H_2O$

In this way, we have investigated H/D isotope effects of $Ln(DMF)_4(H_2O)_3Fe(CN)_6 \cdot H_2O$ and their thermal-responses. Although the $\chi_M T$ vs T plot exhibits H/D isotope effect against intermolecular hydrogen bonds, this influence cannot change low-spin Fe(III) electronic state. Conservation of low-spin Fe(III) electronic state is also supported $Fe2p_{3/2}$ and $2p_{1/2}$ XAS about local information of Fe atoms. Comparison with other systems of local distortion of coordination environment and global strain of crystal lattice may help to understand characteristics of the present results. However, crystallographic study involving other systems is in progress now.

References

[1]G. Li, T. Akitsu, O. Sato, Y. Einaga, *J. Am. Chem. Soc*., **125,** 12396 (2003).
[2] G. Li, O. Sato, T. Akitsu, Y. Einaga, *J. Solid State Chem*., **177**, 3835 (2004).
[3] G. Li, T. Akitsu, O. Sato, and Y. Einaga, *Hyperfine Interactions*, **156/157**, 143 (2004).
[4] T. Akitsu, Y. Einaga, *Polyhedron*, **25**, 2655 (2006).
[5] T. Akitsu, Y. Einaga, *Inorg. Chim. Acta*, **359**, 1421 (2006).
[6] T. Akitsu, Y. Einaga, *Asian Chemistry Letters*, **10**, 95 (2006).
[7] T. Akitsu, Y. Einaga, *Asian Chemistry Letters*, **10**, 113-120 (2006).
[8] T. Akitsu, Y. Einaga, *Asian Chemistry Letters*, **10**, 121 (2006).
[9] T. Akitsu, Y. Einaga, *Chemical Papers*, **61**, 194-198 (2007).
[10] T. Akitsu, J. Nishijo, *J. Magn. Magn. Mater.*, **320**, 1586 (2008).

A Study on the Electronic Structure of Proton Conducting $A^{III}B^{III}O_3$ Single Crystal

H. Yugami*, Y. Nagao*, J. Liu*, T. Higuchi**, F. Iguchi*, N. Sata*

*Department of Mechanical Systems and Design, Graduate School of Engineering, Tohoku University

** Department of Applied Phisycs, Faculty of Science, Tokyo University of Science

Introduction

Since it was reported in the early 1980s that some acceptor-doped ABO_3 perovskite-type oxides such as $A^{II}B^{IV}O_3$ ($SrCeO_3$, $BaCeO_3$ and others) show high proton conductivity in a humid atmosphere at high temperatures, studies of high-temperature proton conductors have become more intensive because of their potential applications in fuel cells or hydrogen sensors. Recently some acceptor-doped $A^{III}B^{III}O_3$ perovskite-type oxides have also been reported to show high proton conductivity in the presence of H_2O vapor or hydrogen at high temperatures. Among them, the $La_{0.8}Sr_{0.2}ScO_3$ ceramic shows the highest proton conductivity, comparable to that of $BaCe_{0.95}Y_{0.05}O_3$. These results suggest that Sr-doped $LaScO_3$ oxides are promising proton conductors. However, their proton conducting mechanism has not yet been fully studied and their fundamental physical and chemical properties need clarification.

In our previous study, we fabricated single crystals of Sr-doped $LaScO_3$ and examined proton existence and proton conduction in them by infrared (IR) absorption and electrical conductivity measurements. To further investigate the proton conduction mechanism of these single crystals, understanding the electronic structure is vital for further applications, because the electronic structure around the band gap region is strongly related to the conduction of electrons, holes or ions. In this study, the electronic structure near the bottom of the conduction band and the top of the valence band for $La_{1-x}Sr_xScO_3$ single crystal ($x = 0.03$; denoted by LSS3) annealed under dry or wet atmosphere at 800 ^oC has been investigated by X-ray absorption spectroscopy (XAS).

Experimental

A transparent LSS3 crystal was grown by the floating zone method in a Xe arc imaging furnace. XAS spectra were measured using a soft-X-ray spectrometer installed at the undulator beamline BL-19B of the Photon Factory at the High Energy Accelerator Organization. The photon energy was calibrated by measuring the photoemission spectrum of the 4*f* core level of an Au film. The single crystal was cut into a plate shape with a thickness of about 0.5 mm, and the surface was optically polished. XAS spectra of the specimen under three different conditions were measured sequentially in the following order. Dry N_2 annealing was performed through annealing at 800 ^oC for 20 h in N_2 atmosphere. After XAS measurements of dry-N_2-annealed LSS3, the sample was annealed at 800 ^oC for 10 h in wet air ($Ar:O_2 = 4:1$, $P_{H2O} = 3$ kPa). Finally, after measuring the XAS spectrum of wet-annealed LSS3, the sample was annealed at 800 ^oC for 20 h in Ar atmosphere to check the dry annealing condition.

Results and discussion

Figure 1 shows the O 1s XAS spectra of the LSS3 single crystal annealed at 800 ^oC in the different atmospheres. The absorption intensity was normalized by the absorption intensity at 536 eV. On the basis of the dipole selection rule, it can be understood that the O 1s XAS

spectrum for ScO_6-octahedral structures corresponds to transitions from the O 1s state to the O 2p state hybridized with the unoccupied Sc 3d states. An obvious absorption feature appears at ~531 eV for LSS3 below the Sc 3d absorption edge, which is not observed for an undoped $LaScO_3$ single crystal. The feature is considered to be due to oxygen vacancies induced by Sr doping.

The XAS spectrum of wet-annealed LSS3 shows a broad absorption around the top of the valence band. A decrease in the intensity of absorption at 532 eV compared with that observed in dry-annealed LSS3, which is due to the t_{2g}-subband of the unoccupied Sc 3d state hybridized with the O 2p state, may be due to the change in DOS on the top of the valence band composed of O 2p.

After the XAS spectrum measurement of wet-annealed LSS3, the sample was annealed at 800 ^{o}C for 20 h in Ar atmosphere to confirm the change in electronic structure by dry annealing. The XAS spectrum is the same as that of the first dry-N_2-annealed LSS3 single crystal. The broad absorption at approximately 526 eV vanishes again after dry Ar annealing. The intensity of the broad absorption at approximately 526 eV in the XAS spectrum of wet-annealed LSS3 is considerably large and the change in absorption intensity is significant considering the signal-to-noise ratio of the spectra. The broad absorption at approximately 526 eV in the XAS spectrum for wet-annealed LSS3 may be related to the level of holes generated under moist atmospheres.

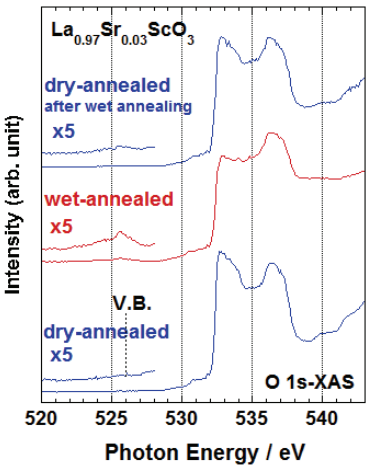

Figure 1 O 1s XAS spectra of LSS3 single crystal measured at room temperature after annealing at 800 ^{o}C in different atmospheres. The vertical dashed line indicates the top of the valence band (V.B.).

Conclusion

The electronic structure near the bottom of the conduction band and the top of the valence band for LSS3 annealed in different atmospheres has been investigated by XAS measurements. A defect-induced localized level is observed below the Sc 3d state for a Sr-doped single crystal, which is considered to be due to the presence of an oxygen vacancy around an acceptor ion of Sr. The XAS spectrum of wet-annealed LSS3 shows a broad absorption around the top of the valence band. The intensity of absorption at 532 eV, which was due to the t_{2g}-subband of the unoccupied Sc 3d state hybridized with the O 2p state, decreased compared with that of absorption in dry-annealed LSS3 because the DOS on top of the valence band composed of O 2p had changed. The broad absorption at approximately 526 eV in the XAS spectrum for wet-annealed LSS3 may be related to the level of holes generated under moist atmospheres.

Acknowledgment

This work has been partially supported by a Grant-in-Aid for Scientific Research on Priority Area Nanoionics (439) and by the Program for Improvement of Research Environment for Young Researchers from Special Coordination Funds (SCF) for Promoting Science and Technology commissioned by the Ministry of Education, Culture, Sports, Science and Technology (MEXT) of Japan.

Resonant Soft-X-ray Emission Study of $La_{0.6}Sr_{0.4}FeO_3$ Thin Film

Tohru Higuchi[1], Masashi Matsumoto[1] and Jinghua Guo[2]
[1]*Department of Applied Physics,Tokyo University of Science*
[2]*Advance Light Source, Lawrence Berkeley National Laboratory*

$LaFeO_3$ is an antiferromagnetic insulator with a high Neel temperature (T_N) of approximately 750 K. The substitution ($La_{1-x}Sr_xFeO_3$) of La^{3+} with Sr^{2+} produces a formal change in the valence state of Fe ion from 3+ (x=0) to 4+ (x=1). This leads to the decrease of T_N and the increase of electronic conductivity. In particular, $La_{0.6}Sr_{0.4}FeO_3$ (LSFO) sample undergoes a metal-insulator (MI) transition at ~200 K, evidenced by a jump in the resistivity of more than 1 order of magnitude with decreasing temperature. This MI transition is accompanied by an antiferromagnetic ordering. However, details of the electronic structure have not been clarified thus far. In this study, the authors have measured resonant soft-X-ray emission spectroscopy (SXES) spectra of $La_{0.6}Sr_{0.4}FeO_3$ thin film. The purpose of this study is to estimate experimentally the magnitudes of the on-site Coulomb energy (U_{dd}) and the crystal-field splitting (10Dq) through the study of *d-d* transitions.

LSFO thin film was deposited on an MgO (100) substrate by pulsed laser deposition (PLD) using a ceramic target. The LSFO ceramics target were synthesized by a solid state reaction method and pressed into cylinders, then sintered in air at 1200°C for 6 h. The target density was approximately 98 %.

The PLD system was arranged in a symmetric configuration with a rotating substrate holder for compositional uniformed. The base pressure was ordinary 3×10^{-8} Torr, and the substrate was inserted from a load lock chamber to main chamber a low base pressure. A KrF excimer laser (λ=248 nm) was used as the ablation beam. The repetition frequency and laser power were 5 Hz and 220 mJ, respectively. The oxygen gas pressure and substrate temperature were fixed at 10 mTorr and 700°C. The film thickness was approximately 20 nm. The prepared LSFO thin film on MgO (100) substrate exhibited the *c*-axis orientation.

The X-ray absorption spectroscopy (XAS) and SXES spectra were carried out at the undulator beamline BL-19B at the Photon Factory (PF) of the High Energy Accelerator Organization (KEK). Synchrotron radiation was monochromatized using a varied-line spacing place grating whose average groove density is 1000 lines/mm. The SXES spectra were measured in the depolarized configuration. The energy resolution was higher than 0.7 eV at $h\nu$=700 eV. The energy axis was calibrated by measuring the 4*f* core level of an Au film deposited in situ on the sample substrate.

Figure 1 shows the Fe 2*p* XAS spectrum of LSFO thin film. The spectrum consists of two parts derived from the spin-orbit split of L_3 ($2p_{3/2}$) and L_2 ($2p_{1/2}$) states. They are further split into the t_{2g} and e_g states due to the octahedral ligand field. The crystal-field splitting (10Dq) corresponding to the energy separation between t_{2g} and e_g states is 1.5 eV. The spectral shape, peak position, and 10Dq are similar to those of $La_{1-x}Sr_xFeO_3$, which was theoretically calculated assuming a high-spin $[t_{2g}]^3[e_g]^2$ ground state. The vertical bars, which are labeled from 1 to 6, indicate the selected photon energies for resonant SXES measurements.

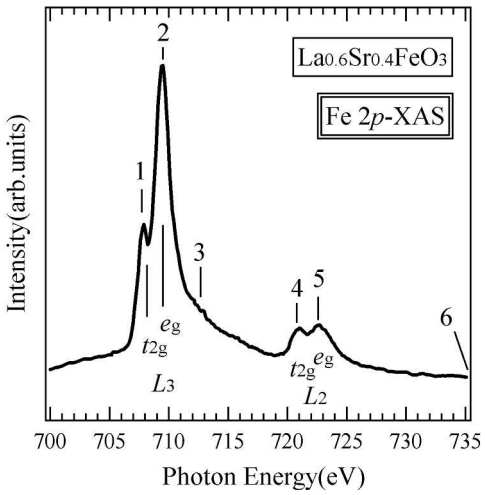

Fig. 1: Fe 2*p* XAS spectrum of LSFO thin film.

Figure 3 shows the SXES spectra of LSFO thin film, which the abscissa is the Raman shift (or energy loss) from the elastic scattering. The elastic scattering peak is located at 0 eV. The Fe $3d \rightarrow 2p$ fluorescence peaks shown as four solid bars shift to the higher energy side with increasing excitation energy. Eight soft-X-ray Raman scattering peaks shown as vertical dashed lines α, β, χ, δ, ε, ϕ, γ, and η are observed at -7.1, -6.2, -5.4, -4.8, -4.4, -3.2, -2.7, and -1.3 eV, respectively, from the elastic scattering peak. The soft-X-ray Raman scattering peaks of spectra 2 and 3 excited at the L_3 absorption edge overlap with the Fe $3d \rightarrow 2p$ fluorescence peaks. The spectrum 1 excited at L_3 (t_{2g}) shows apparent soft-X-ray Raman scattering structures since their positions are located at lower energy side than fluorescence peaks. Similar structures have observed in the SXES spectra of $BiFeO_3$, which has similar crystal structure and electronic configuration. The elementary excitation of the Raman scattering is considered to correspond to the valence band transition. Therefore, the energy positions of these Raman scattering peaks may correspond to the transition from the valence band and conduction band.

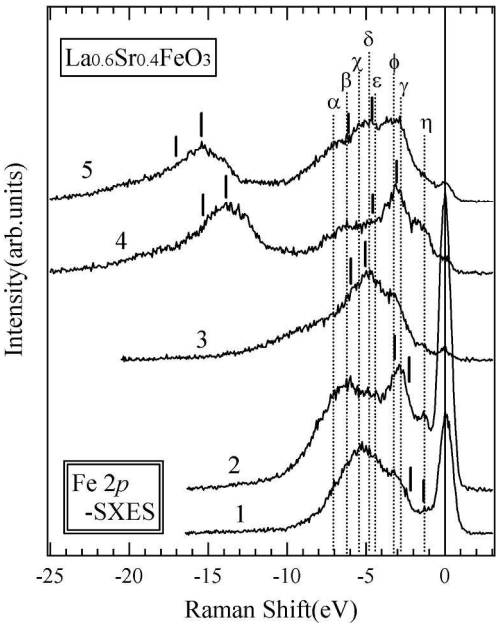

Fig. 2: Fe 2*p* SXES spectra of LSFO thin film presented on a relative emission energy scale compared to the elastic scattering.

Figure 4 shows the O 1*s* and Fe 2*p* fluorescence spectra and O 1*s* XAS spectrum of LSFO thin film, where the abscissa is the relative energy to Fermi level (E_F). The O 1*s* and Fe 2*p* SXES spectra reflect the Fe 3*d* and O 2*p* PDOS, respectively, in the valence band. The energy position of O 2*p* state overlaps with that of Fe 3*d* state. This result indicates that the Fe 3*d* state hybridizes with O 2*p* state in the valence band. The valence band has three structures labeled A, B and C. The Fe 3*d* contribution is more significant in the B and C peaks. In particular, the Fe 3*d* PDOS is dominantly at near E_F. On the other hand, from the dipole selection rule, it is understood that the O 1*s* XAS spectrum of Fe oxide corresponds to transitions from O 1*s* to O 2*p*. The conduction band has three structures. Two sharp peaks at ~2.2 and ~3.7 eV from E_F correspond to the t_{2g} and e_g states, respectively, of Fe 3*d* conduction band. The *h* peak at near E_F is considered to be the hole-induced state.

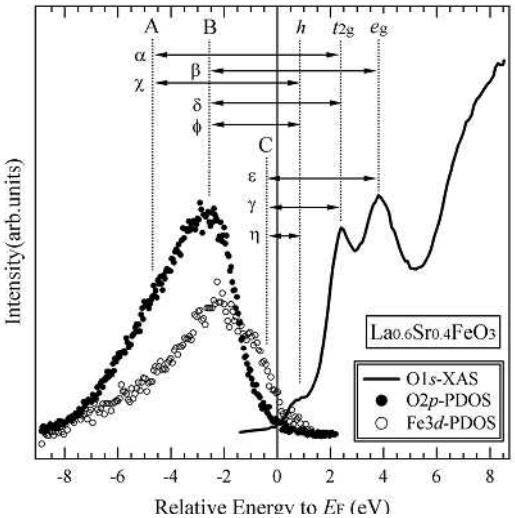

Fig. 2: Fe 2*p*, O 1*s* fluorescence and XAS spectra of LSFO thin film presented on a relative energy compared to E_F. .

Here, the authors estimate the eight soft-X-ray Raman scattering peaks (α, β, χ, δ, ε, ϕ, γ, and η) in Fig. 2. α (χ) corresponds to the transitions from A to t_{2g} (hole induced state). δ (ϕ) corresponds to the transitions from B to t_{2g} (hole induced state). β (ε) corresponds to the transitions from B (C) to e_g. η (γ) corresponds to the transitions from C to t_{2g} (hole induced state). The soft-X-ray Raman scattering peaks of ε, γ, and η are attributed to the pure *d-d* transitions from the occupied Fe 3*d* (e_g) state to unoccupied Fe 3*d* state, because the O 2*p* PDOS does not exist in C peak located at near E_F.

Electronic States of Superconductor without Inverse Symmetry

Masaaki Hirai[1, 2], Hiroyuki Okazaki[1], Yuichiro Yao[3], Sho Yoshida[3],
Yuji Muraoka[1, 2], Takayoshi Yokoya[1, 2]
[1] *Division of Frontier and Fundamental Sciences,*
Graduate School of Natural Science and Technology,
[2] *Research Laboratory for Surface Science, Faculty of Science,*
[3] *Mathematics and Physics, Graduate School of Natural Science and Technology,*
*Okayama University, Tsushima-naka, Kita-ku, Okayama 700-8530, Japa*n

Silicon carbide (SiC) is a candidate material for hard-electronic devices to have the excellent physical properties such as high electric breakdown field, high saturation electron velocity and tolerance to high-temperature and radioactive field compared with silicon (Si) which is a popular electronic material. By the way, for heavily Boron-doped SiC the property of superconductor has been discovered by Zhi-An. Ren, *et al*. in 2007[1], where a critical transition temperature T_c is ~1.4K. In the first place, the superconductivity of semiconductors has been found by E.A. Ekimov, *et al*. for heavily Boron-doped diamond in 2004[2]. After that it is reported that heavily Boron-doped Si also indicates the property of superconductor in 2006[3]. Therefore it is interest from the view point of electron spectroscopy that the semiconductors such as SiC and Si indicate the superconductivity by heavily impurity-doping until a semiconductor-to-metal transition. Especially, the crystalline structure of SiC has not inverse-symmetry for many polytypic structures such as 4H-SiC and 3C-SiC. Because, BCS (J. Bardeen, L. Cooper, and R. Schrieffer) theory for common superconductors is explained by the pairing of electrons close to the Fermi level into Cooper pairs through interaction with the inverse-symmetric crystalline lattice.

We have studied electronic states of heavily Aluminum (Al)-doped and Phosphor (P)-doped 4H-SiC specimens by using a soft X-ray emission spectroscopy (SXES). SXE spectra have characteristics to give information of partial density of states in the valence band density of states (VB-DOS), where an electron in a shallow core level is excited by an incident photon. Because different wave functions for each element in a material under study can be separated due to the dipole selection rule in an electron transition to give rise to a photoemission. Therefore, we can obtain a specific signal for an element which can be used as a finger print, otherwise it is difficult. Further, it is a very powerful tool to a nondestructive buried interface and surface layer analysis of a thin-film on substrate.

The experimental samples were formed as follows. The epitaxial layer with film thickness of 10μm was deposited on 4H-SiC(0001) Si- and C-face substrates. Al or P atoms with the dose concentration of about $3x10^{21}$ atoms/cm^3 were doped by an ion-implantation into these wafers and then these impurity levels were activated by post-annealing. The experiments of SXES were performed at the beamline 19B in Photon Factory facility, KEK.

Figure 1 shows the Si $L_{2,3}$ SXE spectra; (a) a 4H-SiC(0001) bulk sample (blue dots) and (b) an Al-doped specimen in 4H-SiC(0001) Si-face (red dots). Electrons within the Si $L_{2,3}$ level were excited by photon energy of 130eV. The spectrum of (a) is characterized by a hump of 86.0eV, a main peak of 91.6eV and plateau region from 92.0eV to 97.5eV including a small peak at 97.0eV. The spectrum of (b) is characterized by a hump of 86.0eV and double main peaks of 91.6 and 98.0eV. As compared the spectrum (a) with (b), the peak intensity of 98.0eV in spectrum (b) increases. This suggests that the partial density of states near top of the valence band (near Fermi level) in relation to Si *3s* and/or *d* states increases due to heavy concentration of Al-doping level. However, the spectrum shape under 93eV such as the hump of 86.0eV and the peak of 91.6eV does not change little for both samples. Thus one can conclude that the effect of heavy concentration in Al-doping level reflects the intensity of

spectrum near Fermi level. Because, it is considered that the density of states near the top of valence band plays an important part for the appearance of superconductivity.

Next, the C Kα emission spectra obtained from the same spacemen as the Si $L_{2,3}$ SXE spectra are shown in Fig. 2; (a) a 4H-SiC (0001) bulk sample (blue dots) and (b) an Al-doped specimen of 4H-SiC(0001) Si-face (red dots). Incident photon energy is 350eV. Both spectra are similar to the shape with a terrace at 272eV and peak energy position at 278.5eV. Therefore one can say that the partial density of states in relation to C *2p* electrons does not change due to heavy concentration in Al-doping level, which entirely differs from the Si $L_{2,3}$ SXE spectra.

The Si $L_{2,3}$ and C Kα emission spectra reflect the partial density of states in the valence band. Therefore it is considered that aluminum atoms doped by the ion-implantation are substituted at Si-sites. Further it is guessed that excess Si atoms remain around Si-sites, for example interstitial Si-sits, by reason of Al-atoms substitutions of Si-sites. As a result of substitutions, it is suggested that the intensity of Si $L_{2,3}$ SXE spectrum in Fig.1 (b) increases at 98.0eV. Furthermore it is expected that the crystallographic lattice constant changes by heavy Al-doping. If the lattice constant should changes, the density of states for the valance band will be affected by heavy Al-doping. Because speaking with regard to the heavily Boron-doped diamond, the lattice constant changes in correspondence with the dope concentration[4].

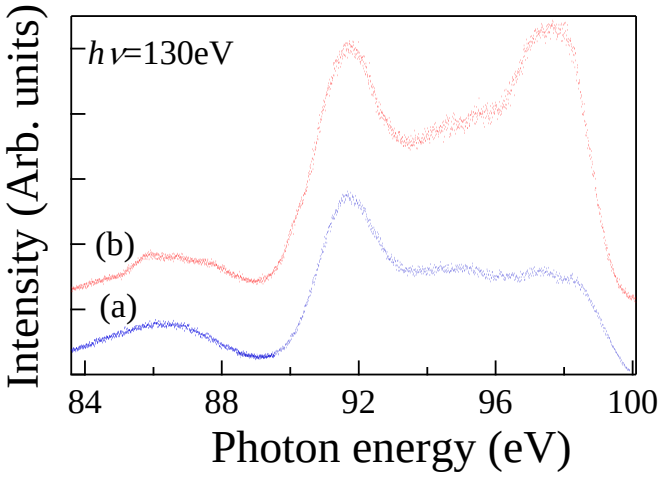

Fig. 1. The Si $L_{2,3}$ SXE spectra; (a) a 4H-SiC(0001) bulk sample (blue dots) and (b) an Al-doped specimen in 4H-SiC(0001) Si-face (red dots). Incident photon energy is 130eV.

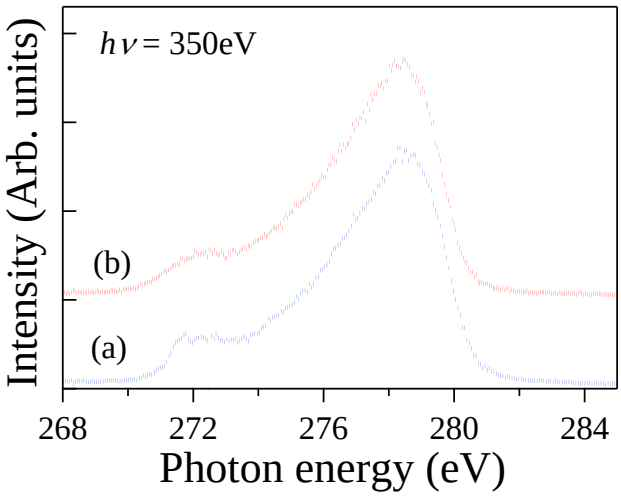

Fig. 2. The C Kα SXE spectra; (a) a 4H-SiC(0001) bulk sample (blue dots) and (b) an Al-doped specimen in 4H-SiC(0001) Si-face (red dots). Incident photon energy is 350eV.

These results are summarized as follows. Though the Si $L_{2,3}$ SXE spectrum shape is changed in the heavy Al-doping concentration, the C Kα emission spectrum does not change. It is concluded that Al-doped atoms are substituted at Si-sites.

References

[1] J. Phys. Soc. Jap. **76**, 103710 (2007).
[2] Nature **248**, 542 (2004).
[3] Nature **444**, 465 (2006)
[4] Vacuum **45**, 1014 (1994).

Atomic and electronic band structure of the √21×√21 phase formed by Au adsorption on the Ag/Si(111)-6×1 surface

Fumitaka Nakamura[1,2,*], Yasuo Takeichi[1,2], Ayumi Harasawa[2], Akito Kakizaki[2] ,and Iwao Matsuda[2]

[1]*Graduate School of Science, The University of Tokyo, Hongo Tokyo 113-0033*

[2] *Synchrotron Radiation Laboratory, The Institute for Solid State Physics, The University of Tokyo, Kashiwa, Chiba 277-8581*

Introduction

Surface superstructures, formed by adsorption of noble metals on Si(111), have been intensively studied. Among them, √21×√21 phases have widely attracted attention because of their interesting atomic structures and high conductivity surface state. Many types of the √21×√21 structure have been reported, and their models have been examined. We can prepare these structures by adsorbing alkali or noble metal atoms on the √3×√3 structure, formed on Si(111)-7×7 by depositing noble metal atoms, to be 1.1～1.2 ML for their total coverage[1,2]. The √21×√21 phases are thought to be a strong candidate for the two-dimensional Hume-Rothery-type electron compound, which forms the same long-range ordered phase when a ratio of electron/atom density is equal[3]. Indeed, a number of the valence electrons in the unit cell is all 3 of these similar √21×√21 structure[4]. In this research, we found a new procedure to make √21×√21 phase, analyzing the atomic structure and electronic band structure by using Scanning Tunneling Microscopy (STM) and angle-resolved photoelectron spectroscopy (ARPES).

Results and Discussion

In order to prepare the (Au+Ag)/Si(111)-√21×√21 surface, we chose a periodic array of 1-D Ag atomic chains, a Ag/Si(111)-6×1 surface, prepared by the 0.3 ML-Ag deposition, as a starting surface. By the Au deposition at 400K, the (Au+Ag)/Si(111)√21×√21 surface was observed. We estimated the deposition rate by well known coverage of Ag/Si(111)-√3×√3, and Au/Si(111)-√3×√3, and confirmed the total metal coverage of 1.1～ 1.2 ML as reported previously on the √21×√21 phases[1,2,4,5]. We checked these phases by Low Energy Electron Diffraction, LEED (Figure1). We can see the clear spot corresponding to √21×√21 periodicity in Figure 1.

Figure 2 (a) and (b) show empty- and filled-state STM images of the surface taken at room temperature, respectively. The surface was fully covered with the √21×√21 phase. A circle at the corner of the unit cell of (a) and (b) corresponds to the 3 adatoms on √3×√3 phase, and these images are almost the same with other STM images of √21×√21 phases, despite the fact that the deposited Ag and Au ratio are different from each other[5,6].

Fig. 1: LEED pattern of √21×√21 phase. Area surrounded by white lines corresponds to √21×√21 unit cell.

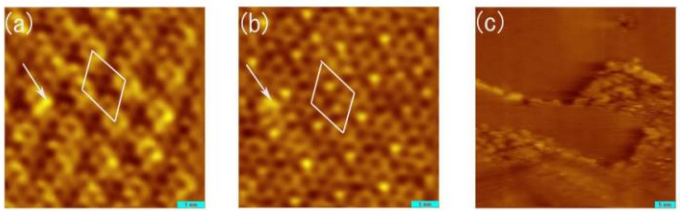

Fig. 2: Unoccupied state STM image (Vs=+1.50V, 7nm×7nm square) of (Au+Ag)/Si(111)-√21×√21 phase (a), occupied state STM image (Vs=-1.50V, 7nm×7nm square) (b), and unoccupied state STM image(Vs=+1.58V, 50nm×50nm square) (c). Vs corresponds to the sample bias. White arrows of (a), and (b) are the marking impurity indicating that (a) and (b) are the same region. Area surrounded by white lines in (a), (b) are √21×√21 unit cell.

Figure 3(a) is gray-scale band diagram obtained from the second derivative of the smoothed spectra of ARPES obtained at beamline 18A at Photon Factory using VG-Scienta SES-100 hemispherical analyzer. Fig.3 (b) corresponds to an energy-versus-wavenumber plot obtained by reading the peak of the spectra Fig.3 (a). A parabolic dispersion is clearly visible and it means that there exists a two-dimensional free electron system in the $\sqrt{21}\times\sqrt{21}$ phase. In addition, Fermi energy of this phase is about 1.1 eV from the band bottom and it is higher than Fermi energy of Ag/Si(111)-$\sqrt{3}\times\sqrt{3}$, which is 0.3 eV from the band bottom[7]. This means that additional adatoms have doped electrons to surface state bands. We can also calculate the effective mass of $\sqrt{21}\times\sqrt{21}$ phase by fitting parabolic curve to the obtained data in Figure 3(b). Effective mass m^* is estimated as $m^*/m_e=0.29\pm0.2$. m_e is mass of free electron. It is similar value of $0.26m_e$, which is effective mass of $\sqrt{21}\times\sqrt{21}$ phase prepared with other methods[6]. Fermi wavenumber is estimated as $0.28Å^{-1}$ and the number of valence electrons in the unit cell is calculated to be 3.3, which is a reasonable value compared to the previous researches.

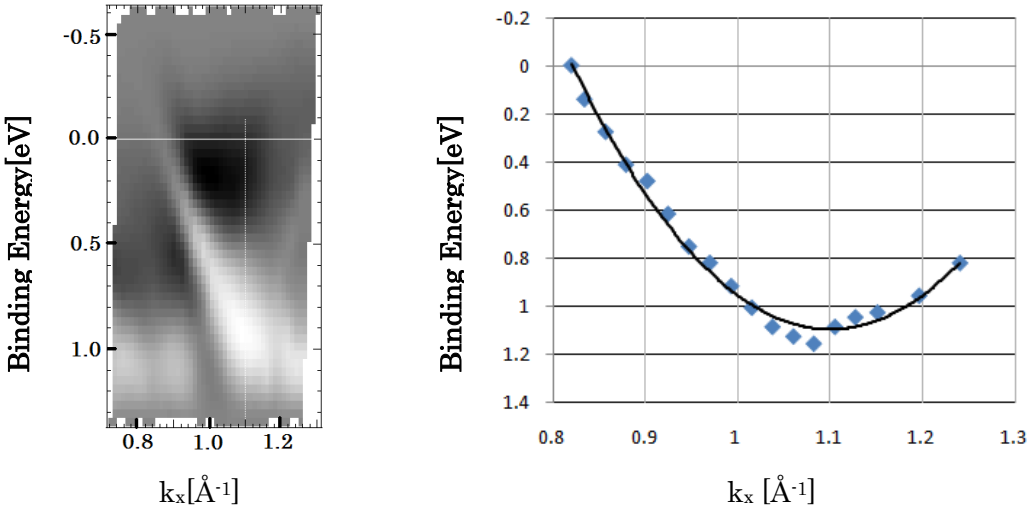

Fig. 3: (a) is second derivative of ARPES spectra. (b) is Energy-versus-wavenumber plot of $\sqrt{21}\times\sqrt{21}$ phase plotted from (a). Parabolic dispersion is visible. Fermi wavenumber is estimated as $0.28Å^{-1}$, the number of valence electrons in the unit cell is 3.3, and effective mass is calculated to be $m^*/m_e=0.29$.

Conclusion

We performed the STM and ARPES measurements of the $\sqrt{21}\times\sqrt{21}$ phase made by adding Au for 0.9ML on Ag/Si(111)-3×1. We observed the parabolic band dispersion and about 3 valence electrons in the unit cell. The atomic and electronic band structure is similar to the other $\sqrt{21}\times\sqrt{21}$ phases despite the fact that the deposited Ag and Au ratio are different from each other.

References

[1] C. Liu *et al.*, Phys. Rev. B **74**, 235420 (2006).
[2] H. Jeong, *et al*., Phys. Rev. B **77**,235425 (2008).
[3] C. Kittel, Introduction to Solid State Physics, Chapter21 (Wiley, 1995).
[4] I.Matsuda *et al* . (to be published)
[5] C. Liu *et al.*, Phys. Rev. B **71**, 041310 (2005).
[6] I.Matsuda *et al* . Phys. Rev. B **71**,235315 (2005)
[7] T.Hirahara *et al.* e-J. Surf. Sci. Nanotech. Vol. 2 (2004) 141-145

A New Soft X-ray Beamline BL07LSU at SPring-8: Design and Status

S. Yamamoto[1], Y. Senba[2], H. Ohashi[2], I. Matsuda[1]
[1]*Synchrotron Radiation Laboratory, The Institute for Solid State Physics, The University of Tokyo*
[2]*Japan Synchrotron Radiation Research Institute, SPring-8*

A new soft X-ray beamline with a 27 m-long undulator, BL07LSU, has been constructed at SPring-8 in order to perform advanced X-ray spectroscopies for materials science. In 2009 the SPring-8 BL07LSU celebrated its grand opening after two years of construction period and came into operation for user experiments. In this report, we present the basic design of the beamline and the current status of beamline commissioning. The future development plan in 2010 will also be described.

The designed optical properties for SPring-8 BL07LSU are summarized in Table 1. These optical properties are achieved by the key components of the beamline such as undulator and monochrometer. The 27 m-long undulator at SPring-8 BL07LSU has been developed with a capability of polarization control [1]. It consists of eight segments of figure-8 undulator and seven phase shifters. Four undulator segments generate horizontally-polarized radiation as the first harmonic, and the other four segments generate vertically-polarized radiation. The helicity of the circular polarization and the linear (horizontal or vertical) polarization can be controlled by the phase shifters placed between the segments, which adjust the relative phase of travelling electrons in the segments. A layout of the beamline is schematically illustrated in Fig. 1 with the optical parameters of mirrors and gratings. The monochromator at SPring-8 BL07LSU is an entrance-slitless variable-included-angle Monk-Gillieson mounting type with a varied-line-spacing plane grating (VLS-PGM) [2]. To optimize the energy resolving power, the included angle of the grating can be varied by off-axis rotation of plane mirror. Two VLS gratings with different central groove densities (600 and 1200 lines/mm) are planned to be used.

Parameter	Value
Energy range	250∼ 2000 eV
Resolving power (E/ΔE)	>10,000
Flux	10^{12} photons/s/0.01%BW
Spot size	<10 μm
Polarization	Linear (Horizontal and Vertical) and Circular

Table 1 Designed optical properties of a new soft X-ray beamline BL07LSU at Spring-8

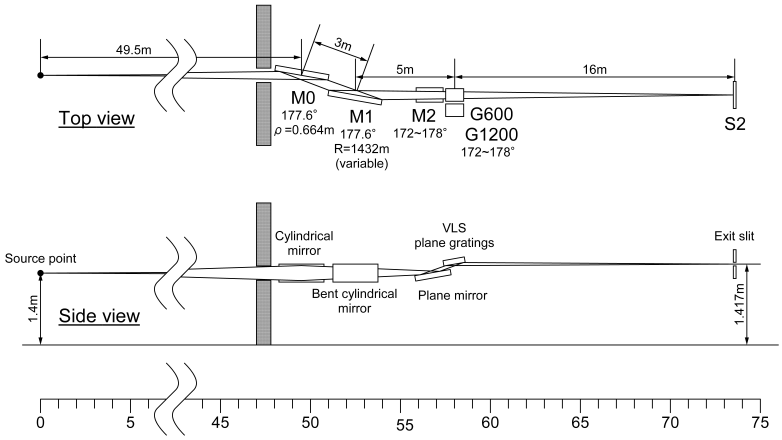

Figure 1 Schematic layout of a new soft X-ray beamline BL07LSU at Spring-8

Next the current status of beamline commissioning is reported. In 2009, as Phase I of the beamline construction, four segments of undulator and three phase shifters which generate horizontal polarization as the first harmonic have been installed. For monochromator, a 600 lines/mm grating has been installed. In the beamline commissioning, the designed photon energy range (250~2000 eV) has been confirmed to be available. The energy resolving power was evaluated from X-ray absorption spectroscopy (XAS) spectra of N_2 and Ne gases; $E/\Delta E \sim 10^4$ was confirmed at 400 eV (N_2) and 870 eV (Ne) (Figs. 2 and 3). The photon flux was estimated to be close to the designed values using a photodiode. The small spot size of 92 nm was achieved at one of the experimental endstations by the refocusing optics of Fresnel zone plate. At present, the horizontal polarization of X-ray is only available by the installed four undulators and phase shifters

In the coming 2010, as Phase II of the beamline construction, the remaining four segments of undulator and phase shifters will be installed, which will allow for the full control of polarizations. To evaluate the linear polarization and the helicity of the circular polarization, the development of soft x-ray polarimeters using multilayer optics and X-ray magnetic circular dichroism is under way. In addition, a 1200 lines/mm grating are planned to be installed to achieve the higher energy resolving power.

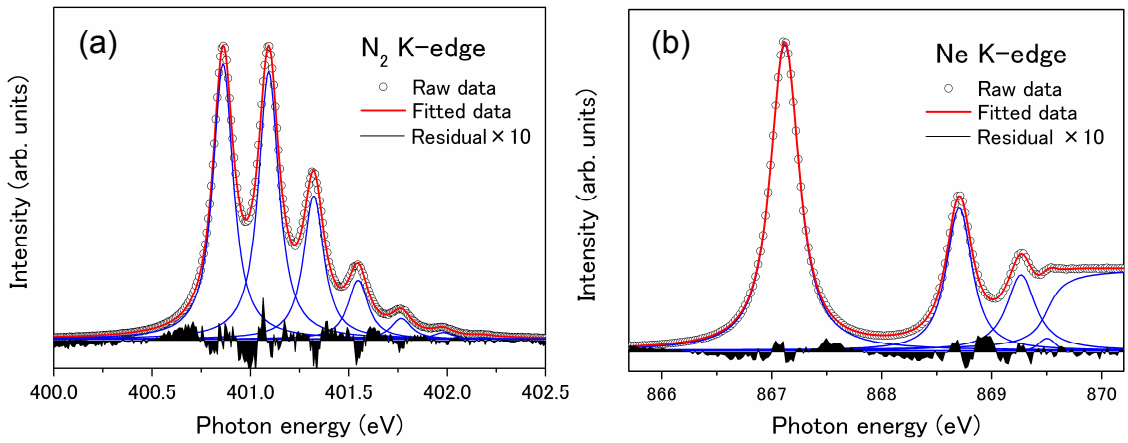

Figure 2 Total ion yield X-ray absorption spectra for N_2 K-edge (E~401 eV) (a) and Ne K-edge (E~ 867 eV) (b). The energy resolving power ($E/\Delta E$) was estimated to be 8700~10000 from full-width-half-maximum (fwhm) of Gaussian in the peak fit using Voigt functions; (a) N_2 K-edge, fwhm of Gaussian and Lorentzian were 38 and 114 meV. (b) Ne K-edge, fwhm of Gaussian and Lorentzian were 100 and 240 meV.

References

[1] T. Tanaka and H. Kitamura, Nucl. Instrum. Methods Phys. Res. A, 490 (2002) 583.
[2] K. Amemiya and T. Ohta, J. Synchrotron Rad., 11 (2004) 171.

Development of picosecond time-resolved soft x-ray spectroscopy system at SPring-8

Manami Ogawa*[1], Susumu Yamamoto[1], Yuka Kousa[2], Akiko Fukushima[1], Ayumi Harasawa[1], Hiroshi Kondo [2], Akito Kakizaki[1], Iwao Matsuda[1]

[1]*Synchrotron Radiation Laboratory, The Institute for Solid State Physics, The University of Tokyo* [2]*Department of Chemistry, Keio University*

Introduction

Recent developments of short pulsed light sources, such as laser and synchrotron radiation (SR), and high time-resolution detectors enable real time measurements of dynamic processes. Especially it is of strong interest to develop a new combination technique between SR and laser for pump-probe experiments and free electron laser. Pulse width of SR is typically several tens picoseconds, which is comparable with various phase transitions and surface chemical reactions. By combining SR with laser, therefore, one can investigate meta-stable transition states excited by laser pulse and the following relaxation processes through the change of electronic and crystalline structures. Here we report the current status of development of time-resolved soft x-ray photoemission spectroscopy (TRPES) system at SPring-8 BL07LSU.

Experimental setup

Our TRPES system is composed of three parts: (1) laser system, (2) photoelectron analyzer and (3) timing control circuit.

(1) Laser system and synchronizing two light sources

To perform TRPES experiments, we need to synchronize two independent light sources, SR and laser, and control a delay time between two lights. The difficulty in TRPES experiments lies in the fact that SR and laser have completely different frequency: kHz~MHz for laser and several hundreds of MHz for SR. The frequency of laser is determined by a cavity length of oscillator laser, while the frequency of SR depends on the frequency of RF cavity and filling pattern in a storage ring. Our laser system consists of three lasers: pump laser, oscillator laser, and amplifier. The oscillator laser (Halcyon, KM-labs) has a feedback circuit, which adjusts the cavity length to make six times of laser repetition frequency equal to the frequency of RF signal at SPring-8 (508.58MHz). The repetition rate of oscillator laser is 84.76 MHz. In the amplifier (Odin, Quantronix), the repetition rate is reduced by pulse picker (Pockels cell) to once every 208 cycles of SR. As a consequence, the output laser pulse of amplifier is synchronized to SR pulses and has 35 fs pulse width, 2.5 mJ/pulse energy and 1.004 kHz repetition rate.

(2) Photoelectron analyzer

Our new photoelectron analyzer is ARTOF10k (VG Scienta), which is a time-of-flight (TOF) type analyzer equipped with two dimensional delay line detector (DLD). The working principle of TOF analyzer is that kinetic energies (E_{kin}) are determined by measuring flight times of photoelectrons. Thus the TOF analyzer requires no slit to gain the energy resolution; as a result, the ARTOF analyzer has 250 times better transmission efficiency than conventional hemispherical analyzers. In order to achieve a high energy resolving power, $E_{kin}/\Delta E > 10{,}000$ (10k), and a large detection angle, the retarding lens system is installed in the ARTOF analyzer. The retarded electrons have prolonged flight times. The ratio of flight time to time accuracy of analyzer (~100 ps, determined by DLD) becomes larger, and hence, the energy resolution becomes higher. In ARTOF fast electrons up to 1000 eV can be measured with good energy resolution. In addition to good energy resolution, ARTOF can measure two dimensional photoelectron spectra (θ, ϕ) at once with good angular resolution of 0.08° with a detection angle of $\pm 15^{o}$.

TOF analyzer requires a pulsed light source and to know t_0 (the time when light reaches sample) precisely. For the precise determination of t_0, we measure the reflected photons from the sample by the DLD detector. An example of photon measurement is shown in Fig. 1(a). From the arrival time of photons at the detector, the distance between sample and detector, and speed of light, we can determine t_0 very precisely. It should also be noted that the measured spectrum is in perfect agreement with the time structure of the filling pattern in the D-mode operation at SPring-8 (Fig. 1(b)), five bunches and one filling part. From the measurements we confirmed the achieved time resolution of DLD is around 350 ps. It is much shorter than bunch interval, therefore DLD does not make worse the time resolution of TRPES.

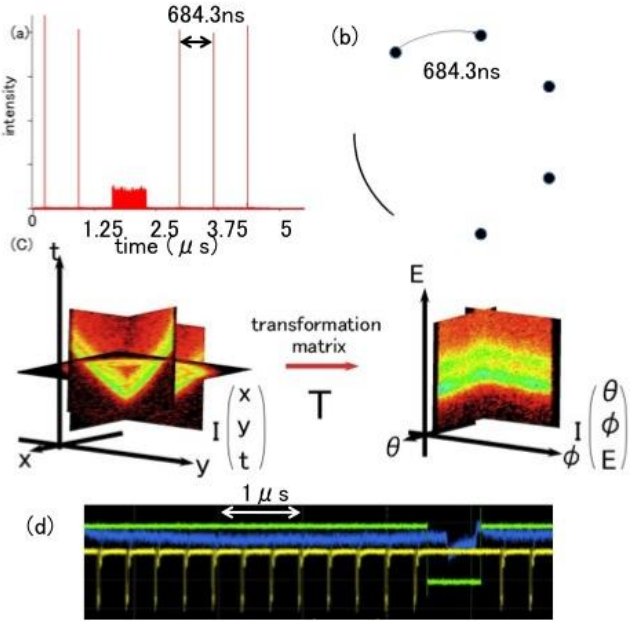

Figure 1 (a)Photon measurement. The observed pattern represents D-mode bunch structure. t=0 is arriving time of trigger signal which we send.(b) The filling pattern of D-mode in SPring-8 A cycle.(c) Si 2p of TOF 2D detection. Left: Si 2p, as a function of time, x and y. Because of the lens system, photoelectrons reach faster at the center than at the edge of detector. Right:as a function of energy, θ and ϕ. (d)The display of oscilloscope: Yellow is lacking trigger signal for t_0, blue is current signal of 0 order light from Au plate just after grating. Green is one revolution of SR. The trigger signal (yellow) is blinded to filling part of SR light(the square part of blue).

(3) Timing control circuit:

The TRPES system requires trigger signals and their precise timing control. In our experiment the timing control circuit (84DgR5A01, Candox) plays important roles as follows. The first role is a delay generator between laser and SR. The circuit generates a delay with 1 ps accuracy in RF signal which is the input signal for a feedback circuit in laser oscillator. The second role is to determine a laser frequency. The circuit sends a trigger signal to pulse picker in the amplifier. If the RF signal (508.58 MHz) is divided by the harmonic number of SPring-8 (2436=2×2×3×7×29), the frequency becomes equal to one revolution of the ring. If divided by integral (n) multiple of harmonic number, the frequency is equivalent to once every n cycles of the ring. Since the amplifier can be operated only in 1 kHz~2 kHz, n=105~209 was chosen to be used. The third role is t_0 trigger for ARTOF. In pump-probe TRPES experiments, the frequency for ARTOF is identical to laser frequency. In the static PES experiments without laser, however, the different trigger signal for ARTOF is prepared by the timing control circuit to measure photoelectrons from all the bunches except for the filling part in the D-mode filling pattern (in Fig. 1(d)).

Results and Conclusion

Figure 1(c) shows the time of flight and energy spectra for Si 2p core level. The left panel of Fig.1(c) is the time of flight spectra as a function of x-y axes [I(t,x,y)]. Photoelectrons reach faster at the center than at the edge of DLD because due to the lens system photoelectrons with large emission angles go through much longer path than electrons with normal emission. The right panel is the transformed spectra of the left panel; time of flight, x, and y are transformed into kinetic energy and emission angles θ and ϕ. It took1~2 minutes to record the PES spectrum in Fig. 1(c).

In summary, we have succeeded in measuring x-ray photoemission spectra with the new type analyzer ARTOF. Moreover we confirmed the synchronization between laser and SR light of SPring-8 with several ps accuracy. Now we are preparing to perform TRPES measurements on carrier dynamics on semiconductor surfaces.

Direct spectroscopic evidence of spin-dependent hybridization between Rashba-split surface states and quantum-well states

Ke He,[1] Yasuo Takeichi,[1] Manami Ogawa,[1] Taichi Okuda,[1] P. Moras,[2] D. Topwal,[3]
Ayumi Harasawa,[1] C. Carbone,[2] Akito Kakizaki,[1] and Iwao Matsuda[1]

[1]*Institute for Solid State Physics (ISSP), the University of Tokyo, 5-1-5 Kashiwanoha, Chiba 277-8581, Japan*

[2]*Istituto di Struttura della Materia, Consiglio Nazionale delle Ricerche, Trieste, Italy*

[3]*International Centre for Theoretical Physics (ICTP), Strada Costiera 11, 34100 Trieste, Italy*

In nanometer- or atomic-scale structures, size reduction implies an increase of the surface/volume ratio and the emergence of various quantum phenomena, intimately linked to the formation of electronic states different from those of the corresponding bulk materials. Recently, there have been vigorous investigations on nanometer-thick metal films, showing the quantum size effect, and on two-dimensional surfaces with large spin-orbit interactions, exhibiting the Rashba effect. In the present study, we prepared an quantum metal Ag(111) film, covered with a Rashba-type surface alloy of $\sqrt{3} \times \sqrt{3}$-Bi/Ag[1], to examine mixture of these two effects, especially their spin characters

Spin-polarized band structure of the system was investigated by high-resolution spin- and angle-resolved photoemission spectroscopy (SARPES) at KEK-PF BL-19A.

Figure 1 shows a series of the spin-up and spin-down SARPES spectra. The spin-up bands show free electron dispersion curves of the quantum-well states (QWS), while the spin-down ones show complicated band features. The former indicates that there is little interaction for the spin-up QWS with the surface state (SS) and the latter means that there is strong QWS-SS interaction. From these results it is found that the SS bands, spin-split by the Rashba effect, make spin-dependent hybridization with QWS in the nanofilm. The QWS subbands of the same spin orientation with the SS bands formed energy gap-opening, while those of the opposite orientation kept the free-electron band dispersion. Figure 2 shows a summary of the spin-dependent band diagram of the Ag(111) quantum film covered with the $\sqrt{3} \times \sqrt{3}$-Bi/Ag surface. The results also indicate that the amount of the hybridization gap depends on the SS band and the wave vectors. The difference may be understood in terms of the symmetry-matching of wave functions between the QWS and SS bands [2].

The present results give the direct evidence of the spin-dependent hybridization between the Rashba-type SS and the QWS, demonstrating that in a non-magnetic metal film the spin-degeneracy of the valence levels can be lifted by hybridization with Rashba-type SS bands.

References:

[1] K. He, T. Hirahara, T. Okuda, S. Hasegawa, A. Kakizaki, and I. Matsuda, Phys. Rev. Lett., **101**, 107604 (2008).

[2] K. He, Y. Takeichi, M. Ogawa, T. Okuda, P. Moras, D. Topwal, T. Hirahara, C. Carbone, A. Kakizaki, and I. Matsuda, Phys. Rev. Lett. **104**, 156805(2010).

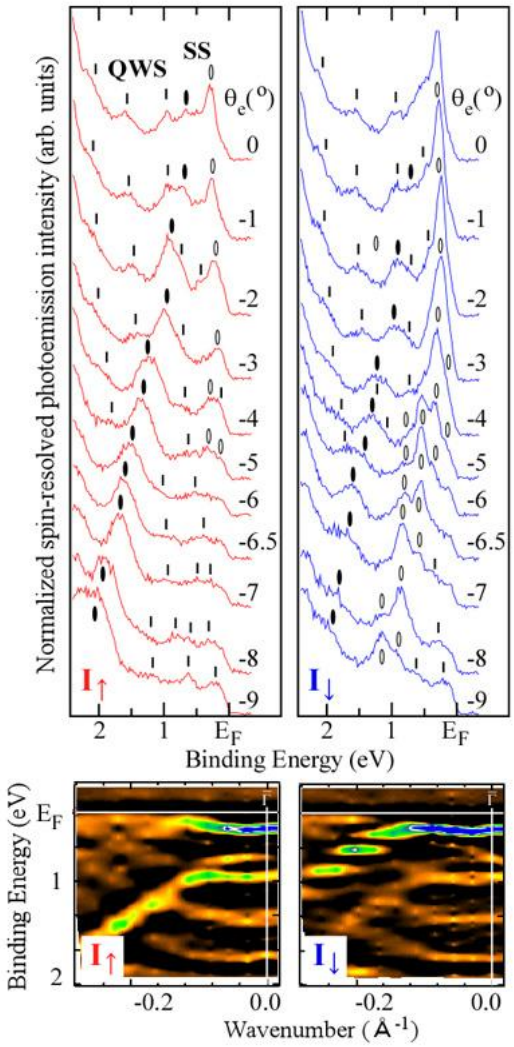

Fig. 1 SARPES spectra and band diagrams of (left) spin-up, $I_{\uparrow}$, and (right) spin-down, $I_{\downarrow}$, orientations. Dispersion of the SS and QWS bands are traced with symbols..

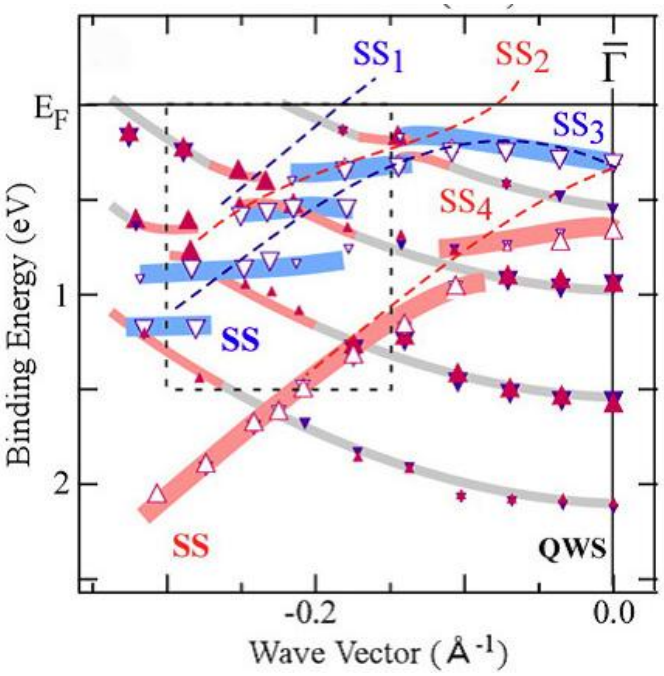

Fig.2 Summary of the spin-resolved dispersion plots of Fig.1. Up- (red) and down-pointing (blue) triangles identify the peak positions in the up- and down-spin spectra, respectively. The size of the symbols is proportional to the intensity of the corresponding feature in the photoemission spectra. Thick lines between symbols guide the eye through the dispersion of bands with SS, QWS or hybrid character. The dashed lines labeled SS_1, SS2, SS3, and SS_4 represent the surface states. Dotted boxes highlight a portion of the energy-momentum space where the spin-selective hybridization between SS and QWS bands occurs.

Direct mapping of the spin-filtered surface bands of a three-dimensional quantum spin Hall insulator

Akinori Nishide[1], Alexey A. Taskin[2], Yasuo Takeichi[1], Taichi Okuda[1,3], Akito Kakizaki[1], Toru Hirahara[4], Kan Nakatsuji[1], Fumio Komori[1], Yoichi Ando[2], and Iwao Matsuda[1]

[1]*Institute for Solid State Physics (ISSP), the University of Tokyo, 5-1-5 Kashiwanoha, Chiba 277-8581, Japan*

[2]*Institute of Scientific and Industrial Research, Osaka University, Ibaraki, Osaka 567-0047, Japan*

[3]*Hiroshima Synchrotron Radiation Center (HSRC), Hiroshima University, 2-313 Kagamiyama, Higashi-Hiroshima 739-0046, Japan*

[4]*School of Science, the University of Tokyo, 7-3-1 Hongo, Bunkyo-ku, Tokyo 113-0033, Japan*

The spin Hall effect, which makes it possible to produce spin currents without magnet, has recently attracted a lot of attention for its potential impact on future spintronics[1]. The spin Hall effect has also stimulated physicists not only to understand the intriguing phenomena, but also to extend the theoretical frameworks to the ``quantum spin Hall'' (QSH) effect[2,3], which is realized in a topologically non-trivial electronic state, as in the case of the quantum Hall effect. The theories of QSH effect have been constructed for two- and three-dimensions, and experimentalists have already attempted to obtain evidence for those topologically non-trivial states of matter.

In three dimensions (3D), there are four Z_2 invariants (η_0;η_1 η_2 η_3), representing time-reversal-invariant band structures[4,5]. When (η_0; η_1 η_2 η_3) = (1;111), the system is a 3D strong topological insulator, where the ``edge states'' (i.e. 2D surface states) form a Kramers pair of opposite spin currents flowing on a surface [Fig. 1] and are robust against disorder[6]. The spin lies within the surface plane and is perpendicular to the momentum (wavenumber) of the electron. The existence of such spin-current pairs is in sharp contrast to the trivial insulator where (η_0; η_1 η_2 η_3) = (0;000). Recently, the semiconductor alloy $Bi_{1-x}Sb_x$ (x~0.1) was predicted[6] to be a strong topological insulator, and subsequently a spin-integrated photoemission study has mapped the (111) surface states of this system at x=0.10 to find a trace of the predicted topological band structure[7]. However, since the surface states of topological insulators are expected to be spin-polarized, the spin characters of all the edge states in the surface Brillouin zone would need to be clarified for a complete proof of the 3D QSH phase. Therefore, it is important to conduct direct measurements of spin-polarized surface-state bands on the $Bi_{1-x}Sb_x$ crystals by spin- and angle-resolved photoemission spectroscopy (SARPES). In the present work, we took advantage of our new spin-polarized photoemission spectrometer with a high spin-polarimetry efficiency and a high energy

resolution[8], and determined all the spin-polarized bands of $Bi_{1-x}Sb_x$ (x = 0.12--0.13), as shown in Fig.2. The experiments were performed at KEK-PF BL-19A. Our results provide direct evidence for the QSH phase in the 3D topological insulator[9,10].

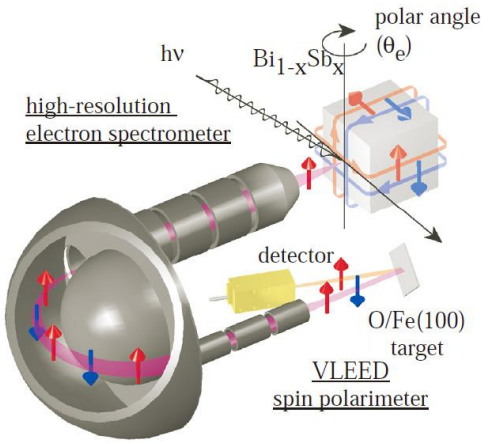

Fig.1 Schematic drawing of the high-resolution spin- and angle-resolved photoemission spectroscopy (SARPES) measurements. Spin-polarized (SP) electrons are depicted as up (red) and down (blue) arrows. Spin currents are also depicted for the edge states in the 3D quantum spin-Hall phase, from which the SP photoelectrons are emitted into a high-resolution electron spectrometer and the high-yield very low energy electron diffraction (VLEED) spin polarimeter.

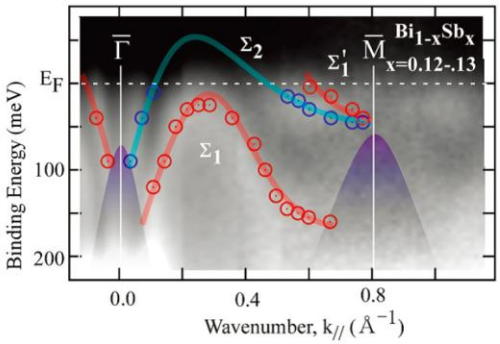

Fig.2 Spin-polarazied band dispersions of the surface states of $Bi_{1-x}Sb_x$ (x=0.12-0.13). The spin-resolved data are plotted with open circles and overlaid on a spin-integrated gray-scale diagram. Spin-up (spin-down) bands are colored in red (blue) and their dispersion curves are schematically traced by thick lines. The bulk band projection, tentatively estimated from the ARPES data, is shown as the shaded purple area.

References

[1] S. Murakami, N. Nagaosa, and S.-C.Zhang, Science **301**, 1348 (2003).

[2] S. Murakami, Phys. Rev. Lett. **97**, 236805 (2006).

[3] S. Murakami and S. I. Kuga, Phys. Rev. B **78**, 165313 (2008).

[4] C. L. Kane and E. J. Mele, Phys. Rev. Lett. **95**, 146802 (2005);

[5] C. L. Kane and E. J. Mele, Phys. Rev. Lett. **95**, 226801 (2005).

[6] L .Fu and C. L. Kane, Phys. Rev. B **76**, 045302 (2007).

[7] D. Hsieh *et al*, Nature **452**, 970 (2008).

[8] T. Okuda *et al.*, Rev. Sci. Instrum. **79**, 123117 (2008).

[9] A. Nishide *et al.*, Phys. Rev. B **81**, 041309 (2010)

[10] A. Nishide *et al.*, New Journal of Physics **12** (2010) 065011

R&D EFFORTS OF ERL MAIN LINAC SUPERCONDUCTING CAVITY

Hiroshi Sakai, Takaaki Furuya, Tohru Takahashi, Kensei Umemori,
*Kenji Shinoe, *Norio Nakamura, **Masaru Sawamura
KEK (High Energy Accelerator Research Organization), Tsukuba, Ibaraki 305-0801,
**ISSP (The Institute for Solid State Physics), the University of Tokyo, Chiba, 277-8581*
***JAEA (Japan Atomic Energy Agency), Tokai, Ibaraki,319-1195*

Abstract

In order to obtain the technology needed for ERL main linac, a great deal of effort had been put into development of critical components, such as cavity, input coupler and HOM absorber. Design of a cryomodule, which contains two 9-cell cavities, is also under going.

9-CELL SUPERCONDUCTING CAVITY

We had designed the KEK-ERL model-2 cavity, which is optimized for ERL operation, especially for HOM damping. It has large iris diameter of 80 mm and large beampipes with diameters of 100 mm / 120 mm [1]. Accelerating gradient of 15~20 MV/m is required for ERL cavity. To verify this cavity design, a proto-type of 9-cell cavity (#1 cavity) was manufactured. A series of surface treatment procedure was applied on it. Several vertical tests were carried out to investigate cavity performance at KEK. Figure 1 shows the Q-E curves obtained from 1st to 9th vertical testing [2][3]. All the cases, field emissions were limited the cavity performances up to 15~17 MV/m except for 9th test. Even the initial state of the 7th test was fine and could reach to 25 MV/m without hard field emissions. Unfortunate X-ray bursts happened during pass-band measurements, however, and the final state of cavity was limited to 10 MV/m. By refreshing the inner surface by Electro-polishing, we could reach the 25MV/m at 9th test. We noted that no field emission was found until 15MV/m, which satisfied our ERL requirement.

Now we fabricated and planed to test the #2 KEK-ERL model-2 cavity, whose shape matched for the assembly to ERL cryomodule.

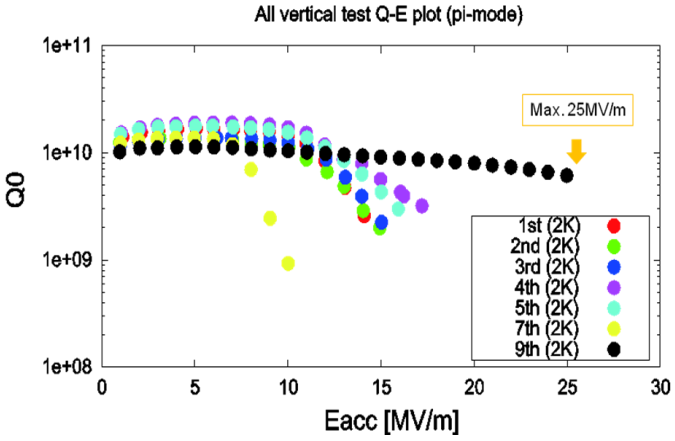

Figure 1: Measured Q-E curves of #1 KEK-ERL model-2 cavity.

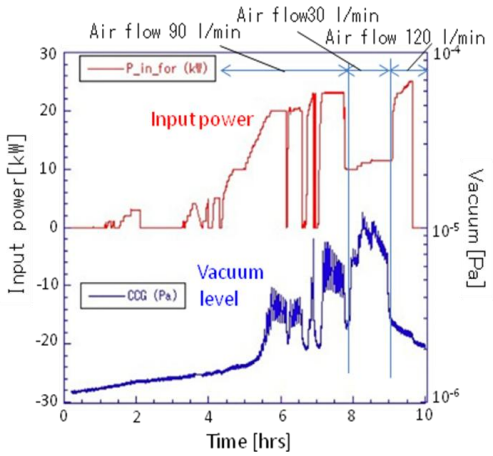

Figure 2: Measurement results of high power test of 2nd model of ceramic window.

INPUT COUPLER

A coaxial type power coupler with double ceramics is designed for ERL main linac input coupler [4]. Maximum RF power of 20 kW with standing wave is required. To reduce dynamic losses HA997 ceramic is used. In order to confirm performances of components, such as ceramics and bellows, we fabricated the high power test stand using 30kW IOT, at JAEA. Unfortunately, the first model of window could not pass enough RF power. Even less than 10kW, unexpected RF losses and temperature rises happened and finally the ceramic windows were broken. Through the low level measurements and computer

simulations with HFSS and MW-studio, it was found that the dipole resonance existed to be close to 1.3GHz [5]. For the second model of the ceramic window was fabricated with thinner HA997 ceramic, to avoid the dipole resonance from operation frequency of 1.3 GHz. It raised the frequency of dipole mode about 30 MHz. High power test was performed and successfully passed 27kW CW standing wave without any abnormal temperature rises as shown in Figure 2. Bellows of inner conductor is another important component to check. Applying air cooling of air flow of 90 l/min, its temperature rise was suppressed to adequate level.

HOM ABSORBER

Ferrite of new IB004 was selected as a material for HOM absorber, after investigating its damping ability at low temperature of 80K. Schematic view and the picture of the prototype HOM absorber are shown in Figure 3. A ferrite cylinder with a thickness of 2 mm is bonded on to the inner surface of a Cu beampipe by HIP.Cooling test of HOM absorber is under investigation at ISSP, University of Tokyo, using this prototype [6].

CRYOMODULE DESIGN

Design of first module for cERL is in progress [7]. Figure 4 shows the design of the cryomodule for ERL main linac. It contains two 9-cell cavities. Each cavity is inserted in the Ti-jacket, whose diameter is 300mm. They are aligned on Ti frames and connected each other through the HOM damper. Slide-jack tuner and piezo tuner are used for frequency tuning.

Two cavities will be fabricated at FY2010 and module assembly will be completed at FY2011.

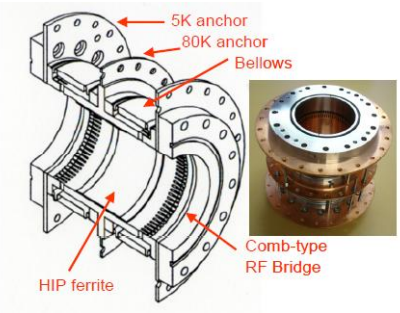

Figure 3 : Schematic view and prototype of the HOM absorber

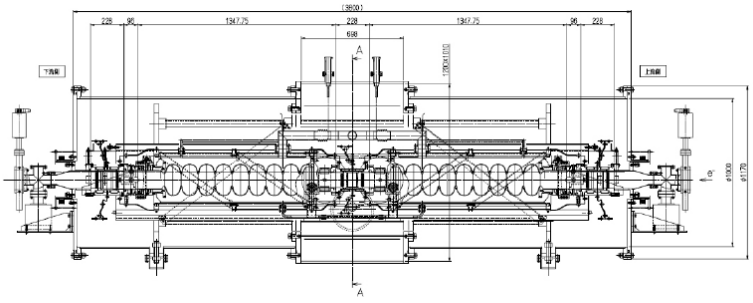

Figure 4 : Design of the prototype cryomodule for the cERL main linac

REFERENCES

[1] K. Umemori *et al.*, "Design of L-band superconducting cavity for the energy recovery linacs", APAC'07, Indore, India, Feb 2007, p.570(2007)
[2] K. Umemori et al., "Results of vertical tests for KEK-ERL 9-cell superconducting cavity", IPAC'10, Kyoto, Japan, May 2010, p2956
[3] H. Sakai et al., "Cavity diagnostics using rotating mapping system for 1.3 GHz ERL-9cell superconducting cavity", IPAC'10, Kyoto, Japan, May 2010, p2950
[4] H. Sakai et al., "Power coupler development for ERL main linac in Japan", IPAC'10, Kyoto, Japan, May 2010, p2953
[5] K. Umemori et al., "Observation of resonance mode in coaxial-type input coupler", IPAC'10, Kyoto, Japan, May 2010, p2959
[6] M. Sawamura et al., "Cooling test of ERL HOM absorber", IPAC'10, Kyoto, Japan, May 2010, p2344
[7] T. Furuya et al., "Development of a prototype module for the ERL superconducting main linac at KEK", IPAC'10, Kyoto, Japan, May 2010, p2923

DEVELOPMENT OF AN YB-DOPED FIBER LASER SYSTEM FOR AN ERL PHOTOCATHODE GUN

I. Ito[1], N. Nakamura[1], D. Yoshitomi[2], K. Torizuka[2], Y. Honda[3]
[1]*Synchrotron Radiation Laboratory, The Institute for Solid State Physics, The University of Tokyo*
[2]*National Institute of Advance Industrial Science and Technology*
[3]*High Energy Accelerator Research Organization*

We are developing an Yb fiber laser system that drives an ERL photocathode gun[1,2]. An Yb fiber laser is expected to have both high stability and high output power required for the drive laser. We have developed 10W preamplifier using an Yb doped photonic crystal fiber and demonstrated second harmonic generation by the conversion efficienc.. We report our recent progress in this development.

Fig.1 shows the schematic of the drive laser system. The drive laser system is MOPA (Master Oscillator and Power Amplifier) type with an Yb fiber laser oscillator and two Yb fiber laser amplifiers. The Yb fiber laser is expected to have high stability and high output power. On the other hand, the Yb fiber laser cannot directly drive the NEA-GaAs photocathode because the wavelength of Yb fiber laser (1030nm) is much longer than that of the band gap of NEA-GaAs (867nm). Therefore, the wavelength conversion from 1030nm to 800nm is done by second harmonic generation and optical parametric amplification.

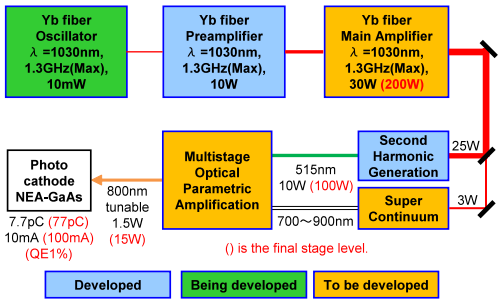

Fig.1. Schematic of drive laser system

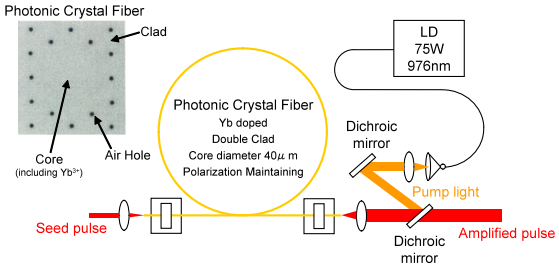

Fig.2. Schematic of Yb fiber laser amplifier

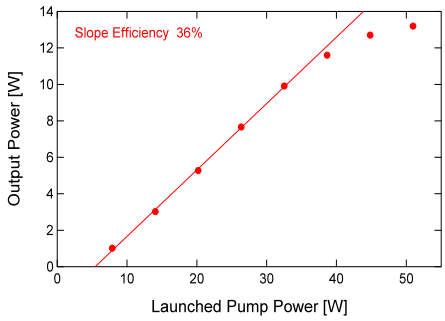

Fig.3. Amplifier slope efficiency

Fig.2 shows the system schematic of the Yb fiber laser amplifier. An Yb doped photonic crystal fiber is used to amplify the seed pulse. The photonic crystal fiber has a large core doped with Yb ions and a clad having periodically allocated air holes. In order to suppress nonlinear optical effect that distorts the amplified pulse, the core diameter need be large to decrease the power density of the amplified pulse. However, if the core diameter is overlarge, multi-mode travelling happens in the core and it distorts the pulse shape. For the case of the photonic crystal fiber, the refractive index of the clad is slightly less than that of the core because of the periodical air holes. So, only single mode can travel in the large core. We evaluated the amplifier slope efficiency, the optical spectrum and the pulse duration using the 85MHz pulse as a seed. Fig.3 shows the amplifier slope efficiency. The slope efficiency is 36%. The 85MHz pulse can be amplified to 150nJ/pluse (=13W/85MHz), which is the same pulse energy as when a 1.3GHz seed pulse is amplified to 200W. Fig.4 shows spectra of a

seed pulse and amplified pulses. A dot line shows the seed pulse and solid lines amplified pulses. FWHMs of amplified spectra are about 10nm, and significant bandwidth broadening does not appear. Fig.5 shows the autocorrelation traces of a seed pulse and amplified pulses. The autocorrelation trace is the convolution of two pulses into which a pulse is divided. FWHMs of the autocorrelation traces are about 1.4ps and almost unchanged. Therefore, we can confirm that nonlinear optical effect that causes the pulse distortion is suppressed in the Yb doped photonic crystal fiber laser amplifier.

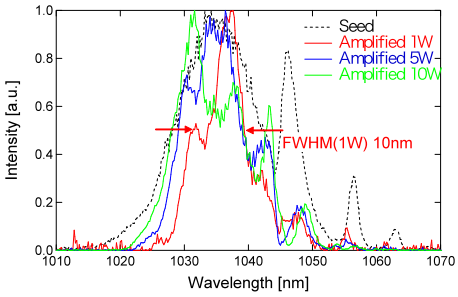

Fig.4. Optical Spectrum

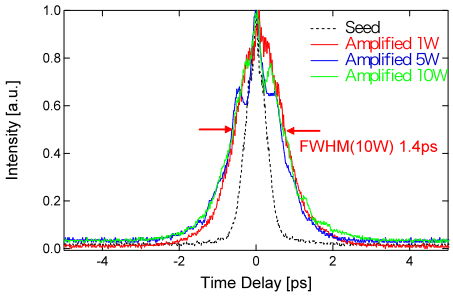

Fig.5. Autocorrelation trace

Since the Yb fiber laser amplifier with the 85MHz seed pulse realized the same pulse energy as required for the ERL photocathode gun, we demonstrated second harmonic generation using the amplifier output. Fig.6 shows a setup of second harmonic generation. The 85MHz seed pulse is amplified to 10W, and the amplified pulse is input into LBO crystal (LiB_3O_5). We use a type-I 5-mm-long LBO crystal. The pulse passing through the LBO crystal involves the fundamental (1035nm) and the second harmonic (518nm). So we lead only the second harmonic to the power meter with two mirrors that reflect only 518nm light.Fig.7 shows the second harmonic power and the conversion efficiency as the function of the fundamental power. When the 9.8W fundamental power is input into the LBO crystal, the second harmonic power of 4.8W is achieved. So the conversion efficiency is 49%. Fig.8 shows the optical spectrum of the 4W second harmonic, and its band width (FWHM) is 1nm.

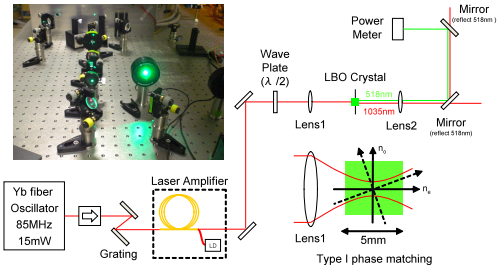

Fig.6. Setup of second harmonic generation

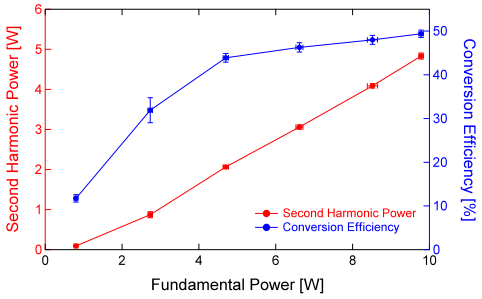

Fig.7. Conversion efficiency

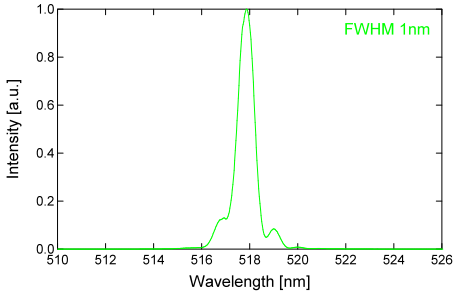

Fig.8. Optical spectrum of second harmonic

References

[1] R. Hajima et al. (ed.), KEK Report 2007-7/JAEA-Research 2008-032 (2008) (in Japanese).
[2] I.Ito et al., Proceedings of IPAC10, Kyoto, 2010.

Tolerance Study on RF Amplitude and Phase of Main Superconducting Cavities and Injection Timing for the Compact ERL

Norio Nakamura*, Miho Shimada**, Tsukasa Miyajima**, Yukinori Kobayashi**, Shogo Sakanaka**, Ryoichi Hajima***

*Synchrotron Radiation Laboratory, The Institute for Solid State Physics, The University of Tokyo
**High Energy Accelerator Research Organization(KEK), ***Japan Atomic Energy Agency(JAEA)

In future ERL-based light sources, higher accuracy may be required for RF control and timing, because the beam has much shorter bunch length and smaller momentum (energy) spread compared with that of the existing storage-ring-based SR sources. We have studied effects of RF amplitude and phase variations of main superconducting(SC) cavities and injection timing jitter with a simulation code "elegant"[1] to know requirements for the RF control and the injection timing of the compact ERL[2] in three operation modes: HC(High Current), LE(Low Emittance) and BC(Bunch Compression) modes. Figure 1 and Table 1 show layout of the compact ERL and the parameters for the three modes.

Table 2 summarizes simulated parameter variations due to the RF amplitude and phase errors(±0.1% and ±0.1°) and the injection timing error(±200 fs) at the exit of the 1st TBA arc in HC mode. The parameter variations are not serious and thus these RF and timing errors are tolerable for the compact ERL. However, since the momentum variation for the RF amplitude error of ±0.1 % is 1.0×10^{-3} and much larger than the momentum spread (1.7×10^{-4} without the RF amplitude error), the RF amplitude error should be improved to the level of 0.01 % in future for making the most of the small momentum spread. Almost the same tolerances are required for the RF control and injection timing in LE mode, because parameter variations due to the errors are almost the same as in HC mode.

Table 1: Parameters of the compact ERL for three operation modes (HC: High Current mode, LE: Low Emittance mode, BC: Bunch Compression mode)

Parameter	HC	LE	BC
RF frequency[GHz]	1.3		
Injection energy[MeV]	5		
Number of main SC cavities	8		
Effective cavity length[m]	1		
Accelerating field[MV/m]	15		
Repetition rate [GHz]	1.3	1.3	≤ 0.001
Average beam current[mA]	100	10	-
Bunch charge[pC]	77	7.7	≥ 77
Emittance[1)][mm·mrad]	1	0.1	-
Bunch length[ps]	2	2	< 0.1

[1)] Normalized emittance

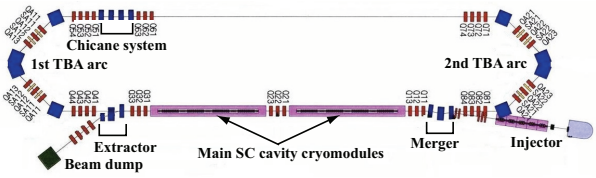

Figure 1: Layout of the compact ERL.

Table 2: Parameter variations at the 1st arc exit in HC mode due to RF amplitude and phase errors and injection timing errors.

Error	$\Delta V/V$ -0.1/0.1 %	$\Delta\phi_{RF}$ -0.1/0.1 °	Δt_{inj} -200/200 fs
Arrival time	-25/1.3 fs	-0.11/0.16 fs	-200/200 fs
Bunch length	< 1 %	< 1 %	< 1 %
Momentum	-0.1/0.1 %	< 0.0002 %	< 0.0002 %
Momentum spread	< 1 %	-4.7/7.1 %	-4.4/6.6 %
Hor. emittance	< 1 %	< 1 %	< 1 %
Vert. emittance	< 1 %	< 1 %	< 1 %

Figure 2 shows the change of 2D electron distribution of the bunch on arrival time-momentum plane at the exit of the 1st TBA arc section for the RF amplitude error of -0.5 % to 0.5 % in 0.1 % step in BC mode. The bunch arrival time is clearly increased with the RF amplitude and the bunch length is increased with the RF amplitude error. Figure 3 shows the arrival time and bunch length variations due to the RF amplitude error. The arrival time variation is almost linear and 410 fs for the RF amplitude error of 0.1 % and it is consistent with the time variation calculated from $\Delta T \approx (R_{56}/c)\cdot(\Delta p/p) \approx (R_{56}/c)\cdot(\Delta V/V)$ and

R_{56}=0.131 m. The bunch length is about 55 fs without the error and its variation is parabolic around the reference RF amplitude. In order to keep the effective bunch length including the arrival time variation within 60 fs and 100 fs, the RF amplitude error should be less than 0.005 % and 0.02 % in rms, respectively. Like the RF amplitude error, the RF phase error causes variations of the arrival time and the bunch length as shown in Fig. 4. The arrival time variation is almost linear and 200 fs for the RF phase error of 0.1°. This is consistent with the time variation calculated from $\Delta T \approx (R_{56}/c)\cdot(\Delta p/p) \approx (R_{56}/c)\cdot\Delta\phi_{RF}\cdot tan\phi_{RF}$ and ϕ_{RF}=15°. The RF phase error should be suppressed to 0.01° and 0.04° to keep the effective bunch length within 60 fs and 100 fs. In BC mode, required stability of the RF amplitude and phase of the main SC cavities should be the level of 0.01% and 0.01°. The arrival time and bunch length variations due to the injection timing error are shown in Fig. 5. The arrival time variation is only less than 10 fs for the injection error of 200 fs, because the injection timing error Δt_{inj} is cancelled by the arrival time variation due to the RF phase error $\Delta\phi_{RF}=2\pi f\Delta t_{inj}$, where f is the accelerating frequency. The injection timing error of 200 fs is enough for preserving the beam quality. More details of the tolerance study are described in ref. 3.

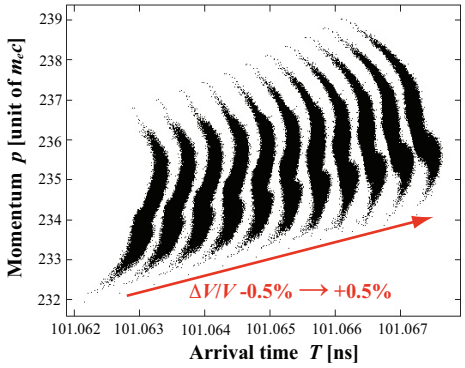

Figure 2: Change of 2D electron distribution of the bunch on the arrival time-momentum plane for the RF amplitude error of -0.5 % to 0.5 % in 0.1 % step.

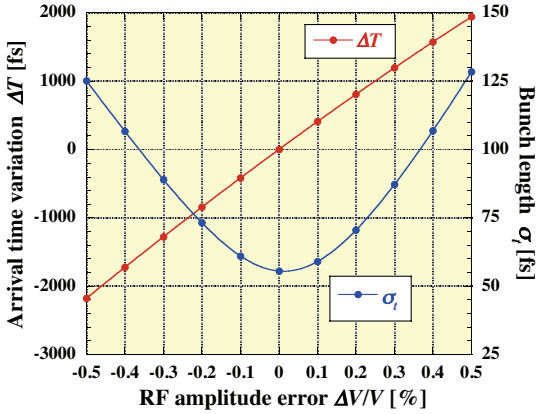

Figure 3: Variations of the arrival time and the bunch length due to the RF amplitude error.

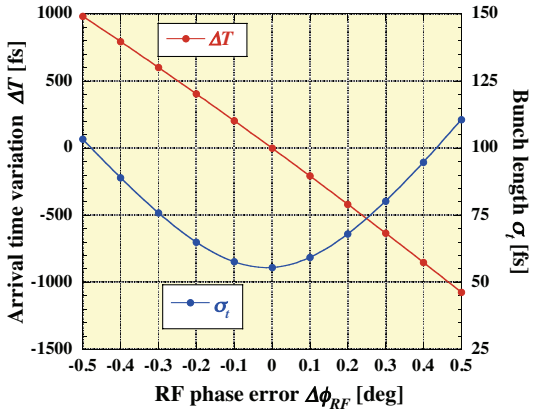

Figure 4: Variations of the arrival time and the bunch length due to the RF phase error.

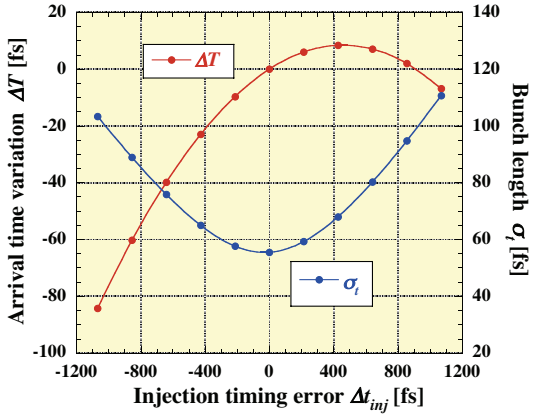

Figure 5: Variations of the arrival time and the bunch length due to the injection timing error.

References

[1] M. Borland, Phys. Rev. ST-AB **4**, 070701 (2001).

[2] R. Hajima, N. Nakamura, S. Sakanaka, Y. Kobayashi(eds.), KEK Report2007-7; T. Shiraga et al., PAC09, Vancouver, 2009.

[3] N. Nakamura et al., Proc. IPAC'10, Kyoto, 2010, pp.2317-2319.

Effects of Alignment Error of Main Superconducting Cavities on ERLs and their Compensation

Norio Nakamura[*], Kentaro Harada[**], Miho Shimada[**], Yukinori Kobayashi[**], Shogo Sakanaka[**], Ryoichi Hajima[***]

[*]*Synchrotron Radiation Laboratory, The Institute for Solid State Physics, The University of Tokyo*
[**]*High Energy Accelerator Research Organization(KEK),* [***]*Japan Atomic Energy Agency(JAEA)*

In ERLs, many superconducting(SC) cavities accelerate and decelerate low-emittance and short-bunch beams. If alignment error of the cavities is considerable, the cavities can harmfully affect the beams because they have strong effects on motion of electrons that are much deviated from the cavity central axis. Since the cavities are contained in cryomodules, achieving high alignment accuracy of the cavities is not easy. Therefore we have studied effects of misalignment of main SC cavities on the compact ERL[1]. Figure 1 shows layout of the compact ERL, which has two arc sections and eight main SC cavities in cryomodules.

For an ultra-relativistic electron($\beta=v/c\approx1$), the averaged equation of transverse motion in the body of a SC cavity is expressed as[2]

$$x'' + \left(\frac{\gamma'}{\gamma}\right)x' + \frac{1}{8}\left(\frac{\gamma'}{\gamma}\right)^2 x = 0 \quad \left(\gamma' \equiv \frac{eE_{rf}}{mc^2}\right) \tag{1}$$

Here x, x', e, m, v, c, γ and E_{rf} are the transverse position and angle (derivative of x respect to the longitudinal position s), electron charge and mass, velocities of the electron and light, Lorentz factor of the electron, and the average RF field of the SC cavity. Furthermore the electron is kicked at the entrance and exit of the SC cavity as[2]

$$\Delta x'_{i(f)} = \mp\frac{1}{2}\frac{\gamma'}{\gamma_{i(f)}}x_{i(f)} \tag{2}$$

where γ_i and γ_f are the Lorentz factors at the entrance and exit of the SC cavity. If misalignment of the SC cavities exists, the beam moving on the central orbit is deflected in the acceleration by the misaligned SC cavities and as a result orbit distortion is generated. For example, the kick angle in Eq. (2) due to the alignment error of 1 mm reaches about 1.5 mrad for the beam energy of 5 MeV and the accelerating field of 15 MV/m.

Chromatic effects of focusing/defocusing elements such as SC cavities and quadrupole magnets can cause emittance growth. When the initial position and angle are uncorrelated with the momentum, the normalized emittance ε_n just after a thin element with focusing strength k is obtained as follows[3]:

$$\varepsilon_n = \sqrt{{\varepsilon_{n0}}^2 + a^2\gamma^2\beta^2k^2\sigma_{x0}^2\sigma_\delta^2\left\langle x_0^2\right\rangle} \tag{3}$$

Here ε_{n0}, σ_{x0}, and σ_δ are the initial normalized emittance, beam size and momentum spread. The focusing strength is assumed to have momentum dependence as $k \propto p^{-a}$. Here $\langle x_0^2\rangle$ means the average of the square of the initial transverse electron position x_0 over the beam and approximately equal to $\langle x_0\rangle^2$ for $|\langle x_0\rangle| >> \sigma_{x0}$. The emittance growth behaves as Eq. (3) with a=1 for edges of SC cavities and quadrupole magnets. For example, the emittance increase is estimated from Eq. (3) to be more than 50 % of the initial emittance ε_{n0}=0.1 mm mrad for $\langle x_0\rangle$=5 mm, k=5 m^{-1} and the typical beam parameter values after acceleration in LE(Low Emittance) mode[1] of the compact ERL, $\gamma\beta$=244.6, σ_{x0}=0.1 mm and σ_δ=2x10^{-4}.

In order to evaluate the effects of the alignment error of the main SC cavities accurately, simulations for the compact ERL were performed by using elegant[4]. Black and red lines in Fig. 2 shows orbits distorted by horizontal/vertical cavity alignment error of +1 mm and orbits corrected by the eigenvector method with constraints[5] in LE and BC(Bunch Compression)

modes[1]. The maximum orbit distortion reaches about 35 mm and 15 mm for LE and BC modes, respectively. Such orbit distortion can cause serious beam loss for a comparable physical aperture size. However the corrected orbits are almost within ±1 mm except for the local orbit in the SC cavities having no BPMs. Simulated normalized emittances (including the momentum dispersion effect) significantly increases by the cavity misalignment as shown in Fig. 4., because the chromatic effects of the quadrupole magnets and SC cavities and the nonlinear fields of the sextupole magnets become considerable by the large orbit distortion. Figure 5 shows simulated 2D electron distributions of the bunch at the exit of the 1st TBA arc section for horizontal/vertical cavity alignment error of $\Delta X/\Delta Y$=±1 mm in BC mode. By the cavity alignment errors, the bunch length increases from 55 fs to more than 100 fs, though the bunch lengthening can be easily compensated by orbit correction.

Simulation results show that misalignment of the main SC cavities in the compact ERL can cause large orbit distortion, non-negligible emittance growth and significant bunch lengthening. However the alignment error can be tolerable at least up to ±1 mm for the compact ERL, because the error effects can be compensated by the orbit correction.

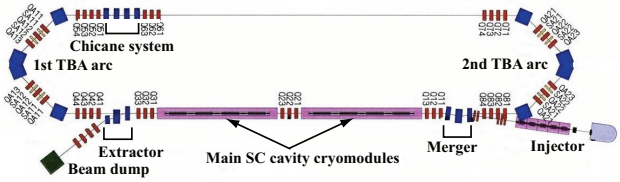

Figure 1: Layout of a 1-loop compact ERL.

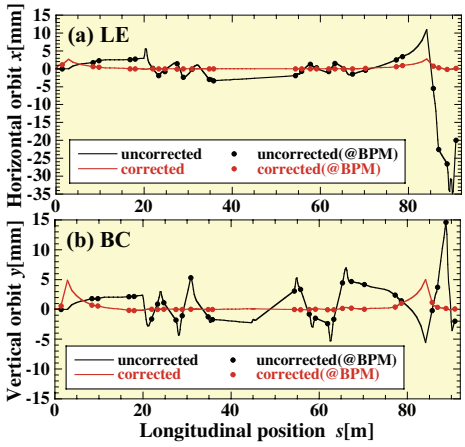

Figure 2: Results of orbit correction: (a) uncorrected and corrected horizontal orbits for the horizontal alignment error of ΔX=+1 mm in LE mode and (b) uncorrected and corrected vertical orbits for the vertical alignment error of ΔY=+1 mm in BC mode. Solid circles indicate 28 positions monitored at the 23 BPMs.

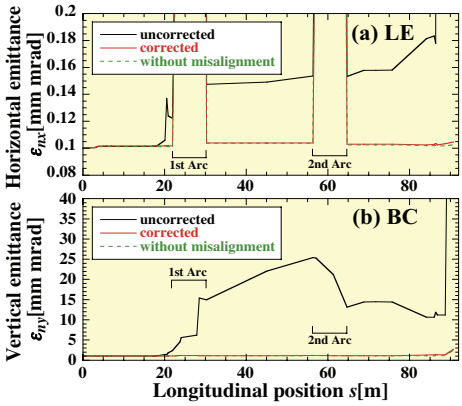

Figure 3: Normalized emittance before and after orbit correction for cavity alignment error of +1 mm and without the cavity alignment error: (a) horizontal emittance for the horizontal error of ΔX=+1 mm in LE mode and (b) vertical emittance for the vertical error of ΔY=+1 mm in BC mode.

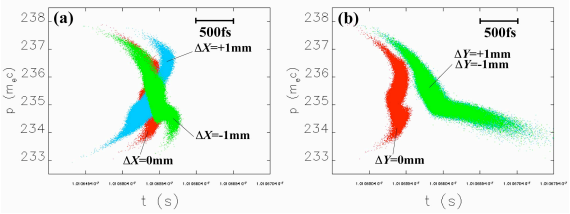

Figure 4: Bunch lengthening due to (a) horizontal and (b) vertical cavity alignment errors of ±1 mm in BC mode.

References

[1] T. Shiraga et al., PAC09, Vancouver, 2009.
[2] J. Rosenzweig and L. Serafini, Phys. Rev. E **49**, 1599 (1994).
[3] N. Nakamura et al., Proc. IPAC'10, Kyoto, 2010, pp.2314-2316.
[4] M. Borland, Phys. Rev. ST-AB **4**, 070701 (2001).
[5] N. Nakamura et al., Nucl. Instr. Meth. A **556** (2006) 421- 432.

Application of the Eigenvector Method with Constraints to Orbit Correction for ERLs

Norio Nakamura* and Kentaro Harada**
*Synchrotron Radiation Laboratory, The Institute for Solid State Physics, The University of Tokyo
**High Energy Accelerator Research Organization(KEK)

Orbit correction in an energy recovery linac(ERL) is more complicated than those of an ordinary linac and a transport line, because the ERL beam passes a long section containing main superconducting cavities at least two times with different energies. The eigenvector method with constraints (hereafter called the EVC method)[1] is a sophisticated and flexible method and suitable for orbit correction for ERLs. We already succeeded in applying the EVC method to orbit correction in the two storage rings, the PF ring and PF-AR[2].

When the vector of a distorted orbit $\vec{x}$ at M beam position monitors(BPMs) is corrected by N corrector kick angles $\vec{\theta}$, the EVC method provides the following solution of $\vec{\theta}$,

$$\vec{\theta} = B\vec{x} - D\vec{z} \tag{1}$$

where

$$B = (-A^{-1} + A^{-1}C^T P^{-1} C A^{-1})R^T, \quad D = A^{-1}C^T P^{-1} \tag{2}$$

$$P = CA^{-1}C^T, \quad A = R^T R \tag{3}$$

Here R is the $M \times N$ response matrix between $\vec{x}$ and $\vec{\theta}$ and the superscript T stands for the transposed matrix or vector. The constraint condition is assumed to be

$$C\vec{\theta} + \vec{z} = 0 \quad , \tag{4}$$

where $\vec{z}$ is a vector of N_c parameters related to the kick angles and C is the response matrix between $\vec{\theta}$ and $\vec{z}$. The matrix A^{-1} is a generalized inverse matrix defined by

$$A^{-1} = \sum_{i=1}^{N_v} \frac{\vec{v}_i \vec{v}_i^T}{\lambda_i} \quad (N_c \le N_v \le N). \tag{5}$$

Here λ_i (≥ 0) and $\vec{v}_i$ are the i-th largest eigenvalue and its eigenvector of the matrix A.

When the betatron functions and phases at the i-th position monitored by its corresponding BPM and the j-th corrector are (β_i, ϕ_i) and (β_j, ϕ_j) respectively, the response matrix element R_{ij} between the i-th position and the kick angle of the j-th corrector is expressed by

$$R_{ij} = \sqrt{\frac{p_j}{p_i}} \sqrt{\beta_i \beta_j}\, sin(\phi_i - \phi_j), \quad \phi_i > \phi_j \tag{6}$$

where p_i and p_j are the beam momenta at the i-th position and the j-th corrector, respectively. In the 2nd turn, the j-th corrector that the beam passes two times provides the (j+L)-th kick as well as the j-th kick. Here L is the total number of the correctors in the ERL loop. In this case, the response matrix element R_{ij} is given by

$$R_{ij} = \sqrt{\frac{p_j}{p_i}} \sqrt{\beta_i \beta_j}\, sin(\phi_i - \phi_j) + \sqrt{\frac{p_{j+L}}{p_i}} \sqrt{\beta_i \beta_{j+L}}\, sin(\phi_i - \phi_{j+L}), \quad \phi_i \ge \phi_{j+L} > \phi_j \tag{7}$$

Here p_{j+L}, β_{j+L} and ϕ_{j+L} are the beam momentum and the betatron function and phase at the j-th corrector in the second turn.

The EVC method was applied to orbit correction for the compact ERL. Layout of the compact ERL[3] including 23 BPMs(BPM01-BPM23) and 19 correctors(COR01 -COR19) is shown in Fig. 1. The orbit distortion to be corrected was generated by position error of +1 mm for the eight main SC cavities. The beam orbits were simulated by elegant[4] including non-linear effects such as coherent synchrotron radiation(CSR) and the kick angles of the

correctors were calculated by the EVC program. We chose constraint conditions that the two positions at BPM13 and BPM14 are zero, because the beam in the long straight section between the two BPMs should be particularly corrected and stabilized for user experiments.

Figure 2 shows a distorted orbit by the horizontal cavity position error of +1 mm and a corrected one by the EVC method with the eigenvector number N_v=7 in Low Emittance(LE) mode. The beam orbit could be almost corrected within ±1 mm except for in the SC cavities having no BPMs. As shown in Fig.3, the normalized emittance was substantially increased at the quadrupole magnets before the 1st arc section for the distorted orbit, because the chromatic effects were caused by the large orbit distortion. However the emittance increase was negligibly small in all the regions of the compact ERL for the corrected orbit.

The RMS beam position of the EVC method was equal within 5 % to that of the ordinary eigenvector method without constraints for $N_v \geq 3$. On the other hand, the beam positions at the two selected BPMs, BPM13 and BPM14, were much better corrected by using the constraint conditions as shown in Fig. 4. This is a great advantage of the EVC method. Exact orbit correction at locations where the orbit accuracy or stability is especially required can be achieved by the EVC method even if a large number of eigenvectors that may cause local orbit distortion and undesirable emittance growth in the regions without any BPM are not used[5].

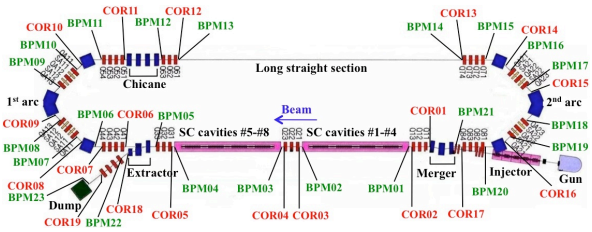

Figure 1: Layout of the compact ERL. Twenty-three beam position monitors(BPMs) and nineteen correctors are distributed.

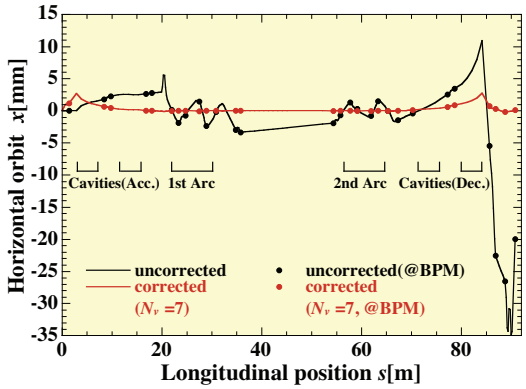

Figure 2: Horizontal orbits uncorrected and corrected by the EVC method with the eigenvector number N_v=7. The solid circles indicate the positions at the BPMs.

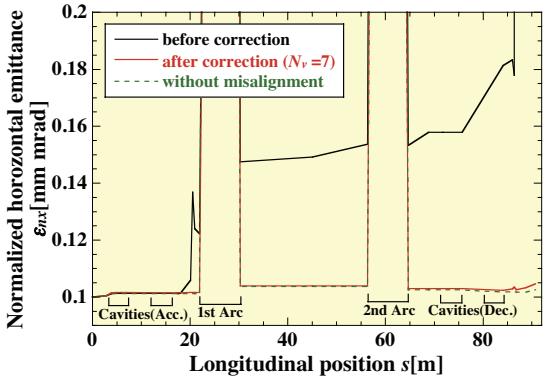

Figure 3: Horizontal normalized emittances in LE mode for orbits uncorrected and corrected by the EVC method with the eigenvector number N_v=7.

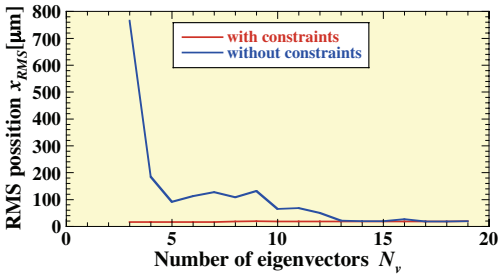

Figure 4: RMS beam positions for the two BPMs (BPM13 and BPM14) after orbit correction by the eigenvector method with and without constraints.

References

[1] N. Nakamura et al., Nucl. Instr. Meth. A **556** (2006) 421- 432.
[2] K. Harada et al., Nucl. Instr. Meth. A **604** (2009) 481-488.
[3] T. Shiraga et al., PAC09, Vancouver, 2009.
[4] M. Borland, Phys. Rev. ST-AB **4**, 070701 (2001).
[5] N. Nakamura et al., Proceedings of IPAC10, Kyoto, 2009, pp.2320-2322.

NEW PULSED POWER SUPPLY FOR THE PULSED SEXTUPOLE INJECTION SYSTEM AT THE PF RING

Hiroyuki Takaki[1], Kentaro Harada[2], Tohru Honda[2], Yukinori Kobayashi[2],

Tsukasa Miyajima[2], Shinya Nagahashi[2], Norio Nakamura[1], Takashi Obina[2], Miho Shimada[2],

Ryota Takai[2], Akira Ueda[2],

[1]*Synchrotron Radiation Laboratory, The Institute for Solid State Physics, The University of Tokyo*

[2]*KEK-PF*

Suppressing stored beam oscillation during beam injection has become important with the top-up injection for synchrotron radiation (SR) sources. We proposed a beam injection system with a pulsed sextupole magnet (PSM) [1] and installed it at the PF-ring in the spring of 2008. The beam injection with the PSM system was successfully operated. However, because the pulsed power supply (PS) of the PSM injection system had been optimized and used for the pulsed quadrupole injection system at the Photon Factory Advanced Ring, the pulse width of the PS was about four times as long as the revolution time of the PF ring (0.624 μs). If the injected beam is kicked at the peak of the half-sine shaped pulse of the PSM in the first turn, a pulse width must be less than about 1.2 μs to prevent the second kick from the PSM after revolving the PF ring. Since the old PS had a pulse width of 2.4 μs, the PSM kicks the injected beam by 0.7 times the strength of the first kick in the second turn. By this kick, the capture efficiency of the injected beam decreases by about 30% in the normal operating tune of the PF ring.

A new PS optimized for the PSM injection at the PF ring was fabricated. The pulse has a half-sine shape with the pulse width of 1.2 μs. The peak current is 3000 A and the maximum voltage is 30 kV limited by the insulation of the PSM. The maximum repetition rate is 25 pps. The new power supply consists of a DC part and a pulsar part. The DC part was placed at the underground pit of the ring tunnel and the pulsar part was installed in the ring tunnel to minimize the inductance of the connection cable between PSM and the PS.

Figure 2 shows the Block diagram of the pulser circuit. The DC part charges the main capacitor and the thyratron turns on by the outer trigger. The thyratron (CX1175C: manufactured by E2V) has 2-gap structure and is installed in a coaxial structure housing. The inside of the housing is air-cooled by a fan. In general, recovery time of the multi-gap

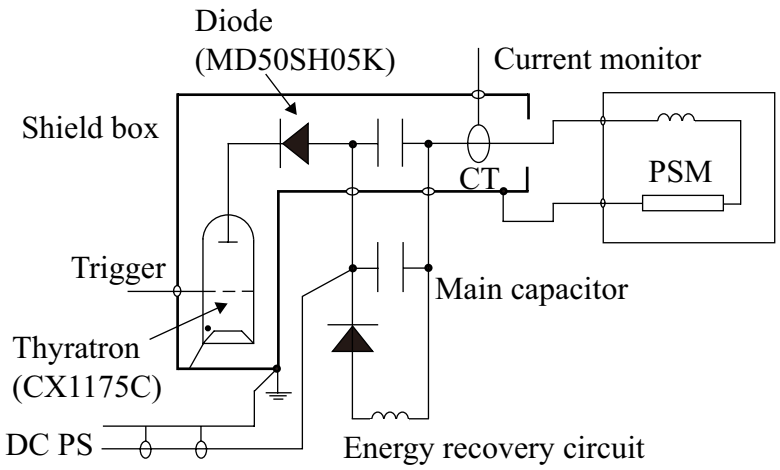

Figure 1: Block diagram of the new pulsed power supply.

thyratron is slow and it has about 50 μs in our case. To prevent the reverse current, which caused undershoot of the excitation current of the PSM, a diode (MD50SH05K manufactured by Origin Electronic) was adopted in the circuit. Although the diode reduced the reverse recovery time from 50 μs to about 0.5 μs, the undershoot remained during 0.5 μs. However, since the injection beam from the KEK-LINAC to PF is always a single bunch, we can avoid the undershoot effect by setting the injection timing to zero-cross point (see figure 2).

The total charge of the main capacitor is very large in the new PS. If we use the charge absorption circuit for the main circuit, the power loss is 21 J/shot. Since the maximum repetition frequency of the injection is 25 pps, the power loss becomes 525 W. If this power is absorbed using resistors in the charge absorption circuit, we have to consider the cost, size, and cooling of the system. Therefore, we decided to revive the power by an energy recovery circuit using a resonant circuit. Figure 2 shows the resulting pulse shape of the PSM excitation. The CT (model-411 manufactured by Pearson Electronics) was used to measure the pulse current and a 20 dB attenuator was attached. The inductance of the PSM was 2.4 μH; the resistance was 0.055 Ω at 100 kHz. Since the inductance of the new power supply was estimated to be 1.29 μH, 28.5 kV was achieved at the peak current of 3000 A, where the limit of the maximum voltage was 30 kV. The stability of the output peak current was less than 0.5 % during 24 hours.

The control system of the old PS was isolated from the ring control system (EPICS) so far. Since the new PS has PLC controller with Linux CPU and LAN module, it can be controlled by the PF standard control system.

References

[1] H. Takaki, N. Nakamura, Y. Kobayashi, K. Harada, T. Miyajima, A. Ueda, S. Nagahashi, M. Shimada, T. Obina, T. Honda, Phys. Rev. ST Accel. Beams **13**, 020705 (2010), URL: http://prst-ab.aps.org/pdf/PRSTAB/v13/i2/e020705.

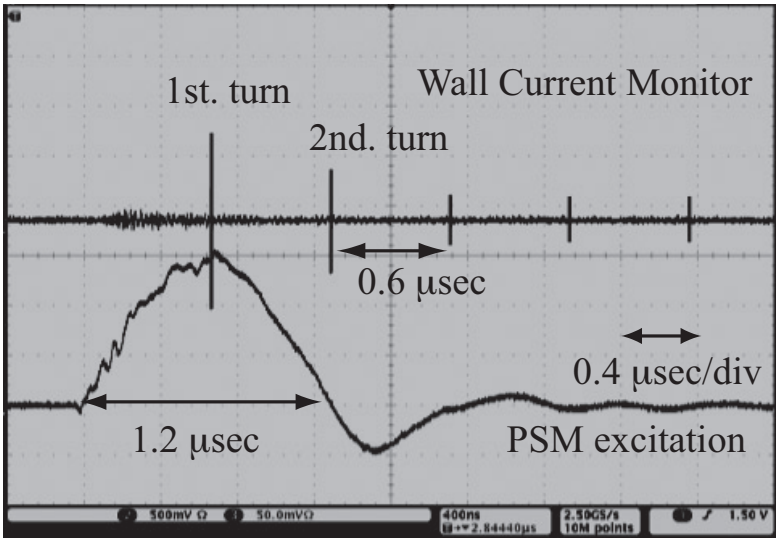

Figure 2: The waveform of the new PS and the signal of the injected beam.

Performance Tests of a Phase Shifter Prototype for a Polarization-Controlled Undulator

Norio Nakamura[*], Isao Ito[*], Kenji Shinoe[*], Takashi Shibuya[*], Hirofumi Kudo[*], Hiroyuki Takaki[*], Kosei Onoue[*], Takashi Tanaka[**], Hideo Kitamura[**], Teruhiko Bizen[***]

[*]*Synchrotron Radiation Laboratory, The Institute for Solid State Physics, The University of Tokyo*

[**]*SPring-8 Center, RIKEN*, [***]*Japan Synchrotron Radiation Research Institute(JASRI)*

An electromagnetic phase shifter prototype for fast helicity switching of a 27-m polarization-controlled undulator has been developed and tested at ISSP[1][2][3][4]. The phase shifter prototype consists of three H-type magnets (Magnet A, B and C) with the yoke-length ratio of 1:2:1 as shown in Fig. 1 and the yokes are made of 0.1-mm-thick permalloy laminations united and insulated by varnish.

Figure 2 shows field reproducibility on the center of Magnet B measured by a Hall probe system. The coil current was increased up from 0 to 1500 AT and decreased down from 1500 to 0 AT and the up and down cycle was repeated three times. It was confirmed that the field reproducibility is very high due to the ultra-low hysteresis of the permalloy yoke. On the other hand, the field reproducibility of a yoke made of the 0.1-mm-thick silicon-steel laminations is much worse than that of the laminated permalloy yoke as shown in Fig. 3, though it is not so low if only the down path is used. Figure 4 shows the measured field reproducibility for a yoke of the 0.2-mm-thick permalloy laminations for comparison.

Figure 1: Phase shifter prototype.

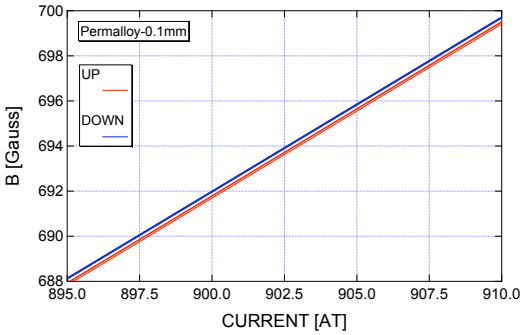

Figure 2: Magnetic field on the center of Magnet B as function of coil current for the yoke of 0.1-mm-thick permalloy laminations.

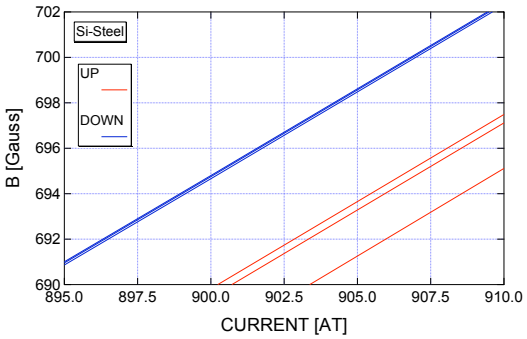

Figure 3: Magnetic field on the center of Magnet B as function of coil current for a yoke of 0.1-mm-thick silicon-steel laminations.

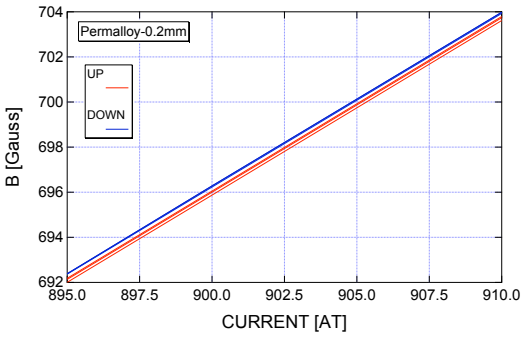

Figure 4: Magnetic field on the center of Magnet B as function of the coil current for a yoke of 0.2-mm-thick permalloy laminations.

Figure 5 shows measured and calculated frequency responses of the stainless-steel(SS) vacuum duct which has a thickness of about 5 mm and a cross-section approximated by a rectangular with width 90 mm and height 18 mm. The phase is significantly delayed at 100

Hz. The thickness of the vacuum duct should be, if possible, reduced for suppressing effects of eddy currents of the duct because a 1.5-mm-thick SS pipe with a diameter of 27 mm has sufficient performance in frequency response as shown in Fig. 6. However we will replace the SS vacuum duct by a ceramic duct to improve the frequency response with almost keeping the mechanical strength and cross-sectional shape.

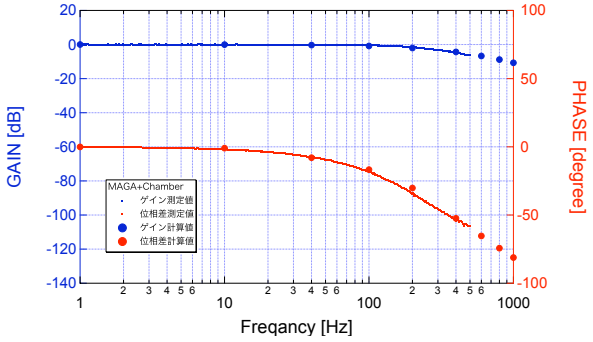

Figure 5: Measured and calculated frequency responses of the 5-mm-thick stainless-steel vacuum duct.

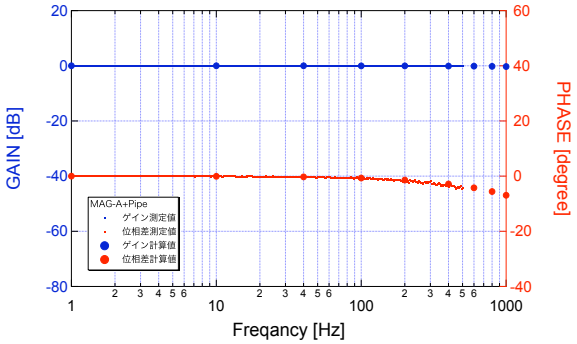

Figure 6: Measured and calculated frequency responses of a 1.5-mm-thick stainless-steel pipe.

Residual field integral of a phase shifter along the beam axis causes movement of the beam orbit. The field integral of the phase shifter prototype excited by AC coil currents was measured with a long-coil system[4]. Figure 7 shows the measured power spectral density(PSD) of the field integral at the excitation frequency of 100 Hz after fine tuning of the AC coil currents of the three magnets. The residual field integral integrated over frequency in RMS is only 0.83 G·cm for the peak-to-peak AC coil currents I_A=I_C=181 AT and I_B=215 AT.

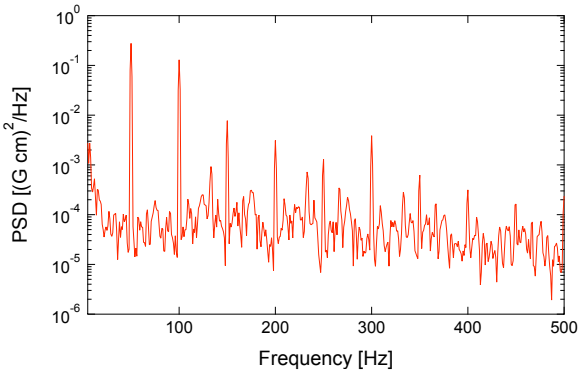

Figure 7: Power spectral density of the field integral of the phase shifter prototype at the excitation frequency of 100 Hz after fine tuning of the AC coil currents of the three magnets for the peak-to-peak AC coil currents I_A=I_C=181 AT and I_B=215 AT.

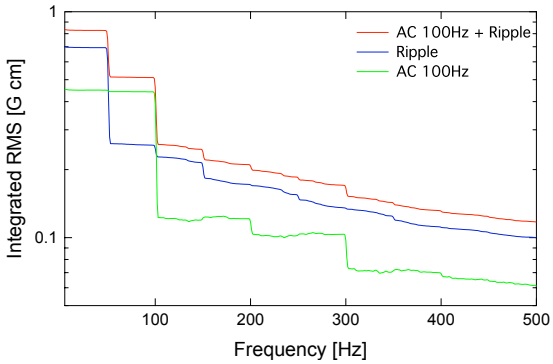

Figure 8: Residual field integral of the phase shifter prototype integrated over frequency in RMS at the excitation frequency of 100 Hz(red line). The blue line shows the contribution of the power supply ripple and the green line square root of difference between squares of red and blue lines.

References

[1] Activity Report of Synchrotron Radiation Laboratory 2007-2008.

[2] N. Nakamura et al., Proceedings of the 5th Annual Meeting of Particle Accelerator Society of Japan and the 33rd Linear Accelerator Meeting in Japan, Higashi-hiroshima, 2008, pp.589-591.

[3] N. Nakamura et al., Proceedings of PAC09, Vancouver, 2009.

[4] I. Ito et al., Proceedings of the 6th Annual Meeting of Particle Accelerator Society of Japan and the 34th Linear Accelerator Meeting in Japan, Tokai, 2009, pp.664-667.

Staff

Director: KAKIZAKI Akito

Solid State Spectroscopy and Instrumentation Group:

KAKIZAKI Akito, Professor
MATSUDA Iwao, Associate Professor
YAMAMOTO Susumu, Research Associate (2009. 10～)
FUJISAWA Masami, Research Associate
HARASAWA Ayumi, Technical Associate
FUKUSHIMA Akiko, Technical Associate

Accelerator Physics Group:

NAKAMURA Norio, Associate Professor
TAKAKI Hiroyuki, Research Associate
SAKAI Hiroshi, Research Associate (～2009. 5)
SHINOE Kenji, Technical Associate
KUDO Hirofumi, Technical Associate
SHIBUYA Takashi, Technical Associate
ITOH Isao, Technical Associate

Technical Assistant:

ONOUE Kousei (2009. 6～)

Secretary:

AIHARA Yumiko
HAMAGUCHI Noriko (～2009. 8)
SOMEYA Akiko (2009. 6～)
YAMAMOTO Yukimi (2009. 8～)

Graduate Student:

ARAI Kuniaki
HASEGAWA Takahide
TAKEICHI Yasuo
OGAWA Manami
NISHIDE Akinori
NAKAMURA Fumitaka

Contract Researcher:

NARITA Hisashi (～2009.12)
RAN Fanyong (2009.10～)

List of Publications

1. Local Electronic States on Two-Dimensional Nanaoscale Island of Si and Ge Fabricated on Si(111) 7 x 7 Substrate

Y. Shigeta, R. Negishi, and M. Suzuki
Int. J. Nanoscience ***8****, 595 (2009).*

2. Anisotropic Two-Dimensional Metallic State of Ge(001)*c*(8x2)-Au Surfaces: An Angle-Resolved Photoelectron Spectroscopy

K. Nakatsuji, R. Niikura, Y. Shibata, M. Yamada, T. Iimori, and F. Komori
Phys. Rev. B ***80****, 081406(R)(2009).*

3. Modification of electronic states of R3XR3-Ag structure by strained Ge/Si(111) substrate

I. Mochizuki, R. Negishi, and Y. Shigeta
J. Appl. Phys. ***106****, 013709 (2009).*

4. Electronic structure of dysprosium silicide films grown on a Si(111) surface

A. Imai, H. Kakuta, K. Mawatari, A. Harasawa, N. Ueno, T. Okuda, and K. Sakamoto
Appl. Surf. Sci. ***in press*** *(2009).*

5. Direct mapping of the spin-filtered surface bands of a three-dimensional quantum spin Hall insulator

A. Nishide, A. A. Taskin, Y. Takeichi, T. Okuda, A. Kakizaki, T. Hirahara, K. Nakatsuji, F. Komori, Y. Ando, and I. Matsuda
Phys. Rev. B ***81****, 041309(R) (2009).*

6. High efficiency and high energy-resolution spin-polarized photoemission spectrometer

T. Okuda, Y. Takeichi, A. Harasawa, I. Matsuda, T. Kinoshita, and A. Kakizaki
Eur. Phys. J. Special Topics ***169****, 181 (2009).*

7. Study of Electronic States for V thin Films Deposited on 6H-SiC Substrates by Soft X-Ray Emission Spectroscopy

K. Nakatsuji, T. Iimori, Y. Takagi, D. Sekiba, S. Doi, M. Yamada, T. Okuda, A. Harasawa, M.Hirai, H.Okazaki, R.Yoshida, M.Tajima, K.Saeki, Y.Muraoka, and T.Yokoya
Appl. Surf. Sci. ***256****, 948 (2009).*

8. Conductivity of the Si(111)7×7 dangling-bond state

M. D'angelo, K. Takase, N. Miyata, T. Hirahara, S. Hasegawa, A. Nishide, M. Ogawa, and I. Matsuda
Phys. Rev. B ***79****, 035318 (2009).*

9. Atomic Scale Study of Surface Structures and Phase Transition with Reflection High-Energy Positron Diffraction

S. Yamazaki, I. Matsuda, H. Okino, H. Morikawa, and S. Hasegawa
Mater. Sci. For. ***607****, 94-98 (2009).*

10. Localization and Hopping Conduction at Glass and Crystal Phases of Monatomic Au Layers on Silicon Surface

K. Kaneda, K. Kitsuka, Y. Nowatari, M. Ikematsu, M. Iseki, T. Higuchi, T. Hattori, and T. Tsukamoto
Phys. Rev. B ***79****, 085317 (2009).*

11. High efficiency and high-energy resolution spin-polarized photoemission spectrometer,
T. Okuda, *et al.*
Eur. Phys. J. Special Topics ***169****, 181-185 (2009).*

12. Substrate dependence of anisotropic electronic structure in Ag(111) quantum film studied by angle-resolved photoelectron spectroscopy,
T. Okuda, Y. Takeichi, K. He, A. Harasawa, A. Kakizaki, and I. Matsuda
Phys. Rev. B ***80****, 113409 (2009).*

13. Metal Co-Adsorption Induced R21xR21 Superstructure on Si(111) Surface Studied by Reflection High-Energy Positron Diffraction
Y. Fukaya, I. Matsuda, M. Hashimoto, H. Narita, A. Kawasuso, and A. Ichimiya
E-J. Surf. Sci. Nanotechnology, ***7****, 432 (2009).*

14. Nanoscale chemical imaging by scanning tunneling microscopy assisted by synchrotron radiation
T. Okuda, T. Eguchi, K. Akiyama, A. Harasawa, T. Kinoshita, Y. Hasegawa, M. Kawamori, Y. Haruyama, and S. Matsui
Phys. Rev. Lett. ***102****,105503 (2009).*

15. 高効率スピン分解光電子分光装置の開発と表面研究への応用
奥田太一
表面科学

16. Beam Optics Study for the Compact ERL in Japan:
T. Shiraga, N. Nakamura, H. Takaki, R. Hajima, K. Harada, M. Shimada, T. Miyajima, Y. Kobayashi, and S. Sakanaka,
Proceedings of the 23rd Particle Accelerator Conference (PAC09) (PAC09, 2009).

17. Effects of Longitudinal and Transverse Resistive-Wall Wakefields on ERLs
N. Nakamura
Proceedings of ERL09 (Cornell University, 2009).

18. Phase Shifter Prototype with Laminated Permalloy Yokes for a Polarization-Controlled Undulator
N. Nakamura, K. Shinoe, I. Ito, T. Shibuya, A. Ishii, H. Kudo, H. Takaki, T. Tanaka, H. Kitamura, and T. Bizen
Proceedings of the 23rd Particle Accelerator Conference (PAC09) (PAC09, 2009).

19. Status of the Energy Recovery Linac Project in Japan

S. Sakanaka, M. Akemoto, T. Aoto, D. Arakawa, A. Enomoto, S. Fukuda, K. Furukawa, T. Furuya, K. Haga, K. Hara, K. Harada, T. Honda, Y. Honda, H. Honma, T. Honma, K. Hosoyama, M. Izawa, E. Kako, T. Kasuga, H. Kawata, M. Kikuchi, Y. Kobayashi, Y. Kojima, T. Matsumoto, H. Matsushita, S. Michizono, T. Mitsuhashi, T. Miura, T. Miyajima, T. Muto, S. Nagahashi, T. Naito, H. Nakai, H. Nakajima, E. Nakamura, K. Nakanishi, T. Nogami, S. Noguchi, T. Obina, S. Ohsawa, T. Ozaki, S. Sasaki, K. Satoh, M. Satoh, T. Shidara, M. Shimada, T. Shioya, T. Shishido, T. Suwada, T. Takahashi, R. Takai, Y. Tanimoto, M. Tawada, M. Tobiyama, K. Tsuchiya, T. Uchiyama, K. Umemori, K. Watanabe, M. Yamamoto, S. Yamamoto, Y. Yamamoto, R. Hajima, H. Iijima, N. Kikuzawa, E. J. Minehara, R. Nagai, N. Nishimori, M. Sawamura, N. Nakamura, A. Ishii, I. Ito, T. Kawasaki, H. Kudoh, H. Sakai, T. Shibuya, K. Shinoe, T. Shiraga, H. Takaki, M. Katoh, M. Kuriki, S. Matsuba, D. Yoshitomi, K. Torizuka, and H. Hanaki,

Proceedings of the 23rd Particle Accelerator Conference (PAC09) (PAC09, 2009).

20. Stored Beam Stability during Pulsed Sextupole Injection at the Photon Factory Storage Ring

H. Takaki, N. Nakamura, Y. Kobayashi, K. Harada, T. Miyajima, A. Ueda, S. Nagahashi, M. Shimada, T. Honda, and T. Obina,

Proceedings of the 23rd Particle Accelerator Conference (PAC09) (PAC09, 2009).

21. Beam Instrumentation for KEK ERL Test Facility

K. Furukawa, K. Haga, S. Hiramatsu, T. Kasuga, T. Mitsuhashi, T. Naito, T. Obina, M. Satoh, M. Tadano, M. Tobiyama, and N. Nakamura

Proceedings of ERL07, edited by John Poole and Neil Thompson (Daresbury Laboratory, 50-52.2009).

22. COMPACT ERL LINAC

K. Umemori, T. Furuya, E. Kako, S. Noguchi, H. Sakai, M. Satoh, T. Shishido, T. Takahashi, K. Watanabe, Y. Yamamoto, K. Shinoe, and M. Sawamura

Proceedings of SRF2009, 896-901(HZB, 2009).

23. Development of 20kW input power coupler for 1.3GHz ERL main linac ---- Component test at 30kW IOT test stand

H. Sakai, K. Umemori, S. Sakanaka, T. Takahashi, T. Furuya, K. Shinoe, A. Ishii, N. Nakamura, and M. Sawamura

Proceedings of Particle Accelerator Society Meeting 2009, 866-868. (PASJ, 2009).

.

24. Development of a 1.3GHz 9-cell Superconducting Cavity for the Energy Recovery Linac

H. Sakai, K. Shinoe, T. Furuya, S. Sakanaka, T. Suwada, T. Takahashi, K. Umemori, and M. Sawamura

Proceedings of ERL07, edited by John Poole and Neil Thompson 56-61.

(Daresbury Laboratory, 2009).

25. Development of a linear cavity Yb-doped fiber laser oscillator for driving an ERL photocathode gun

T. Kawasaki, I. Ito, N. Nakamura, D. Yoshitomi Y. Kobayashi, K. Torizuka, and T. H. Kawta

Proceedings of Particle Accelerator Society Meeting 2009, 124-126 (PASJ, 2009).

26. Development of HOM damper for ERL Main Linac

M. Sawamura, K. Umemori, T. Furuya, H. Sakai, and K. Shinoe

Proceedings of Particle Accelerator Society Meeting 2009, 878-879 (PASJ, 2009).

27. Development of Input Power Coupler for Erl Main Linac in Japan
H. Sakai, T. Furuya, S. Sakanaka, T. Takahashi, K. Umemori, A. Ishii, N. Nakamura, K. Shinoe, and M. Sawamura
Proceedings of SRF2009, 684-688 (HZB, 2009).

28. ERL HOM Absorber Development
M. Sawamura, T. Furuya, H. Sakai, K. Umemori and K. Shinoe
Proceedings of SRF2009, 698-701 (HZB, 2009).

29. Design Study of the Compact ERL Optics
Takashi Shiraga
Master Thesis (in Japanese), University of Tokyo, 2009.

30. Development of Fiber Laser Oscillators for Driving an ERL Electron Gun
Taisuke Kawasaki
Master Thesis (in Japanese), University of Tokyo, 2009.

31. Lattice and Optics Designs of the Test ERL in Japan
K. Harada, T. Kasuga, Y. Kobayashi, T. Miyajima, T. Ozaki, S. Sakanaka, K. Satoh, M. Tobiyama, R. Hajima, N. Nakamura, H. Takaki, and M. Shimada
Proceedings of ERL07, edited by John Poole and Neil Thompson, 26-29(Daresbury Laboratory, 2009).

32. Longitudinal and Transverse Resistive-Wall Wakefields and Their Effects on ERLS
N. Nakamura
Proceedings of Particle Accelerator Society Meeting 2009, 104-106 (PASJ, 2009).

33. Magnetic Field Measurement of Fast Electromagnetic Phase Shifter Prototype for a Polarization-Controlled Undulator
I.Ito, N. Nakamura, K. Shinoe, T. Shibuya, H. Kudo, H. Takaki, T. Tanaka, H. Kitamura, and T. Bizen
Proceedings of Particle Accelerator Society Meeting 2009, 664-666 (PASJ, 2009).

34. Recent Progress of Construction for Compact Energy Recover LINAC
Y. Kobayashi, S. Sakanaka, K. Satoh, T. Kasuga, H. Kawata, R. Hajima, and N. Nakamura
Proceedings of Particle Accelerator Society Meeting 2009, 66-68 (PASJ, 2009).

35. Status of 9-Cell Superconducting Cavity Development for ERL Project in Japan
K. Umemori, T. Furuya, H. Sakai, T. Takahashi, K. Shinoe, and M. Sawamura
Proceedings of SRF2009, 355-358 (HZB, 2009).

36. Study of Resistive-Wall Beam Breakup
N. Nakamura
Proceedings of ERL07, edited by John Poole and Neil Thompson, 45-49 (Daresbury Laboratory, 2009).

37. Tolerance Study on RF Amplitude and Phase of Main Accelerating Cavities and Injection Timing for the Compact ERL
N. Nakamura, T. Miyajima, M. Shimada, Y. Kobayashi, S. Sakanaka, and R. Hajima
Proceedings of Particle Accelerator Society Meeting 2009, 109-111 (PASJ, 2009).

38. Research and development for future ERL light sources and construction of the Compact ERL

R. Hajima, N. Nakamura, S. Sakanaka, Y. Kobayashi
Journal of Particle Accelerator Society of Japan (*in Japanese*), ***6,*** *2, 149-157(2009).*

39. Orbit correction using an eigenvector method with constraints for synchrotron radiation sources

K. Harada, T. Obina, Y. Kobayashi, N. Nakamura, H. Takaki and H. Sakai
Nucl. Instr. and Meth. Phys. Res. A ***604****,481-488 (2009).*

40. Development of a new initial-beam-loading compensation system and its application to a free-electron-laser linac

M. Satoh, T. Koseki, T. Shidara, S. Fukuda, H. Kobayashi, Y. Kamiya, N. Nakamura, T. Sakai, Y. Hayakawa, T. Tanaka, K. Hayakawa, I. Sato and S. Miura
Phys. Rev. ST Accel. Beams ***12,*** *013501-013509 (2009).*